Atmos. Chem. Phys., 25, 9561–9581, 2025
https://doi.org/10.5194/acp-25-9561-2025

Atmospheric Chemistry and Physics
Open Access
EGU

Research article

Surprisingly robust photochemistry in subarctic particles during winter: evidence from photooxidants

Laura M. D. Heinlein[1], Junwei He[1], Michael Oluwatoyin Sunday[1,a], Fangzhou Guo[2,b], James Campbell[3], Allison Moon[4], Sukriti Kapur[5], Ting Fang[5,c], Kasey Edwards[5], Meeta Cesler-Maloney[3,d], Alyssa J. Burns[1], Jack Dibb[6], William Simpson[3], Manabu Shiraiwa[5], Becky Alexander[4], Jingqiu Mao[3], James H. Flynn III[2], Jochen Stutz[7], and Cort Anastasio[1]

[1]Department of Land, Air and Water Resources, University of California, Davis, CA 95616, USA
[2]Department of Earth & Atmospheric Sciences, University of Houston, Houston, TX 77204, USA
[3]Department of Chemistry and Biochemistry, University of Alaska, Fairbanks, AK 99775, USA
[4]Department of Atmospheric Sciences, University of Washington, Seattle, WA 98195, USA
[5]Department of Chemistry, University of California, Irvine, CA 92697, USA
[6]College of Engineering & Physical Sciences, University of New Hampshire, Durham, NH 03824, USA
[7]Department of Atmospheric & Oceanic Sciences, University of California, Los Angeles, CA 90095, USA
[a]now at: California Air Resources Board, Sacramento, CA, USA
[b]now at: Center for Atmospheric and Environmental Chemistry, Aerodyne Research Inc, Billerica, MA 01821, USA
[c]now at: Sustainable Energy and Environment Thrust, The Hong Kong University of Science and Technology (Guangzhou), Guangzhou, Guangdong 511400, China
[d]now at: Louisville Metro Air Pollution Control District, Louisville, KY 40203, USA

Correspondence: Cort Anastasio (canastasio@ucdavis.edu)

Received: 21 February 2025 – Discussion started: 27 February 2025
Revised: 31 May 2025 – Accepted: 11 June 2025 – Published: 29 August 2025

Abstract. Subarctic cities notoriously experience severe winter pollution episodes with fine particle ($PM_{2.5}$) concentrations above 35 µg m^{-3}, the US Environmental Protection Agency (EPA) 24 h standard. While winter sources of primary particles in Fairbanks, Alaska, have been studied, the chemistry driving secondary particle formation is elusive. Biomass burning is a major source of wintertime primary particles, making the $PM_{2.5}$ rich in light-absorbing brown carbon (BrC). When BrC absorbs sunlight, it produces photooxidants – reactive species potentially important for secondary sulfate and secondary organic aerosol formation – yet photooxidant measurements in high-latitude $PM_{2.5}$ remain scarce. During the winter of 2022 Alaskan Layered Pollution And Chemical Analysis (ALPACA) field campaign in Fairbanks, we collected PM filters, extracted the filters into water, and exposed the extracts to simulated sunlight to characterize the production of three photooxidants: oxidizing triplet excited states of BrC, singlet molecular oxygen, and hydroxyl radical. Next, we used our measurements to model photooxidant production in highly concentrated aerosol liquid water. While conventional wisdom indicates photochemistry is limited during high-latitude winters, we find that BrC photochemistry is significant: we predict high triplet and singlet oxygen daytime particle concentrations up to 2×10^{-12} and 3×10^{-11} M, respectively, with moderate hydroxyl radical concentrations up to 5×10^{-15} M. Although our modeling predicts that triplets account for 0.4 %–10 % of daytime secondary sulfate formation, particle photochemistry cumulatively dominates, generating 76 % of daytime secondary sulfate formation, largely due to in-particle hydrogen peroxide, which contributes 25 %–54 %. Finally, we estimate triplet production rates year-round, revealing the highest rates in late winter when Fairbanks experiences severe pollution and in summer when wildfires generate BrC.

Published by Copernicus Publications on behalf of the European Geosciences Union.

1 Introduction

In 2022, Fairbanks, Alaska, was ranked the third-worst US city for fine particle ($PM_{2.5}$) pollution, averaging 30 d per year above 35 $\mu g\,m^{-3}$, the US Environmental Protection Agency (EPA) 24 h standard (Simpson et al., 2024). Like Fairbanks, cities across the Arctic and subarctic suffer from severe winter $PM_{2.5}$ pollution episodes (Arnold et al., 2016; Schmale et al., 2018; Simpson et al., 2024). These pollution events are caused by local emissions and unfavorable meteorology, where strong surface-based inversions trap locally emitted pollution in the bottom 20 m of the atmosphere (Cesler-Maloney et al., 2022; Simpson et al., 2024). While the meteorology driving pollution episodes has been characterized (Brett et al., 2025; Cesler-Maloney et al., 2024) and many of the primary sources of PM have been identified, the secondary chemical processes that form and transform PM in Fairbanks are only starting to be explored (Moon et al., 2024; Simpson et al., 2024; Sunday et al., 2025). These secondary processes can produce PM, worsening air quality, and need to be characterized for a complete understanding of PM pollution in Fairbanks (Ijaz et al., 2024; Joo et al., 2024; Mao et al., 2024; Moon et al., 2024; Sunday et al., 2025; Virtanen et al., 2010).

Winter $PM_{2.5}$ in Fairbanks is, on average, 60 % organic aerosol (OA) and 20 % sulfate (SO_4^{2-}), with the remaining 20 % a combination of elemental carbon, nitrate, ammonium, and other inorganic ions (Kotchenruther, 2016; Robinson et al., 2024; Simpson et al., 2024). The dominant sources of primary $PM_{2.5}$ – fine particles emitted directly into the atmosphere – are residential wood burning, combustion of sulfur-rich fuel oil, and vehicle emissions (Moon et al., 2024; Robinson et al., 2023; Simpson et al., 2024). Secondary $PM_{2.5}$ formation – the oxidation of gases to form low-volatility products – has also been identified as a PM source in Fairbanks (Ijaz et al., 2024; Moon et al., 2024; Robinson et al., 2024; Simpson et al., 2019). Kotchenruther (2016) reported that in Fairbanks winters, on average 12 % of OA is secondary (i.e., SOA) or aged woodsmoke OA – both formed by secondary chemistry. Similarly, during the Alaskan Layered Pollution And Chemical Analysis (ALPACA) field campaign in 2022, between 16 % and 58 % of total SO_4^{2-} was secondary (Moon et al., 2024). While it is evident that secondary PM comprises a substantial portion of winter $PM_{2.5}$ in Fairbanks, the oxidants driving this observed secondary PM formation remain unclear (Simpson et al., 2019).

In Fairbanks, the abundance of biomass burning PM indicates a strong potential for condensed-phase brown carbon (BrC) photochemistry. Biomass burning (BB) particles are rich in BrC – light-absorbing organic compounds formed during the incomplete combustion of biomass – as well as fossil fuel combustion and multiphase chemical processing (Laskin et al., 2025). When BrC chromophores absorb light, they form photooxidants – reactive species that can produce secondary sulfate and secondary organic aerosol (Jiang et al., 2021; Sunday et al., 2025; Wang et al., 2020b). We focus on three photooxidants that are important for condensed-phase reactions in woodsmoke particles: hydroxyl radical ($^{\bullet}OH$), oxidizing triplet excited states of BrC ($^3C^*$ or "triplets"), and singlet molecular oxygen ($^1O_2^*$) (Bogler et al., 2022; Chen et al., 2018; Kaur et al., 2019; Kaur and Anastasio, 2018; Lyu et al., 2023; Ma et al., 2023, 2024; Manfrin et al., 2019). As shown in Fig. 1, these photooxidants, which are formed by sunlight reactions involving brown carbon, can be significant intermediates in the formation of secondary PM species.

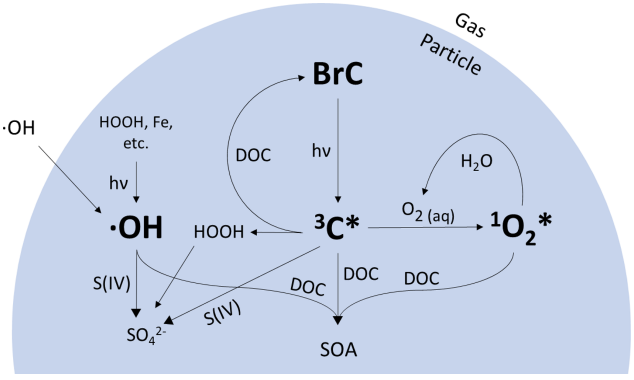

Figure 1. Schematic of condensed-phase $^{\bullet}OH$, $^3C^*$, and $^1O_2^*$ formation from brown carbon (BrC) photochemistry.

Hydroxyl radicals in aqueous droplets can be formed through a variety of mechanisms. In cloud/fog water, where the PM mass/H_2O mass ratio is between 10^{-3} and 10^{-4} (Ma et al., 2023), transport of $^{\bullet}OH$ from the gas phase is an important source of aqueous-phase $^{\bullet}OH$. In aerosol liquid water (ALW), where the PM mass/H_2O mass ratio is close to 1 (Ma et al., 2023), in situ photochemical production of $^{\bullet}OH$ becomes the dominant source (Kaur et al., 2019; Ma et al., 2023). Aqueous-phase $^{\bullet}OH$ can be produced by reactions of hydrogen peroxide with reduced iron or copper, the decomposition and photolysis of organic hydroperoxides, the photolysis of nitrate and nitrite, and as a byproduct of BrC photochemistry (Arciva et al., 2022; Gerritz et al., 2023, 2024; Tomaz et al., 2018; Tong et al., 2016). In addition, Kapur et al. (2024) report production of $^{\bullet}OH$ in dark samples from the ALPACA campaign using electron paramagnetic resonance. The dominant sink for photochemical $^{\bullet}OH$ in cloud water and ALW is dissolved organic carbon (DOC) (Arakaki et al., 2013): hydroxyl radicals react rapidly with organic compounds and can form aqueous secondary organic aerosol, which may contribute to the abundant OA observed in Fairbanks (Arciva et al., 2022; Smith et al., 2015; Yu et al., 2014). Aqueous-phase $^{\bullet}OH$ also reacts with S(IV) to form secondary SO_4^{2-}, which may contribute to the sulfate observed in Fairbanks (Seinfeld and Pandis, 2016).

Oxidizing triplet excited states of brown carbon are formed when BrC chromophores absorb sunlight, forming an electronically excited state chromophore (Kaur and Anastasio, 2018; McNeill and Canonica, 2016). ^{3}C* concentrations in the atmosphere were first measured in cloud and fog drops, but recent work showed much higher levels in ALW (Kaur and Anastasio, 2018; Ma et al., 2023). These results suggest that triplets are kinetically competitive against other particle oxidants like $^\bullet$OH and indicate the strong potential for ^{3}C*-driven chemistry in particles (Ma et al., 2023). Specifically, triplets might be an important oxidant in secondary SO_4^{2-} formation in BrC-rich aerosols due to in situ particle chemistry and surface reactions (Wang et al., 2020b; Liang et al., 2024). They can also rapidly convert phenols to aqueous SOA in drops and particles (Jiang et al., 2023b, a; Ma et al., 2021, 2024; Smith et al., 2014, 2016; Yu et al., 2014; Zhang et al., 2022) and form secondary oxidants such as phenoxy radicals, which may drive additional chemistry (Remke et al., 2022).

The third photooxidant of interest in BrC-rich particles is singlet molecular oxygen, which is produced when triplets transfer their energy to dissolved oxygen (Fig. 1; Appiani and McNeill, 2015). Of the three photooxidants discussed here, $^1O_2$* is predicted to exhibit the highest steady-state concentrations in ALW, roughly 10 times higher than those of triplets and 100–1000 times higher than those of aqueous $^\bullet$OH (Kaur et al., 2019; Ma et al., 2023). Interestingly, the concentration of $^1O_2$* is highly dependent on the type of BrC and varies greatly among BrC sources (Jiang et al., 2023a; Ma et al., 2024; Manfrin et al., 2019). While $^1O_2$* concentrations in ALW are higher than those of ^{3}C* and $^\bullet$OH in ALW, singlet oxygen is also more selective: $^1O_2$* reacts with fewer organic species and with slower reaction rates than ^{3}C* and $^\bullet$OH (Manfrin et al., 2019). Nonetheless, in ALW, singlet oxygen can be a significant sink for some organic species and might also be important for aqueous SOA formation (Ma et al., 2023; Manfrin et al., 2019).

Given the potential importance of photooxidants and the lack of measurements, our goal is to quantify photooxidant production in wintertime particles from a high-latitude site to understand their role in multiphase chemical processing during severe winter pollution events. First, we measure the photolytic production of aqueous-phase $^\bullet$OH, ^{3}C*, and $^1O_2$* in dilute extracts of $PM_{2.5}$ collected in Fairbanks during ALPACA. We then use these extract measurements to model photooxidant production in aerosol liquid water to understand wintertime photooxidant production in biomass burning PM. To explore how ^{3}C* and other oxidants contribute to chemical processing in particles, we first assess the lifetimes of various organic species due to $^\bullet$OH, ^{3}C*, and $^1O_2$*. We next build a kinetic model to estimate the importance of triplet excited states and other oxidants in the formation of secondary sulfate. Lastly, we predict ^{3}C* production in particles throughout the year in Fairbanks to assess the overall potential for ^{3}C* chemistry.

2 Methods

2.1 Chemicals

Syringol (SYR; 99 %), furfuryl alcohol (FFA; 98 %), benzoic acid (BA; $\geq$ 99.5 %), *p*-hydroxybenzoic acid (*p*-HBA; 99 %), 3,4-dimethoxybenzaldehyde (DMB; 99 %), and methanol (MeOH; $\geq$ 99.5 %) were received from Millipore Sigma. Chemical solutions and particulate matter extracts (PMEs) were prepared using air-saturated ultrapure water (Milli-Q water) from a Milli-Q Advantage A10 system (Millipore; $\geq$ 18.2 MΩ cm) that was pretreated with a Barnstead activated carbon cartridge. pH was adjusted with TraceMetal™ grade concentrated sulfuric acid (Fisher Scientific, 18.4 M).

2.2 Sample collection, extraction, and storage

Between 13 January and 25 February 2022, high-volume 24 h filter samples of ambient particles were collected at two separate sites in Fairbanks: a residential location designated as the "house" site and the University of Alaska Fairbanks Community & Technical College in downtown Fairbanks, called the "CTC" site (Simpson et al., 2024). We collected $PM_{2.5}$ at the house site and $PM_{0.7}$ (particulate matter $\leq$ 2.5 and $\leq$ 0.7 µm in diameter, respectively) at the CTC site. Details regarding filter collection at the house and CTC sites are outlined in Edwards et al. (2024) and Moon et al. (2024), respectively, and in Sect. S1 in the Supplement. While we measured photooxidants on all house site composites, we only performed a few measurements of photooxidants using the CTC composites and instead used them to perform the dilution series experiment (outlined below), to explore site differences, and to examine pH differences.

The 24 h filters were compiled into multiday composites, with each composite named with its midpoint date (Table S1, Fig. 2). To prepare PMEs, filters were first cut into 2 × 2 cm squares (with several squares cut from each filter), placed in individual 20 mL amber bottles, and submerged in 1.0 mL of solvent. For a given composite, we used an equal number of filter squares from each filter to ensure that each day was equally represented. In other words, we controlled the ratio of filter area from each individual filter to the total area of filter extracted to create a composite. Filters were extracted in Milli-Q water, 50 mM sulfuric acid (pH 1.3, henceforth referred to as pH 1), or 10 µM sulfuric acid (pH 4.7, henceforth referred to as pH 5). House site filters were extracted into only Milli-Q water and pH 1, while some CTC site filters were extracted into pH 5 in addition to Milli-Q water and pH 1. The two concentrations of sulfuric acid were selected to mimic the high- and low-pH values predicted in aerosol liquid water by Campbell et al. (2024b). The filters in solution were shaken for 4 h in the dark, after which the filter squares were removed and extracts in a given solvent were combined. For each filter, we made up two to three differ-

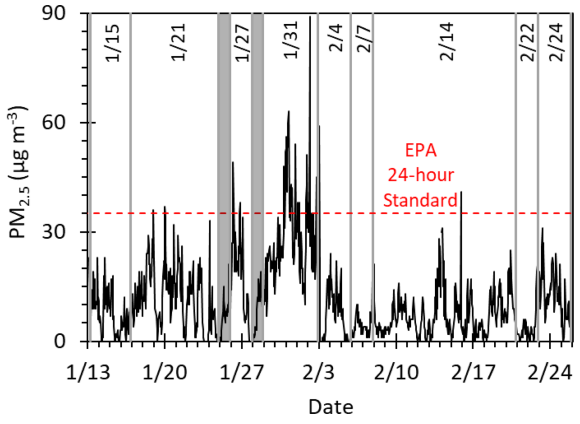

Figure 2. Hourly average $PM_{2.5}$ mass concentrations in downtown Fairbanks (NCore site; Simpson et al., 2024) for the ALPACA campaign of winter 2022. Grey lines delineate each composite, labeled with its midpoint date, while grey-shaded days were used for initial testing and were not part of a composite (see Table S1 for collection times). The dashed red line marks the EPA 24 h $PM_{2.5}$ standard.

ent extracts: Milli-Q; pH 1; and, for some filters, pH 5. The extracts were filtered (0.22 µm PTFE; Pall); their pH values were measured (Table S2); and for pH 5 extracts, which generally had an initial pH above 5, additional sulfuric acid was added to adjust to within 0.2 pH units of pH 5. The solutions were then flash-frozen in liquid nitrogen and stored in a −20 °C freezer until further use. The pH 1 and pH 5 particle extracts were used to measure photooxidant production, UV–Vis absorbance spectra, and concentrations of water-soluble transition metals, while parallel Milli-Q extracts were used to determine concentrations of total solutes, DOC, and ions.

2.3 General sample composition

The UV–Vis absorbance spectrum of each composite was measured with a Shimadzu UV-2501PC spectrophotometer in a 1 cm quartz cuvette. The pH of each extract from every composite was measured using a microelectrode (MI-414 series, protected tip; Microelectrodes, Inc.). The DOC concentration of each composite was measured using a Shimadzu total organic carbon analyzer (TOC-V CSH). Dissolved metal concentrations of each composite were measured using an Agilent Technologies triple-quadrupole 8900 inductively coupled plasma mass spectrometer. The concentrations of major ions of each composite were measured using ion chromatography (Dionex ICS-6000) (Sunday et al., 2025).

2.4 Illumination experiments

Illumination experiments were performed as outlined in Ma et al. (2024) and are briefly reviewed here. Tropospheric sunlight was simulated with a 1000 W Xenon arc lamp with three downstream optical filters: a water filter, an AM1.0 air mass filter (AM1D-3L, Sciencetech), and a 295 nm long-pass filter (20CGA-295, Thorlabs; see Fig. S1 for the simulated sunlight spectrum; Kaur and Anastasio, 2018; Ma et al., 2023; Sunday et al., 2025). All illuminations were performed in 1 mL GE 021 quartz tubes (5 mm inner diameter). On each experiment day, the photolysis rate constant of 10 µM of 2-nitrobenzaldehyde ($j_{2NB,EXP}$) was measured and used to determine the daily photon flux in the solar simulator (Galbavy et al., 2010). Values of $j_{2NB,EXP}$ ranged from 0.018 to 0.026 s^{-1} (decay plots are shown in Fig. S2); all laboratory oxidant production rates and concentrations reported in this work were normalized to a standard $j_{2NB,AK}$ of 0.0045 s^{-1}, a value representative of the Fairbanks midday actinic flux on 1 February 2022 using actinic sunlight modeled by the Tropospheric Ultraviolet and Visible (TUV) radiation model (Madronich and Flocke, 1998). This $j_{2NB,AK}$ value also includes an enhancement factor of 2.5 to account for optical confinement (described in Sect. 3.1) (Corral Arroyo et al., 2022). Light screening, i.e., the attenuation of photons through the reaction tube, was quantified using a screening factor (S_λ) (Sect. S2). The rate of light absorbance by PM extracts in the solar simulator was calculated as described in Sect. S3.

2.5 Photooxidant measurements

Steady-state concentrations of $^{\bullet}OH$, $^3C^*$, and $^1O_2^*$ were measured under laboratory conditions with widely used probe methods (Anastasio and McGregor, 2001; Appiani et al., 2017; Appiani and McNeill, 2015; Kaur et al., 2019; Kaur and Anastasio, 2018; Ma et al., 2022). Benzoic acid, syringol, and furfuryl alcohol were used to measure $^{\bullet}OH$, oxidizing $^3C^*$, and $^1O_2^*$, respectively, by quantifying the loss of the probes during illumination. For benzoic acid, we also monitored the formation of a product, *p*-HBA (Sect. S4). For each experiment, 1.0 mL of particulate matter extract was spiked with 10 µM of a probe (P), held at 10 °C, and illuminated. Solutions were not stirred since the entire solution was illuminated, but solutions were shaken vigorously prior to illumination and sampling to ensure homogeneity. At five designated time points, a 130 µL aliquot was removed, and the probe concentration was determined using high-pressure liquid chromatography (HPLC; Shimadzu LC-20AB pump, Thermo Scientific Accucore XL C18 column (50 × 3 mm, 4 µm bead), and Shimadzu-M20A photodiode array detector). The probe decay was then fit with the following first-order kinetic equation:

$$\ln\frac{[P_t]}{[P_0]} = -k'_P t, \quad (1)$$

where t is time, $[P_t]$ is the probe concentration at time t, $[P_0]$ is the initial probe concentration, and k'_P is the measured pseudo-first-order rate constant for probe loss (raw data are shown in Fig. S2). Here k'_P is corrected for internal light

screening and normalized to a $j_{2NB,AK}$ of 0.0045 s^{-1} using

$$k'_{P,EXP} = \frac{k'_P\, 0.0045}{S_\lambda\ j_{2NB,EXP}}, \quad (2)$$

where $k'_{P,EXP}$ is the normalized pseudo-first-order rate constant for P loss, and S_λ is the screening factor. Parallel dark control experiments were performed by measuring probe concentrations in a quartz tube containing the particulate matter extract spiked with all three probes and wrapped in aluminum foil. No probe loss was observed in the dark samples. Using the experimental k'_P, the steady-state oxidant concentrations and oxidant production rates were calculated using the methods described in Sects. S4 and S5 and rate constants from Table S3. Finally, the quantum yield (Φ_{Ox}) of each oxidant in our dilute extracts was determined by

$$\Phi_{Ox} = \frac{P_{Ox,EXP,PME}}{R_{abs,EXP,PME}}, \quad (3)$$

where $P_{Ox,EXP,PME}$ is the production rate of a given oxidant, and $R_{abs,EXP,PME}$ is the rate of light absorbance of our PMEs (Sect. S3), both under laboratory experimental conditions with a standard photon flux of $j_{2NB,AK} = 0.0045\ s^{-1}$.

2.6 Predicting photooxidant concentrations in aerosol liquid water of Fairbanks particles

2.6.1 Sunlight in Fairbanks

Throughout ALPACA, the downwelling spectral actinic flux (310–700 nm) was measured every 8 min using a diode array actinic flux spectroradiometer (MetCon GmbH) at the NCore site in downtown Fairbanks (calibrated prior to the ALPACA campaign). To quantify albedo, upwelling and downwelling j_{NO2} values were measured at 1 min intervals using a filter radiometer (MetCon GmbH, calibrated after the ALPACA campaign). The upwelling-to-downwelling ratio of j_{NO2} was calculated and applied to the downwelling spectral actinic flux to estimate the total (i.e., upwelling and downwelling) actinic flux. Using these data, we calculated the daily peak 3 h average actinic flux ($I_{\lambda,AK}$). We then averaged the daily peak 3 h $I_{\lambda,AK}$ over each composite to calculate an $I_{\lambda,AK}$ representative of the peak 3 h average sunlight condition for each composite. The rate of light absorbance ($R_{abs,AK,ALW}$, mol L^{-1} s^{-1}) of BrC in Fairbanks particles was then calculated with

$$R_{abs,AK,ALW} = [DOC]_{ALW} \times \sum_{310}^{550} \left[MAC_\lambda \times I_{\lambda,AK} \times \Delta\lambda \times 10^{-3}\right] \times (a+1) \times 2.5, \quad (4)$$

where $[DOC]_{ALW}$ is the water-soluble DOC concentration predicted for ALW conditions (mg L^{-1}), MAC_λ is the DOC-normalized mass absorption cross section at wavelength λ (cm^2 g^{-1}), $I_{\lambda,AK}$ is the composite-average peak 3 h actinic flux based on measurements during ALPACA (mol photons cm^{-2} nm^{-1} s^{-1}), $\Delta\lambda$ is the wavelength interval between discreet $I_{\lambda,AK}$ values (1 nm), the 10^{-3} factor is a unit conversion of g to mg, a is the albedo, and 2.5 is a factor that accounts for optical confinement (Corral Arroyo et al., 2022; Kaur et al., 2019). We defined our ALW conditions based on the ALW concentrations reported by Campbell et al. (2024b) modeled using ISORROPIA-II during the ALPACA campaign. DOC concentrations in ALW were calculated as described in Sect. S6.

2.6.2 Dilution series

To predict the steady-state concentrations of $^{\bullet}OH$, $^3C^*$, and $^1O_2^*$ in aerosol liquid water in Fairbanks, we first characterized how oxidant concentrations changed with solution concentration (Kaur et al., 2019; Ma et al., 2023). We performed a dilution experiment on the 14 February CTC composite. We prepared five separate particulate matter extracts, extracting the 2 × 2 cm filter squares into different volumes of solution to obtain a sequence of dilutions (prepared in pH 1, with parallel Milli-Q extracts prepared for the three most dilute samples). Compared to the standard particulate matter extract, where a 2 × 2 cm filter square was extracted into 1.0 mL of solution, the five dilution series extracts were prepared with solution volumes equal to extracting each 2 × 2 cm filter square into 10.0, 2.0, 0.70, 0.40, and 0.30 mL of solution. For the three most dilute extracts, we extracted the filters into 50 mM H_2SO_4 (pH 1.3). For the 0.40 mL per square and 0.30 mL per square extractions, we extracted the filter squares into 1.0 mL of 0.020 and 0.015 M H_2SO_4, respectively. We then used rotary evaporation to concentrate the extracts (removing 60 % and 70 % of the water for the 0.40 and 0.30 mL samples, respectively), a technique described and validated by Ma et al. (2024). The final extracts had H_2SO_4 concentrations of roughly 50 mM, which was verified with pH measurements (i.e., pH 1.3). We then measured the $^{\bullet}OH$, $^3C^*$, and $^1O_2^*$ concentrations in each of the five extracts to understand how photooxidant concentrations change as a function of extract concentration. We also measured DOC in all five extracts (in Milli-Q extracts of the three most dilute samples and in pH 1 PME for the two concentrated samples) and water-soluble metals and ions in the Milli-Q extracts of the three most dilute samples to validate that DOC, ions, and metals all changed linearly with the dilution (Sunday et al., 2025); there was insufficient sample volume to measure metals and ions in the two most concentrated samples.

2.6.3 Modeling photooxidant production in aerosol liquid water

We extrapolated steady-state concentrations of $^{\bullet}OH$, $^3C^*$, and $^1O_2^*$ in aerosol liquid water from our particle extract results using the kinetic models developed by Ma et al. (2024) and Kaur et al. (2019). The model was based on the definition

of steady-state concentration:

$$[\mathrm{Ox}] = \frac{P_{\mathrm{Ox}}}{k'_{\mathrm{Ox}}}, \tag{5}$$

where the oxidant concentration ([Ox]) is equal to the ratio of the production rate (P_{Ox}) to the pseudo-first-order rate constant for oxidant loss (k'_{Ox}). We used DOC concentration as a proxy for aerosol liquid water content (ALWC), with higher DOC concentrations corresponding to lower ALWC (Ma et al., 2023). For the dilution series composite, we calculated P_{Ox}, k'_{Ox}, and oxidant concentrations at a wide range of liquid water content, from fog/cloud drops to particle water; for all other composites, we only determined these values under ALW conditions.

We modeled the steady-state $^{\bullet}$OH concentration in ALW by calculating both the $^{\bullet}$OH production rate ($P_{\bullet\mathrm{OH,ALW}}$) and the major $^{\bullet}$OH sink ($k'_{\bullet\mathrm{OH,ALW}}$). Laboratory experiments determined that $P_{\bullet\mathrm{OH,PME}}$ is proportional to DOC (Kaur et al., 2019; Ma et al., 2023), which we verified for our samples in the dilution series experiment. As such, we assumed the quantum yield determined in the dilute particle extracts under laboratory-simulated sunlight, $\Phi_{\bullet\mathrm{OH}}$, was constant across cloud/fog and ALW conditions. $P_{\bullet\mathrm{OH,ALW}}$ was calculated with

$$P_{\bullet\mathrm{OH,ALW}} = \Phi_{\bullet\mathrm{OH}} \times R_{\mathrm{abs,AK,ALW}}, \tag{6}$$

where $R_{\mathrm{abs,AK,ALW}}$ is the rate of light absorbance in ALW conditions under Fairbanks sunlight. We estimate the contribution of $^{\bullet}$OH in particles from gas-phase $^{\bullet}$OH mass transport using the Fuchs–Sutugin transition regime theory (Seinfeld and Pandis, 2016; Tables S4, S5, S6). The total aqueous-phase $P_{\bullet\mathrm{OH,ALW}}$ was the combined rate of photochemical $^{\bullet}$OH formation inside particles and uptake rate of $^{\bullet}$OH from the gas phase. We calculate the sink for $^{\bullet}$OH considering only reactions with DOC ($k_{\mathrm{DOC}+\bullet\mathrm{OH}} = 3.8(\pm1.9) \times 10^8\ \mathrm{L\,mol\,C^{-1}\,s^{-1}}$; Arakaki et al., 2013) since this was the dominant loss for $^{\bullet}$OH under dilute and ALW conditions (Arakaki et al., 2013; Kaur et al., 2019; Ma et al., 2023). Once $P_{\bullet\mathrm{OH,ALW}}$ and $k'_{\bullet\mathrm{OH,ALW}}$ were determined, the $^{\bullet}$OH concentration was calculated using Eq. (5).

Similar to $P_{\bullet\mathrm{OH,PME}}$, laboratory experiments have shown that $P_{3\mathrm{C*,PME}}$ is also proportional to solute concentration, which we tested with our dilution series samples (Kaur et al., 2019; Ma et al., 2023). $P_{3\mathrm{C*,ALW}}$ was calculated with an equation analogous to Eq. 6, instead using $\Phi_{3\mathrm{C*}}$. The rate constant for triplet loss in ALW ($k'_{3\mathrm{C*,ALW}}$) was estimated by considering three sinks for triplets: energy transfer to dissolved O_2, chemical reaction with DOC, and physical quenching by DOC (Ma et al., 2024). The average second-order rate constant for the reaction of ^{3}C* with O_2 ($k_{\mathrm{O2+3C*}}$) was estimated by Kaur et al. (2019) as $2.8 \times 10^9\ \mathrm{M^{-1}\,s^{-1}}$. The concentration of O_2 in Fairbanks particle water was estimated using the temperature-dependent Henry's law constant and composite-averaged temperature measurements, assuming negligible influence of ionic strength (Seinfeld and Pandis, 2016). The second-order rate constant for reaction and quenching of oxidizing ^{3}C* with DOC ($k_{\mathrm{rxn+Q,3C*,SYR}}$) measured in biomass burning PM extracts with the syringol (SYR) probe was $7 \times 10^7\ \mathrm{M^{-1}\,s^{-1}}$ (Ma et al., 2024). Once $k'_{3\mathrm{C*,ALW}}$ was calculated, the ^{3}C* concentration was predicted using Eq. (5).

While $P_{1\mathrm{O2*,PME}}$ increased linearly with DOC concentration in PM extracts, which are dilute, Ma et al. (2023) have shown that the production rate plateaus at the high DOC concentrations of ALW. We captured this behavior in $P_{1\mathrm{O2*}}$ across both PME and ALW conditions using the formulation from Ma et al. (2024):

$$P_{1\mathrm{O2*}} = \frac{\frac{\Delta P_{1\mathrm{O2*}}}{\Delta \mathrm{DOC}} \times [\mathrm{DOC}]}{1 + \left(\frac{k_{\mathrm{rxn+Q,3C*,FFA}}[\mathrm{DOC}]}{k_{\mathrm{O2+3C*}}[\mathrm{O_2}]}\right)}, \tag{7}$$

where $\frac{\Delta P_{1\mathrm{O2*}}}{\Delta \mathrm{DOC}}$ is the ratio of the $^1O_2$* production rate to DOC concentration for a given sample in dilute solutions, and $k_{\mathrm{rxn+Q,3C*,FFA}}$ is the second-order rate constant for reaction and quenching of the entire pool of ^{3}C* by DOC as measured with furfuryl alcohol (FFA) ($1 \times 10^7\ \mathrm{M^{-1}\,s^{-1}}$; Ma et al., 2024). We then calculated the pseudo-first-order rate constant for $^1O_2$* loss by using two $^1O_2$* sinks: quenching by water ($k'_{1\mathrm{O2*,H2O}} = 2.76(\pm0.02) \times 10^5\ \mathrm{s^{-1}}$, Appiani et al., 2017) and reaction with DOC ($k_{1\mathrm{O2*+DOC}} = 1 \times 10^5\ \mathrm{M^{-1}\,s^{-1}}$, Ma et al., 2023). The $^1O_2$* concentration was then predicted using Eq. (5).

3 Results and discussion

To assess the role of brown-carbon-mediated photochemistry during winter in Fairbanks, Alaska, we measured photooxidant production in nine composites of $PM_{2.5}$ filter samples collected at the house and CTC sites during the 6-week ALPACA field campaign (Fig. 2, Table S1). During the campaign, the composite-average temperature at the CTC site ranged from −31 to −5 °C, and the composite-average relative humidity ranged from 75 % to 90 % (Table S7; relative humidity was measured by the AK Department of Transportation < 1.5 km from the CTC site). The most polluted period during the ALPACA campaign is captured by the 31 January composite (29 January to 3 February), with a peak hourly average $PM_{2.5}$ of $89\ \mu\mathrm{g\,m^{-3}}$ and a composite-average $PM_{2.5}$ concentration of $27\ \mu\mathrm{g\,m^{-3}}$ (Fig. 2). The pollution episode exhibited low temperatures and high relative humidity, with a composite-average temperature of −31 °C and relative humidity of 75 %. Details of each sample composite, including the sample collection time period, average $PM_{2.5}$ concentration, ambient temperature, relative humidity, albedo, and peak 3 h composite-averaged actinic flux are listed in Table S7.

3.1 Is condensed-phase photochemistry possible in the winter in Fairbanks?

Conventional wisdom holds that photochemical oxidant generation, such as •OH formation from ozone photolysis, is slow and generally unimportant in high latitudes during winter. We sought to assess this for brown carbon photochemistry by examining whether BrC might be a significant source of winter oxidants in Fairbanks particles. Figure 3a compares the absorption cross sections of gas-phase O_3 and HONO and particulate BrC from the 31 January house sample. Ozone absorbs very little wintertime sunlight, confirming its lack of photochemical activity during ALPACA. However, both HONO and BrC absorb sunlight significantly at longer wavelengths, suggesting they are likely sources of wintertime oxidants.

Figure 3b compares the per-molecule (or for BrC, per-carbon-atom) light absorbance rates of BrC, O_3, and HONO. Three factors enhance BrC photochemistry in Fairbanks' low-sunlight environment. First, BrC significantly absorbs visible light ($\lambda > 400$ nm), while O_3 and HONO do not. Moreover, BrC and HONO both have significant UV-A absorbance and are therefore less impacted by the suppression of UV-B photons in winter sunlight, which limits O_3 photolysis (Seinfeld and Pandis, 2016). Second, Corral Arroyo et al. (2022) report a 2- to 3-fold enhancement of the photon flux inside particles due to optical confinement, which impacts particle-phase BrC but not gas-phase HONO or O_3 (the factor of 2.5 is included in Fig. 3b and in all ALW calculations). Third, sunlight during the winter in Fairbanks is enhanced by albedo: the composite-average ($\pm 1\sigma$) measured upwelling-to-downwelling ratio during the peak 3 h of daylight was 0.85($\pm$0.07) (Table S7), affecting all photochemistry. BrC absorbs 8 times more light than HONO and 1000 times more light than O_3 on a per-molecule (or per-carbon-atom) basis (Fig. 3b), demonstrating the strong potential for BrC-mediated photochemistry.

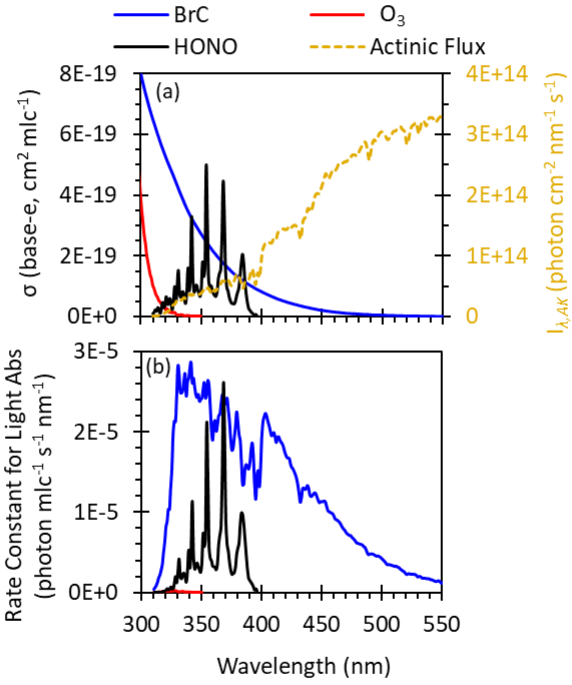

Figure 3. **(a)** Base-e absorption coefficients for particulate BrC (31 January composite, expressed in units of per carbon atom of DOC) and gas-phase O_3 and HONO (Finlayson-Pitts and Pitts, 2000), overlaid with the measured total photon flux ($I_{\lambda,\mathrm{AK}}$) at solar noon for the 31 January polluted period. **(b)** Rate constant of light absorption of BrC (per carbon atom), O_3 (per molecule), and HONO (per molecule). The ozone result is indistinguishable from the x axis. The brown carbon result includes a factor of 2.5 enhancement of $I_{\lambda,\mathrm{AK}}$ due to optical confinement within particles (Sect. 3.1).

3.1.1 Subarctic winter sunlight

Next, we explore how the intensity of sunlight changes throughout the campaign. Figure 4a compares the actinic flux at solar noon measured during ALPACA to predictions by the Tropospheric Ultraviolet and Visible (TUV) radiation model run with standard clear-sky conditions (Madronich and Flocke, 1998; TUV parameters in Table S8). The ratio of measured-to-modeled actinic flux ranged from 0.31 to 1.28, with an average ($\pm 1\sigma$) of 0.62($\pm$0.33). For periods when TUV underestimates the measurements, the error is likely because the 0.85 albedo used in our TUV input underestimates the midday albedo, which was often close to 1. For periods where TUV overestimates the measurements, we attribute this to cloudiness not accounted for in our TUV inputs. This is in line with the 50 %–70 % reduction in actinic flux observed below clouds in previous work (Crawford et al., 2003). The most significant difference between measured and TUV-modeled actinic fluxes is at short wavelengths, where the model overpredicts the flux (Fig. S3). This is important for species like O_3 that absorb light solely at short wavelengths, but it has less of an impact on species such as BrC, which absorb light strongly into the visible region (Fig. 3).

3.1.2 Light-absorbing properties of BrC

The composite-average DOC (Sect. S6) at the house site peaked during the 31 January pollution event at 4 µgC m^{-3} and averaged ($\pm 1\sigma$) 2.2($\pm$0.8) µgC m^{-3} across the campaign (Fig. 4b). In our samples, the average ($\pm 1\sigma$) mass absorption coefficient at 300 nm (MAC_{300}) is 3.3($\pm$0.8) m^2 gC^{-1}, and the average ($\pm 1\sigma$) absorption Ångström exponent (AAE; 300–450 nm) is 9.4($\pm$0.6) (Fig. S4 and Table S9). For the composites where we measured the MAC at both the house and the CTC sites, we see only minor differences between the two sites (Table S9). While MAC_{300} is consistent throughout the campaign, MAC_{365} decreases ($p < 0.05$), suggesting photobleaching becomes more important as daylight hours

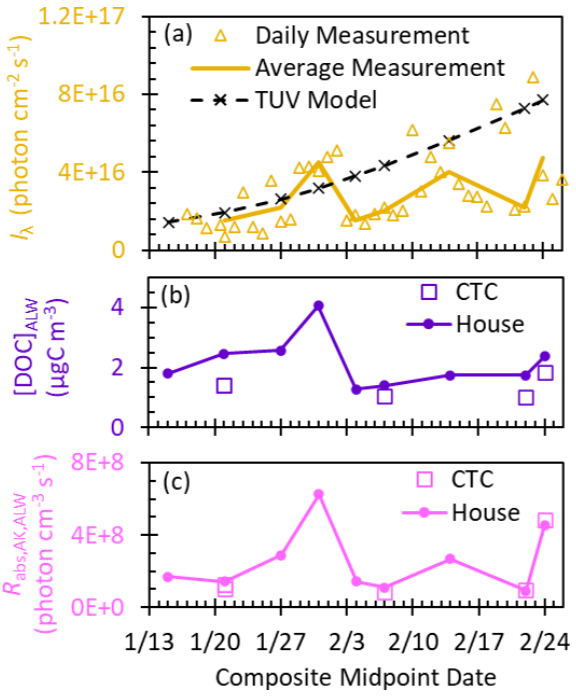

Figure 4. **(a)** Daily measured total (upwelling and downwelling) actinic flux ($I_{\lambda,AK}$) summed from 310 to 550 nm measured at solar noon (gold triangles) and the corresponding midday values averaged for each composite (gold line). TUV-modeled $I_{\lambda,AK}$ summed from 310 to 550 nm at solar noon at the midpoint day of each composite (dashed black line), using an albedo of 0.85. All $I_{\lambda,AK}$ values here are for the gas phase and are not affected by in-particle enhancement from optical confinement. **(b)** Dissolved organic carbon concentrations calculated in ALW (Sect. S6) at the two sampling locations (house and CTC). **(c)** Rate of light absorbance by DOC per volume of ALW using the measured 3 h midday $I_{\lambda,AK}$ average for each composite. For the 15 January composite, $I_{\lambda,AK}$ was not measured, and so the modeled $I_{\lambda,AK}$ was used. $R_{abs,AK,ALW}$ values account for the factor of 2.5 enhancement due to optical confinement in particles.

increase (Laskin et al., 2015). Our MAC and AAE values are very similar to other urban polluted regions where residential wood burning is abundant (Li et al., 2020) and are slightly higher than values reported for wildfire-dominated samples (Bali et al., 2024; Jiang et al., 2023a; Ma et al., 2023). Since the MAC values of BrC from gasoline exhaust are a factor of 2 lower than those of woodsmoke BrC, our data suggest gasoline vehicles are not a dominant source of BrC during ALPACA (Xie et al., 2017). We also characterized our BrC with E2/E3, i.e., the ratio of absorbance at 250 nm to that at 365 nm (Helms et al., 2008; Peuravuori and Pihlaja, 1997). While E2/E3 values in aqueous $PM_{2.5}$ extracts have been reported between 4.2 and 17 (Ma et al., 2024), our sample values inhabit a small range, from 5.8 to 8. Low E2/E3 values correspond to high-molecular-weight compounds, indicating their ubiquity in our samples (Helms et al., 2008; Ma et al., 2024; Ossola et al., 2021; Peuravuori and Pihlaja, 1997). High-molecular-weight compounds are associated with fresh biomass burning OA (Farley et al., 2022; Ma et al., 2024), indicating the abundance of fresh BrC. This is further corroborated by the short (1.5–3 h) lifetime of particles during pollution events (Cesler-Maloney et al., 2024) and by source apportionment of ALPACA OA, finding that fresh and lightly aged wood burning OA on average account for 47 % of the total measured OA (Ijaz et al., 2024).

3.1.3 Brown carbon light absorbance

By combining the measured actinic fluxes ($I_{\lambda,AK}$), the water-soluble organic carbon concentration, and the MAC_λ of DOC, we calculated the rate of light absorption by water-soluble chromophores in particles in Fairbanks during the peak 3 h of daylight, when photochemistry is most active (Fig. 4c). The peak 3 h average $R_{abs,AK,ALW}$ is 39 %–88 % of the value at solar noon. The rate shows no notable trend across the campaign (Fig. 4c): this is a result of highly variable measured actinic fluxes due to variable cloudiness, a small decrease in soluble organic aerosol concentrations from January to February, some photobleaching of BrC, and a peak in the rate of light absorption during the pollution episode. This elevated $R_{abs,AK,ALW}$ for the 31 January composite indicates heightened potential for BrC-mediated photochemistry during the pollution episode.

3.2 Measurements of photooxidant production in PM extracts

Under laboratory-simulated sunlight, all particle extracts produce significant concentrations of $^{\bullet}OH$, $^3C^*$, and $^1O_2^*$. Figure 5 presents particle extract results normalized to a standard Fairbanks winter photon flux, providing insight into the capacity of water-soluble chromophores to produce photooxidants in each sample (details are in Tables S10 and S11). The average ($\pm 1\sigma$) DOC concentration in PME is $2.6(\pm 0.8) \times 10^{-3}$ M, which is 3–4 orders of magnitude lower than aerosol liquid water but similar to DOC concentrations of cloud and fog droplets (Kaur et al., 2019; Ma et al., 2023).

3.2.1 Hydroxyl radical in PM extracts

Hydroxyl radical concentrations are variable throughout the field campaign (Fig. 5a). The $^{\bullet}OH$ concentration peaks during the 31 January pollution episode at a value 6 times higher than the lowest value. $^{\bullet}OH$ concentrations at pH 1 are moderately correlated with DOC concentration ($R^2 = 0.47$, p value < 0.01) and poorly correlated with $PM_{2.5}$ concentration ($R^2 = 0.28$, p value < 0.01), though both correlations are stronger than those reported in past work for biomass burning samples (Fig. S5) (Kaur et al., 2019; Ma et al., 2023). The correlation of $^{\bullet}OH$ with DOC is unexpected: past studies have found that $^{\bullet}OH$ concentrations do not increase

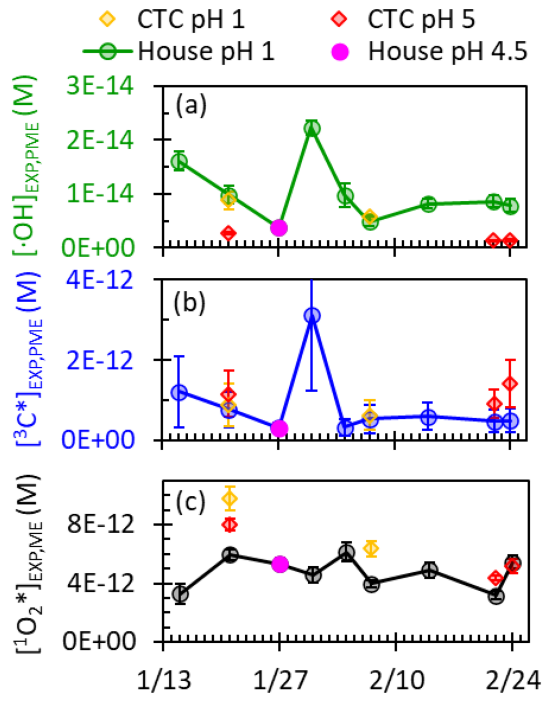

Figure 5. Steady-state concentrations of **(a)** $^{\bullet}$OH, **(b)** ^{3}C*, and **(c)** $^{1}O_2$* in particle extracts measured under laboratory-simulated sunlight and normalized to actinometric conditions of $j_{2NB,AK} = 0.0045\,s^{-1}$, the Fairbanks midday photon flux modeled by TUV on 1 February 2022. Samples were collected from two different sites (house and CTC) and were extracted at two different pH values (pH 1 and 4.5/5). The error bars represent the error propagated from each component of the calculation, including the regression to determine k'_P and the rate constants with each probe. The ^{3}C* concentrations have the highest errors, mostly due to large errors in the rate constant of the syringol probe with ^{3}C* at low pH.

with DOC because DOC is the dominant $^{\bullet}$OH sink (Kaur et al., 2019; Ma et al., 2023). Instead, our observed correlation suggests that DOC is an $^{\bullet}$OH source (Gerritz et al., 2023) or an $^{\bullet}$OH precursor (e.g., through HOOH formation by BrC; Anastasio et al., 1997) or that DOC is correlated with other sources of $^{\bullet}$OH (Ma et al., 2024; Mao et al., 2013). To understand our $^{\bullet}$OH sources, we compared our measured $^{\bullet}$OH formation rates with calculated nitrate and nitrite photolysis rates based on measurement of inorganic ions, as well as the HOOH formation rate measured by Sunday et al. (2025) (Table S12). While nitrite and nitrate photolysis are negligible, the rate of HOOH formation is large enough to account for all $^{\bullet}$OH formed in our PM extracts. Furthermore, there is a strong correlation between $P_{\bullet OH,EXP,PME}$ and $P_{HOOH,EXP,PME}$ ($R^2 = 0.93$, p value < 0.1; Fig. S6a) and a notable correlation between $^{\bullet}$OH and water-soluble Fe ($R^2 = 0.47$, p value < 0.01; Fig. S6b). This suggests that photo-Fenton reactions of HOOH with metals are a major $^{\bullet}$OH source (Anastasio and McGregor, 2001; Arciva et al., 2022; Kaur et al., 2019; Ma et al., 2024; Tong et al., 2016). Further evidence can be seen in the strong pH dependence of $^{\bullet}$OH concentrations: values at pH 5 for CTC particles are 15 %–30 % of their pH 1 house site counterparts, in line with the lower Fe concentrations and slower rates of HOOH production at pH 5 compared to pH 1 (Sunday et al., 2025).

3.2.2 Triplet excited states of brown carbon in PM extracts

The triplet concentrations show strong differences between clean and polluted periods (Fig. 5b). ^{3}C* concentrations peak during the pollution episode and are low during clean periods when DOC concentrations are low. We observe no statistically significant pH dependence or site difference for ^{3}C*. Concentrations of ^{3}C* and $^{1}O_2$* are poorly correlated ($R^2 = 0.04$, p value < 0.01), a surprising observation because singlet oxygen is produced from triplets. The lack of correlation might be caused by the specificity of the syringol probe, which only quantifies the oxidizing subset of the ^{3}C* population, while $^{1}O_2$* is produced from the total ^{3}C* population (Bodesheim et al., 1994; Ma et al., 2022; Schweitzer et al., 2003). In general, we find that high DOC concentrations during pollution events lead to high ^{3}C* concentrations, indicating the strong potential for triplet-driven chemistry.

3.2.3 Singlet molecular oxygen in PM extracts

The $^{1}O_2$* concentrations in the house particle extracts do not change significantly across the campaign (Fig. 5c). The few samples from the CTC site and at pH 5 suggest that $^{1}O_2$* generation is similar between the sites and relatively independent of acidity. Surprisingly, we found poor correlations between $^{1}O_2$* concentration and $PM_{2.5}$ ($R^2 = 0.01$, p value < 0.01) and DOC ($R^2 = 0.11$, p value < 0.01; Fig. S5). During the 31 January pollution episode, where $PM_{2.5}$ and DOC peaked, $^{1}O_2$* did not increase, while concentrations of $^{\bullet}$OH and ^{3}C* were both enhanced during the pollution event. We expected enhanced $^{1}O_2$* concentrations for the pollution event because the concentrations of BrC driving $^{1}O_2$* formation are heightened, suggesting $P_{^1O_2^*}$ should increase, while the dominant $^{1}O_2$* sink in our laboratory PM extracts, water, is consistent across all extracts (Kaur et al., 2019; Ma et al., 2023). The lack of correlation between $^{1}O_2$* and DOC indicates significant variability in singlet oxygen quantum yields, as discussed below.

3.2.4 Photooxidant quantum yields determined in PM extracts

Using the photooxidant measurements, we calculated the quantum yields (Φ) of $^{\bullet}$OH, ^{3}C*, and $^{1}O_2$* in our samples (Fig. 6). The average ($\pm 1\sigma$) $\Phi_{\bullet OH}$ was 0.037($\pm$0.018) %, similar to previously reported values in aqueous extracts of ambient $PM_{2.5}$ (Fig. 6a) (Kaur et al., 2019; Ma et al., 2024). We find that $\Phi_{\bullet OH}$ is independent of the sampling site

but does depend on pH: the lower quantum yields at pH 5 (compared to pH 1) are likely due to the lower solubility of transition metals, which can be sources of •OH (Sunday et al., 2025). Φ_{3C*} was relatively stable with an average of 3.0(±1.2) %, nearly identical to the average for Davis particles (Ma et al., 2024), although our quantum yield range (1.2 %–4.9 %) is notably narrower than in this past work (0.9 %–8.8 %). Φ_{3C*} demonstrates no site or pH dependence, which is likely because our MAC values and DOC concentrations show little variation with sample site or extract pH (Fig. S4). In contrast to Φ_{3C*}, the Φ_{1O2*} of 1.8 %–8.5 % observed in our 6-week field campaign demonstrates a range of values similar to those reported in samples collected over a 1-year period in Davis, California (Ma et al., 2024). We find minor site and pH differences in Φ_{1O2*}, but without further investigation, we cannot comment on the causes. We find a significant correlation between Φ_{1O2*} and E2/E3 ($R^2 = 0.63$, p value < 0.01; Fig. S7), even with our narrow range of E2/E3 values, which suggests that higher-molecular-weight DOC (which has lower E2/E3 ratios) corresponds to lower Φ_{1O2*}. This also suggests that small changes in the average molecular weight of BrC compounds can significantly impact their ability to produce $^1O_2$* (Ossola et al., 2021). Altogether, we attribute the wide range of Φ_{1O2*} values to minor differences in BrC sources or small changes in the degree of chemical aging due to reactions that might involve direct photodegradation, •OH, ^{3}C*, or ozone (Bogler et al., 2022; Leresche et al., 2021; Ma et al., 2024).

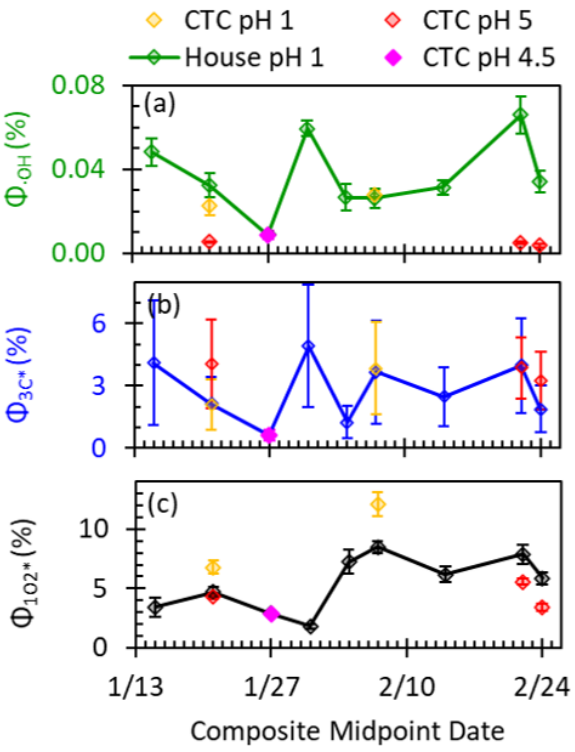

Figure 6. Quantum yields measured in dilute particle extracts under simulated sunlight laboratory conditions for **(a)** •OH, **(b)** ^{3}C*, and **(c)** $^1O_2$*.

3.3 Modeling photooxidant production in aerosol liquid water

Next, we use kinetic models to predict the steady-state concentrations of •OH, ^{3}C*, and $^1O_2$* in aerosol liquid water under Fairbanks actinic flux conditions using the quantum yields determined in our extracts (Fig. 7). First, we used our dilution series to understand how photooxidant production changes with DOC concentration (Table S13, Fig. S8). In our PM extracts, where DOC concentrations are similar to cloud/fog water conditions, $P_{\bullet OH,EXP,PME}$, $P_{3C*,EXP,PME}$, and $P_{^1O_2*,EXP,PME}$ are all proportional to DOC concentration, which agrees with previous work on PM extracts from Davis, California (Kaur et al., 2019; Ma et al., 2023). To extrapolate our photooxidant concentrations to aerosol liquid water conditions, we used parameters defined by Ma et al. (2023) (Table S14) to predict how photooxidant production rates and sinks vary as a function of ALWC (Sect. 2.6.3), using DOC concentration as our proxy for ALW. As shown in Fig. 7, concentrations of $^1O_2$* and ^{3}C* are predicted to be higher in ALW compared to in PM extracts (which are roughly as concentrated as fog/cloud drops), while •OH is fairly stable across the entire range of DOC concentration. Figure 8 shows the modeled photooxidant concentrations under Fairbanks actinic flux in both ALW (colored points, Table S15) and in our much more dilute PM extracts (grey points).

3.3.1 Hydroxyl radical in ALW

Even in the winter in Fairbanks, we predict significant concentrations of •OH, ^{3}C*, and $^1O_2$* in particles. Midday •OH concentrations predicted for Fairbanks ALW at pH 1 range from (1–6) $\times 10^{-15}$ M (Fig. 8a), similar to •OH concentrations in ALW reported by Ma et al. (2023) in $PM_{2.5}$ from Davis, California, at midday on the winter solstice ((6–9) $\times 10^{-15}$ M). The lower •OH observed in Fairbanks is in part because of lower wintertime actinic fluxes compared to those in California and in part because the Davis sunlight condition is solar noon, while the Fairbanks sunlight condition is the average peak 3 h of daylight. In ALW, we calculated the potential role of two additional potential sources of •OH that would not be captured in our illumination experiments: the reactions of ozone with superoxide (Bielski et al., 1985) and ozone with phenolic moieties in DOC (Önnby et al., 2018), but each accounted for less than 1 % of the measured •OH production. Of the three photooxidants discussed here, •OH is the only oxidant whose steady-state concentration does not show major differences between dilute extract conditions and concentrated aerosol liquid water conditions (Fig. 8a). This is because both the production rate of

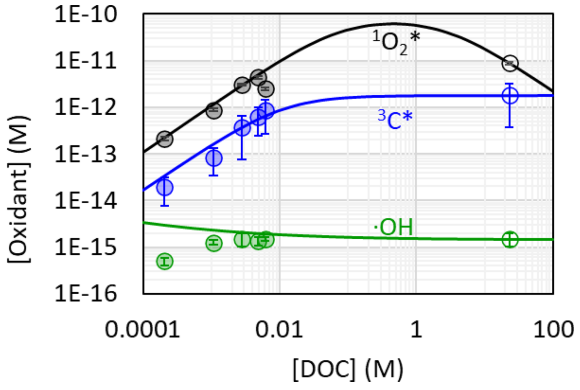

Figure 7. Kinetic models used to extrapolate photooxidant concentrations from the dilution series in PM extracts to aerosol liquid water conditions for CTC sample 2/14 for singlet oxygen (gray circles), oxidizing triplets (blue circles), and hydroxyl radical (green circles). The filled circles at low DOC concentrations represent the dilution series measurements, and the open circles at high DOC correspond to extrapolated values for ALW conditions with a PM mass/H_2O mass ratio of 0.69 µg PM/µg H_2O determined for the 2/14 CTC sample. Oxidant concentrations in the dilution series and ALW extrapolation were normalized to $j_{2NB,AK} = 0.0045\ s^{-1}$, which corresponds to the average midday actinic flux for 1 February and includes the 2.5 enhancement factor due to optical confinement. Lines represent extrapolations, which were made using Eqs. (4), (5), and (6) with parameters from Tables S14, S15, and S16. The line for •OH includes mass transport of •OH from the gas phase, which is why the green line is above the PM extract data points, which represent only aqueous sources.

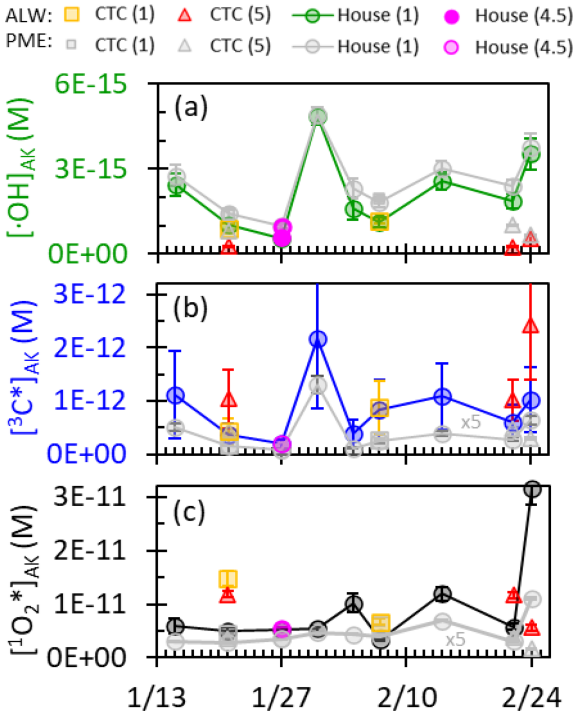

Figure 8. Predicted steady-state concentrations of **(a)** •OH, **(b)** ^{3}C*, and **(c)** $^1O_2$* under Fairbanks $I_{\lambda,AK}$ averaged over the peak 3 h of sunlight for each composite period. The colored points represent concentrated ALW conditions (average [DOC] = 21(±7) M). The grey data represent results for the PM extracts (average [DOC] = 2.6(±0.8) × 10^{-3} M), i.e., Fig. 5 results with added •OH uptake from mass transport and adjusted to the measured Fairbanks $I_{\lambda,AK}$ for each composite. For **(b)** and **(c)**, the PME ^{3}C* and $^1O_2$* concentrations are multiplied by a factor of 5 so they can be distinguished from the x axis. Note that CTC site samples may slightly underestimate DOC concentration in ALW due to using $PM_{0.7}$ samples, which may lead to a small overestimate of $^1O_2$* at the CTC site. The pH of each sample type is indicated in parentheses in the legend.

•OH and its first-order rate constant for loss increase linearly with DOC concentration (as a proxy for solution concentration), as reported in past work (Kaur et al., 2019; Ma et al., 2023). For example, in our dilution experiment composite (CTC 2/14, pH 1), the predicted $P_{\bullet OH,ALW}$ is roughly 8000 times higher than the measured $P_{\bullet OH,EXP}$ for the standard extract, while $k'_{\bullet OH,ALW}$ is also 8000 times faster than its extract value, corresponding to an •OH lifetime in ALW at pH 1 of 0.2(±0.1) ns (nanoseconds). The minor difference in •OH concentrations between PME and ALW conditions, e.g., in Fig. 7, is caused by mass transport – in dilute conditions with PM mass/H_2O mass ratios equal to our PM extracts, mass transport accounts for 6 %–50 % of the •OH source, while in ALW it only accounts for 0.4 %–5 %, leading to slightly lower •OH concentrations in ALW.

3.3.2 Triplet excited states of brown carbon in ALW

We predict that Fairbanks PM also produces significant concentrations of ^{3}C* during daylight (Fig. 8b), ranging from (0.2–2) × 10^{-12} M, which are at the lower end of the range of ^{3}C* concentrations in ALW reported in California particles during winter, to (0.4–13) × 10^{-12} M (Ma et al., 2023). Because the source of ^{3}C* is BrC, higher DOC concentrations lead to higher ^{3}C* production rates (Fig. S8). The dominant sink for ^{3}C* in dilute conditions is energy transfer with O_2, accounting for 90(±2) % of ^{3}C* loss, with DOC accounting for the remaining 10(±2) % (Table S16), as seen previously (Ma et al., 2023). In ALW conditions, however, DOC concentrations are 10^3–10^4 times higher, and DOC is the dominant (> 99 %) ^{3}C* sink. Because DOC is both the dominant source and the dominant sink of ^{3}C* in ALW, the triplet concentration plateaus at the high DOC concentrations expected in ALW (Fig. 7) (Kaur et al., 2019; Ma et al., 2023). On average, predicted ^{3}C* concentrations in ALW are 12(±4) times higher than in our extracts, similar to the enhancements reported in past work (Kaur et al., 2019; Ma et al., 2023). In ALW, the average predicted lifetime of ^{3}C* is 0.9(±0.6) ns, almost 3 orders of magnitude shorter than in PM extracts (500 ns). It is worth noting that our predicted ^{3}C* lifetimes in ALW are within the range of singlet excited states of BrC

($^1C^*$) lifetimes (0.15–5.5 ns) measured for humic substances in dilute surface waters. This suggests that singlet states of brown carbon might be significant for chemistry in aerosol particles.

3.3.3 Singlet molecular oxygen in ALW

We also predict high concentrations of $^1O_2^*$ in ALW in Fairbanks, ranging from $(4–30) \times 10^{-12}$ M (Fig. 8c). Surprisingly, most of our measurements fall within the range reported by Ma et al. (2023) for Davis PM ($(1–8) \times 10^{-12}$ M), despite notably different wintertime photon fluxes in these two locations. We attribute this similarity to higher $\Delta P_{1O2*}/\Delta DOC$ values in Fairbanks, leading to comparable P_{1O2*} at both latitudes (Table S16). In addition, because the steady-state $^1O_2^*$ concentration in ALW is highly dependent on the DOC concentration, similar ALW DOC concentrations in both locations lead to similar predicted $^1O_2^*$ concentrations. In ALW, DOC is the dominant sink for $^1O_2^*$, accounting for 88(±6) % of its loss, while in our PM extracts, DOC is a minor sink, and water accounts for > 99 % of $^1O_2^*$ loss (Table S14, Ma et al., 2023). While the rate of $^1O_2^*$ loss to DOC increased at higher DOC concentrations, P_{1O2*} reaches a maximum at high DOC concentrations because P_{1O2*} is limited by the maximum $^3C^*$ concentration in high-DOC conditions (Fig. 7). This phenomenon leads to lower $^1O_2^*$ concentrations predicted under higher-DOC conditions and explains why the highest $^1O_2^*$ concentration was observed in the 24 February CTC composite: warmer temperatures caused high ALW, dilute DOC concentration in ALW, and therefore slower $^1O_2^*$ loss to DOC. The high $^1O_2^*$ concentrations predicted here for Fairbanks PM in winter reiterate the impact of DOC on $^1O_2^*$ concentrations in ALW reported by Ma et al. (2023). Overall, the high concentrations of all three photooxidants predicted for ALW suggest these oxidants are important drivers of particle-phase chemistry during winter pollution events in Fairbanks.

4 Atmospheric implications

While measurements of $^\bullet OH$, $^3C^*$, and $^1O_2^*$ in ambient PM extracts indicate a strong potential role of photooxidants in heterogenous chemistry, little work has been done to assess how particle photooxidants compete against other oxidation mechanisms to contribute to $PM_{2.5}$ production and loss (Badali et al., 2015; Bogler et al., 2022; Kaur et al., 2019; Kaur and Anastasio, 2018; Leresche et al., 2021; Ma et al., 2023, 2024; Smith et al., 2014, 2015, 2016; Yu et al., 2016). Here, we first explore the lifetime of various organic species due to photooxidative loss. Next, we model secondary SO_4^{2-} formation in Fairbanks during winter pollution events, and, finally, we assess the potential of BrC-mediated photochemistry year-round in Fairbanks.

4.1 Effect of photooxidants on the lifetimes of organic compounds

Triplets and $^1O_2^*$ are highly reactive with certain classes of organic compounds, while $^\bullet OH$ is highly reactive with nearly all classes. Using the average particle photooxidant concentrations during the peak 3 h of daylight during ALPACA, we estimated the average daylight winter lifetime of several organic species (Table S17). Substituted phenols, which react rapidly with $^3C^*$ and $^\bullet OH$ (Arciva et al., 2022; Ma et al., 2021), have lifetimes in Fairbanks between 3 and 6 min due to $^3C^*$ and 9–19 h lifetimes due to aqueous $^\bullet OH$. $^1O_2^*$ also reacts appreciably with certain organic classes, such as phenols and heterocycles, leading to lifetimes of 0.4–12 h with respect to $^1O_2^*$, which is 2 %–74 % of the lifetime due to $^\bullet OH$ for the same compounds (Manfrin et al., 2019). The lifetimes for these organic species are shorter with respect to triplets and singlet oxygen, primarily because ALW concentrations of these oxidants are much higher compared to $^\bullet OH$: the average $[^3C^*]:[^\bullet OH]$ and $[^1O_2^*]:[^\bullet OH]$ ratios for our samples are 390 and 4200, respectively. The short lifetimes of organic compounds demonstrate that biomass burning particles are active sites of oxidation driven by BrC photochemistry, even in winter in Fairbanks, Alaska.

4.2 Secondary sulfate formation

In Fairbanks, traditional gas-phase S(IV) oxidants, such as O_3, HOOH, and $^\bullet OH$, are expected to be minor sulfate sources in Fairbanks winter because of limited sunlight (Moon et al., 2024; Simpson et al., 2019). Instead, several nontraditional oxidants may be important for secondary SO_4^{2-} formation in aerosols under highly polluted conditions, including oxidation by $^3C^*$, photochemical HOOH produced inside BrC particles, HONO, and NO_2 (Anastasio et al., 1997; Sunday et al., 2025; Wang et al., 2020a, b). To assess the contribution of $^3C^*$ to secondary sulfate during ALPACA, we built a kinetic model that calculates the rates of secondary SO_4^{2-} formation through eight oxidation pathways (one gas phase and seven particle phases) during the peak 3 h of daylight.

The kinetics for each oxidant with inorganic S(IV) (Table S18), the concentrations and activity coefficients of the oxidants (Table S19), and the activity of inorganic S(IV) (Table S20, Sect. S7) are summarized in the supplementary information. Kinetics are from the literature (Cheng et al., 2016; Ibusuki and Takeuchi, 1986; Martin and Hill, 1987; Mu et al., 2021; Seinfeld and Pandis, 2016; Song et al., 2021; Tilgner et al., 2021; Wang et al., 2020a, 2021, 2020b; Ye et al., 2021; Yu et al., 2023), while the concentrations of several key oxidants were measured and modeled during the ALPACA field campaign (Cesler-Maloney et al., 2022; Simpson et al., 2023; Kuhn et al., 2024; Simpson et al., 2024; Sunday et al., 2025). While the rate constants and oxidant concentra-

tions have constrained errors, the concentration of inorganic S(IV) is highly uncertain.

4.2.1 Predicting inorganic S(IV)

The measured concentrations of inorganic S(IV) in ALPACA particles are orders of magnitude higher than expected based on Henry's law (Fig. S10). Mao et al. (2024) report that up to 30 % of the total particulate sulfur content was S(IV), including hydroxymethanesulfonate, other organo-S(IV) adducts, and inorganic S(IV). The measurements of inorganic S(IV) were determined in parallel extracts of the same filter with and without added HOOH to remove inorganic S(IV), but the HOOH probably also destroyed labile organo-S(IV) compounds, resulting in them also being counted as inorganic S(IV) (Campbell et al., 2022; Dingilian et al., 2024b). To better constrain inorganic S(IV), we used the model to find the activity of inorganic S(IV) where the fraction of secondary SO_4^{2-} formed by HOOH in our model matched the value reported from sulfate isotope measurements by Moon et al. (2024) (Sect. S7). Based on this process, our modeled inorganic S(IV) activity for pH 1 particle water is, on average ($\pm 1\sigma$), 29($\pm$40) times lower than the "measured" inorganic S(IV) and 1.5($\pm$3.0) $\times 10^6$ times higher than that predicted by Henry's law (Fig. S10). The HOOH fraction is fixed to match the isotope results, making the fractional contribution of HOOH well constrained. In contrast, the contributions from other sources are calculated only from our kinetic modeling, leaving the error in the rest of the model difficult to quantify. Nonetheless, the results provide novel insight into the contribution of competing secondary sulfate pathways, including from ^{3}C*.

4.2.2 31 January polluted period

During the 31 January polluted period, the model calculates a cumulative secondary SO_4^{2-} formation rate of 0.9 µg m^{-3} h^{-1} at pH 1 during the peak 3 h of daylight. Within the 1.5–3 h estimated lifetime of a particle in the boundary layer during pollution episodes (Cesler-Maloney et al., 2024), this yields 1–3 µg m^{-3} of secondary SO_4^{2-}, similar to the isotope-determined measurements of 1.5 µg m^{-3} for the daytime sample collected on 31 January (Moon et al., 2024). During the pollution episode, HOOH accounts for 54 % of secondary sulfate, while NO_2, gaseous $^\bullet$OH, ^{3}C*, and O_3 each contribute between 8 % and 14 %, accounting for much of the remaining portion (Table S21). Surprisingly, local photochemistry dominates the production of secondary sulfate during ALPACA: of the modeled daytime secondary sulfate, 76 % is photochemically formed by the sum of HOOH produced inside particles, gas and aqueous $^\bullet$OH, and particulate ^{3}C*. The sulfate isotope field measurements support the hypothesis of significant photochemical secondary SO_4^{2-}: during daylight hours on 31 January, secondary SO_4^{2-} accounted for 35 % of total SO_4^{2-}, while at night, the fraction of secondary SO_4^{2-} decreased to 16 % (Moon et al., 2024). Our model highlights the important, and unexpected, role of photochemistry in sulfate formation during winter pollution events in Fairbanks.

As a direct oxidant, triplets play a minor role in sulfur chemistry. The model predicts that during the 31 January pollution episode, 10 % of secondary sulfate is from ^{3}C* during the peak 3 h of daylight, while the 24 h average isotopic measurements attribute 3 % of secondary sulfate to the ^{3}C*/TMI pathways (sulfate from ^{3}C* and TMI are isotopically equivalent and cannot be distinguished by measurements; Sect. S8) (Moon et al., 2024). The difference between the measured and modeled ^{3}C* contribution is likely because they represent different time periods: the contribution of ^{3}C* is the strongest during peak daylight and stops at sunset, leading to low 8 h average isotopic signatures of sulfate from ^{3}C*/TMI. During peak daylight hours, we calculate 0.1 µg m^{-3} h^{-1} of sulfate from ^{3}C*, which is 800 times slower than the 7.9 µg m^{-3} h^{-1} upper bound predicted in past work (Wang et al., 2020b). The discrepancy stems from differences in predicted ^{3}C* concentrations in ALW. Wang et al. (2020b) calculated triplet-mediated rates of sulfate formation using ^{3}C* concentrations as high as 1×10^{-10} M, while recent work shows that ^{3}C* concentrations in particles are closer to the 10^{-12} M value shown in Fig. 7 (Kaur et al., 2019; Ma et al., 2023; Wang et al., 2020b). Recently, Liang et al. (2024) reported enhanced surface activity of triplets in illuminated biomass burning organic aerosol (BBOA) microdroplets, leading to rapid interfacial sulfate formation, not accounted for in our model. In Fairbanks, HOOH formed from triplet-mediated reactions is more significant as an oxidant of S(IV) than triplets themselves (Moon et al., 2024; Sunday et al., 2025).

4.2.3 7 February clean period

During the 7 February clean period, the model predicts that ^{3}C* contributes less than 1 % to sulfate formation. Overall, our model has moderate agreement with the isotope measurements for this period (Fig. 9f, Table S21) (Moon et al., 2024). Because the activity of inorganic S(IV) was defined by matching the modeled and measured fraction of secondary SO_4^2 formed by HOOH (see Sect. S7), both techniques agree that HOOH is the dominant formation pathway, accounting for 44 % of secondary SO_4^{2-}. The model and measurements also agree that O_3 and gas-phase $^\bullet$OH are the second- and third-most important mechanisms, respectively. The biggest discrepancies between the model and measurements are for the ^{3}C*/TMI and NO_2 pathways: in the model these pathways each account for 1 % of secondary SO_4^{2-} formation, while measurements indicate ^{3}C*/TMI and NO_2 account for 10 % and 9 %, respectively. The discrepancies between the model and measurements are likely because our model uses surface measurements and therefore only represents ground-level chemistry. The well-mixed boundary layer, which is

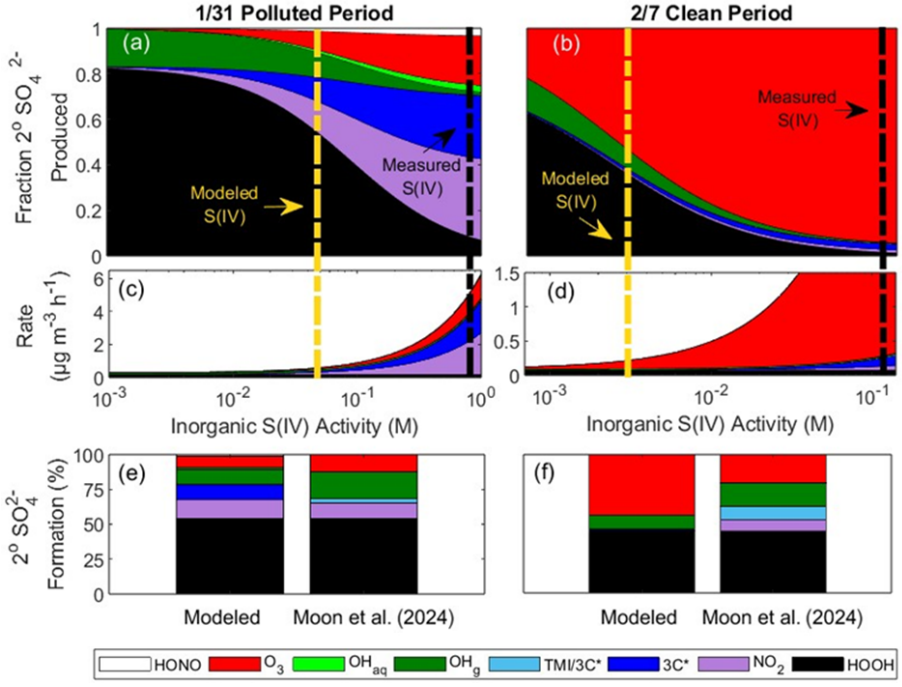

Figure 9. Modeled secondary (2°) SO_4^{2-} formation under low-pH (pH 1) daytime conditions during the 31 January polluted period and 7 February clean period due to HOOH, NO_2, $^3C^*$, and O_2 catalyzed by transition metal ions (TMIs), gas-phase $^\bullet OH$, aqueous-phase $^\bullet OH$, and O_3. Panels **(a)** and **(b)** show the fraction of secondary SO_4^{2-} formation from each oxidation pathway as a function of particle inorganic S(IV) activity. The vertical dashed black lines are the ALW inorganic S(IV) activities based on PM measurements (likely an overestimate because of contributions from organo-S(IV) compounds). The vertical dashed yellow lines are the predicted ALW inorganic S(IV) activities. Panels **(c)** and **(d)** show the total rate of secondary SO_4^{2-} formation from all pathways as a function of inorganic S(IV) activity. Panels **(e)** and **(f)** show the contribution of each oxidant to secondary SO_4^{2-} formation at the modeled activities of inorganic S(IV). Parallel results for high-pH (pH 4–5) conditions are presented in Fig. S9.

characteristic of clean periods in Fairbanks, likely transports sulfate formed aloft to the surface, which is captured in the isotopic measurements of sulfate but not by our model.

4.3 Predicted seasonal variations in BrC-mediated photochemistry

Brown-carbon-mediated photochemistry in Fairbanks is not limited to winter pollution events but could contribute to multiphase chemistry throughout the year. To investigate this, Fig. 10 compares the monthly average photochemical activities of particulate BrC, gas-phase O_3, and gas-phase HONO using actinic fluxes modeled with TUV (parameters in Table S22, Finlayson-Pitts and Pitts, 2000; Seinfeld and Pandis, 2016).

Figure 10a depicts the first-order photolysis rate constants (j values) for each reaction normalized to their June value (Sect. S9, Table S23). The photochemical production of $^\bullet OH$ from O_3 shows a strong seasonable dependence in Fairbanks, with the January photolysis frequency being only 0.2 % of the June value. In contrast, brown carbon and HONO experience less seasonal dependence, with January j values at 13 % and 14 % of the June values, respectively. O_3 is more impacted by seasonal changes in the actinic flux because it absorbs shorter wavelengths of light than BrC and HONO, and short wavelengths are the most suppressed during winter (Seinfeld and Pandis, 2016). Figure 10a also demonstrates the impact of albedo: long-lasting snow cover leads to peak HONO and BrC j values in March and April, indicating the strong potential for BrC photochemistry during this period.

Seasonal variations in the concentrations of BrC, HONO, and O_3 (Fig. 10b) also affect their rates of photoactivity (Sect. S10). The peak in woodsmoke OA and HONO concentrations during winter months enhances their dominance in winter photochemistry. In the summer, BrC photochemistry is also expected to be important because of high, yet highly variable, BrC concentrations from wildfires. HONO concentrations in Fairbanks are expected to be relatively low in summer, both because higher summertime HONO j values lead to enhanced photochemical loss and because of enhanced summer vertical mixing.

Figure 10c integrates the results from panels (a) and (b) to compare the production of $^3C^*$ from BrC to the production of $^\bullet OH$ by HONO and O_3; it clearly demonstrates that BrC-mediated photochemistry is likely important year-

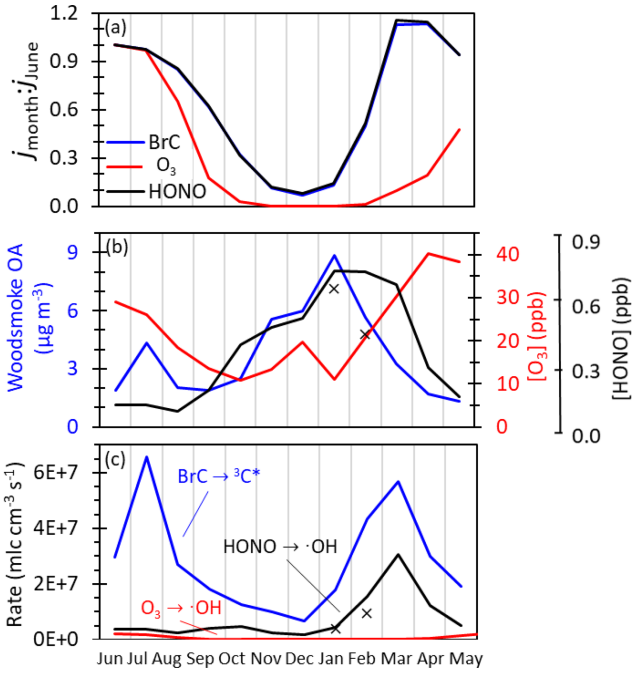

Figure 10. Predicted seasonal variations in three photochemical reactions in Fairbanks, Alaska: oxidizing triplet formation from particulate brown carbon (BrC→^{3}C*), •OH formation from gas-phase ozone (O_3→•OH), and •OH formation from gas-phase nitrous acid (HONO→•OH) (Sect. S9). **(a)** Photolysis rate constant (j) for each reaction at solar noon on the 15th day of each month normalized to the corresponding mid-June j value. **(b)** Measured and estimated monthly BBOA, O_3, and HONO concentrations (Sect. S10). The black line is the estimated monthly HONO, and the black × symbols are monthly averaged HONO measured during ALPACA within the polluted layer (Kuhn et al., 2024). **(c)** Predicted midday rates of each reaction on the 15th of each month. The rate of triplet formation in particles from brown carbon is expressed in equivalent gas-phase units.

round. The ^{3}C* production rate has two peaks: the first in late winter/early spring, when surface-based inversions trap copious BrC-rich woodsmoke, and the second during summer, when wildfires produce abundant BrC (Kotchenruther, 2016; Robinson et al., 2024). In the cold months, triplet production in particles is on average 3.4(±0.6) times faster than gas-phase •OH production by HONO and up to 10 000 times faster than the negligible •OH production by O_3 photolysis. Triplet production is also predicted to be rapid in the summer when wildfire smoke influences air quality. Based on the estimated ^{3}C* formation rates during the summer of 2021, a period only moderately impacted by wildfire smoke (Fig. 10c), summertime ^{3}C* formation is much faster than •OH production: 11(±5) times faster than •OH production by HONO and 20(±10) times faster than •OH production by O_3. While oxidizing triplets are more selective than •OH, they react rapidly with multiple classes of organic compounds, including phenols (Table S17a, Arciva et al., 2022; Ma et al., 2021; Smith et al., 2014, 2015, 2016), and they are a source of HOOH (Anastasio et al., 1997; Sunday et al., 2025). Overall, Fig. 10 indicates that ^{3}C*-mediated photochemistry is likely important for particle-phase chemistry year-round in Fairbanks.

5 Conclusions and uncertainties

In this work, we characterized the production of •OH, ^{3}C*, and $^1O_2$* in aqueous particulate matter extracts collected during the winter 2022 ALPACA field campaign in Fairbanks, Alaska. We then used kinetic models to extrapolate oxidant concentrations from our dilute extracts to the concentrated conditions of aerosol liquid water. We predict significant concentrations of all three photooxidants in Fairbanks PM, at levels that are comparable to those in wintertime particles in northern California. Next, we modeled secondary sulfate formation and find that photochemistry is the dominant source of secondary sulfate during daylight hours, primarily from in-particle hydrogen peroxide, while oxidation by ^{3}C* and aqueous •OH are minor. Lastly, we estimated rates of ^{3}C* production year-round from brown carbon in Fairbanks PM: ^{3}C* is formed at significant rates throughout the year, with peaks during late winter pollution events and seasonal summer wildfires. Overall, this work provides insight into the unexpected role of photooxidative multiphase chemical processing of PM during winter pollution events in Fairbanks, Alaska, and throughout the subarctic.

As our PM filter extracts are prepared in water, our work does not account for water-insoluble BrC. Atwi et al. (2022) report that water-insoluble chromophores account for the majority of BrC light absorbance, indicating a potential missing reservoir of water-insoluble BrC capable of forming particle photooxidants. As of yet, the photochemistry driven by water-insoluble BrC has not been explored.

A significant source of uncertainty in our results is the effect of low winter temperatures on multiphase photochemistry. While we performed our experiments at 10 °C, midday temperatures in Fairbanks ranged from −33.9 to 5.2 °C during the ALPACA campaign. Temperature can impact numerous processes, including gas–particle partitioning and the rates of chemical reactions. Where thermodynamic data are available, we corrected the Henry's law constants and reaction rate constants to Fairbanks winter temperatures (Sander, 2023; Smith et al., 2014, Table S18). However, many processes do not have a well-constrained temperature dependence, including many of the quantum yields, rate constants, and absorption coefficients that we measured or used in this study. Similarly, only one of the eight sulfate formation reactions in the secondary sulfate model has a published temperature dependence. Nonetheless, our work incorporates the available temperature dependence data to provide insight into multiphase photochemistry at a high-latitude winter site.

Another important impact of low temperature is the phase state of particles (Kiland et al., 2023; Reid et al., 2018; Shi-

raiwa et al., 2017; Zobrist et al., 2008). A large body of work has demonstrated a freezing point suppression in aerosol particles. For example, Cziczo and Abbatt (1999) reported that pure water aerosols freeze only at −39 °C, while supercooled ammonium sulfate (49 % by weight) particles freeze at −49 °C, with higher salt concentrations leading to a larger freezing point suppression. Hearn and Smith (2005) observed rapid chemistry occurring in the organic condensed phase as low as −32 °C, while at lower temperatures the aerosol particles crystallized and chemistry stopped. We expect that particles in Fairbanks during winter are not solids but supercooled liquids, and they are likely viscous (Kiland et al., 2023; Koop et al., 2011). We expect photooxidants produced in situ will not be hindered by high viscosities: BrC is expected to continue to absorb light in viscous particles, suggesting $^3C^*$ and $^1O_2^*$ production continues in viscous conditions. We do, however, expect that the higher viscosities predicted for Fairbanks particles likely affect secondary sulfate formation because gas-phase species like SO_2 and O_3, which diffuse into the aqueous phase, will be limited by slow mass transport in viscous media (Koop et al., 2011). More research is needed to constrain the impact of particle phase state on multiphase photochemistry.

The last major source of uncertainty is related to the kinetic model used to extrapolate photooxidant concentrations from bulk PM extracts to aerosol liquid water conditions. Our bulk PM extracts are roughly the concentration of cloud/fog waters, which are 3 to 4 orders of magnitude more dilute than aerosol liquid waters. The dilution experiment (Fig. S8) constrains the relationships between photooxidant production and dissolved organic carbon content, but direct measurements of oxidant concentrations have not been made in suspended particles to confirm the extrapolation to ALW. Specific to $^1O_2^*$ in ALW, the second-order rate constant for DOC with $^1O_2^*$ – a key parameter to determine $^1O_2^*$ concentrations in particles – is not well constrained (Ma et al., 2023). Measurements of photooxidant concentrations in suspended particles and the rate constant for $^1O_2^*$ with DOC are needed to fully understand multiphase photooxidant production in PM.

Data availability. Experimental data are available upon request. Temperature, O_3, and NO_x measurements can be found at https://doi.org/10.18739/A27D2Q87W (Simpson et al., 2023). ALW and pH can be found at https://doi.org/10.18739/A2G73757K (Campbell et al., 2024a). Sulfate source apportionment measurements can be found at https://doi.org/10.18739/A2Q52FF68 (Moon et al., 2023). HMS measurements can be found at https://doi.org/10.18739/A2VD6P65Q (Dingilian et al., 2024a).

Supplement. The supplement related to this article is available online at https://doi.org/10.5194/acp-25-9561-2025-supplement.

Author contributions. CA, LH, WS, MS, BA, JD, JM, JHF, and JS developed the research goals and designed the experiment. AM, SK, TF, KE, MS, and BA set up the samplers in Fairbanks and collected filter samples. FG and JHF made actinic flux measurements in Fairbanks. MCM and WS made measurements of temperature, O_3, NO_2, and SO_2; JS made HONO measurements using a long-path DOAS; and JD measured particle composition at the CTC site. JC and JM modeled ALW and pH in aerosol in Fairbanks using ISORRPIA-II. LH and JH performed the photochemistry experiments. MOS and AB analyzed ions and DOC, respectively. LH analyzed the data, built the models, and prepared the paper with CA. The other authors provided helpful feedback on the paper.

Competing interests. At least one of the (co-)authors is a member of the editorial board of *Atmospheric Chemistry and Physics*. The peer-review process was guided by an independent editor, and the authors also have no other competing interests to declare.

Disclaimer. Publisher's note: Copernicus Publications remains neutral with regard to jurisdictional claims made in the text, published maps, institutional affiliations, or any other geographical representation in this paper. While Copernicus Publications makes every effort to include appropriate place names, the final responsibility lies with the authors.

Acknowledgements. We gratefully acknowledge the following agencies for their publicly available data: the entire ALPACA team for data collection and collaboration; NOAA's Environmental Research Division Data Access Program (ERDDAP) website for relative humidity data (https://erddap.sensors.ioos.us/erddap/tabledap/alaska-dot-rwis-255.html, last access: 18 October 2023, Airport Way @ Eielson Street); the Alaska Department of Environmental Conservation for year-round $PM_{2.5}$, O_3, and NO_2 data; the NCAR Tropospheric Ultraviolet and Visible (TUV) radiation model website for actinic flux and photolysis rate constants (https://www.acom.ucar.edu/Models/TUV/Interactive_TUV/, last access: 1 April 2022); the UC Davis Interdisciplinary Center for Plasma Mass Spectrometry (ICP-MS) for metal analysis; and Kerri Steenwerth and Kyle T. Sherbine (USDA) for ion analysis. We also thank Frank Leresche, Nadine Borduas-Dedekind, Keighan Gemmell, Claudia Sardena, and the anonymous reviewer for their comments and insights.

Financial support. This research has been supported by the National Science Foundation (grant nos. 2109011 (UC Davis), 2109023 (UNH), 2109098 (UH), AGS-1654104 and CHE-2203419 (UC Irvine), AGS-2029747 and ICER-1927750 (UAK)); the National Oceanic and Atmospheric Administration (grant no. NA20OAR4310295 to UW); and the University of California, Davis (Donald G. Crosby Graduate Fellowship in Environmental Chemistry and Jastro Shields Research Awards to Laura M. D. Heinlein).

Review statement. This paper was edited by Alexander Laskin and reviewed by Frank Leresche, Nadine Borduas-Dedekind, and one anonymous referee.

References

Anastasio, C. and McGregor, K. G.: Chemistry of fog waters in California's Central Valley: 1. In situ photoformation of hydroxyl radical and singlet molecular oxygen, Atmos. Environ., 35, 1079–1089, https://doi.org/10.1016/S1352-2310(00)00281-8, 2001.

Anastasio, C., Faust, B. C., and Rao, C. J.: Aromatic Carbonyl Compounds as Aqueous-Phase Photochemical Sources of Hydrogen Peroxide in Acidic Sulfate Aerosols, Fogs, and Clouds. 1. Non-Phenolic Methoxybenzaldehydes and Methoxyacetophenones with Reductants (Phenols), Environ. Sci. Technol., 31, 218–232, https://doi.org/10.1021/es960359g, 1997.

Appiani, E. and McNeill, K.: Photochemical production of singlet oxygen from particulate organic matter, Environ. Sci. Technol., 49, 3514–3522, https://doi.org/10.1021/es505712e, 2015.

Appiani, E., Ossola, R., Latch, D. E., Erickson, P. R., and McNeill, K.: Aqueous singlet oxygen reaction kinetics of furfuryl alcohol: Effect of temperature, pH, and salt content, Environ. Sci. Process. Impacts, 19, 507–516, https://doi.org/10.1039/c6em00646a, 2017.

Arakaki, T., Anastasio, C., Kuroki, Y., Nakajima, H., Okada, K., Kotani, Y., Handa, D., Azechi, S., Kimura, T., Tsuhako, A., and Miyagi, Y.: A General Scavenging Rate Constant for Reaction of Hydroxyl Radical with Organic Carbon in Atmospheric Waters, Environ. Sci. Technol., 47, 8196–8203, https://doi.org/10.1021/es401927b, 2013.

Arciva, S., Niedek, C., Mavis, C., Yoon, M., Sanchez, M. E., Zhang, Q., and Anastasio, C.: Aqueous •OH Oxidation of Highly Substituted Phenols as a Source of Secondary Organic Aerosol, Environ. Sci. Technol., 56, 9959–9967, https://doi.org/10.1021/acs.est.2c02225, 2022.

Arnold, S. R., Law, K. S., Brock, C. A., Thomas, J. L., Starkweather, S. M., Von Salzen, K., Stohl, A., Sharma, S., Lund, M. T., Flanner, M. G., Petäjä, T., Tanimoto, H., Gamble, J., Dibb, J. E., Melamed, M., Johnson, N., Fidel, M., Tynkkynen, V. P., Baklanov, A., Eckhardt, S., Monks, S. A., Browse, J., and Bozem, H.: Arctic air pollution: Challenges and opportunities for the next decade, Elementa, 4, 000104, https://doi.org/10.12952/journal.elementa.000104, 2016.

Atwi, K., Cheng, Z., El Hajj, O., Perrie, C., and Saleh, R.: A dominant contribution to light absorption by methanol-insoluble brown carbon produced in the combustion of biomass fuels typically consumed in wildland fires in the United States, Environ. Sci.-Atmospheres, 2, 182–191, https://doi.org/10.1039/d1ea00065a, 2022.

Badali, K. M., Zhou, S., Aljawhary, D., Antiñolo, M., Chen, W. J., Lok, A., Mungall, E., Wong, J. P. S., Zhao, R., and Abbatt, J. P. D.: Formation of hydroxyl radicals from photolysis of secondary organic aerosol material, Atmos. Chem. Phys., 15, 7831—-7840, https://doi.org/10.5194/acp-15-7831-2015, 2015.

Bali, K., Banerji, S., Campbell, J. R., Bhakta, A. V., Chen, L. W. A., Holmes, C. D., and Mao, J.: Measurements of brown carbon and its optical properties from boreal forest fires in Alaska summer, Atmos. Environ., 324, 120436, https://doi.org/10.1016/j.atmosenv.2024.120436, 2024.

Bielski, B. H., Babelli, D. E., Arudi, R. L., and Ross, A. B.: Reactivity of HO_2/O_2^- in Aqueous Solution, J. Phys. Chem. Ref. Data., 14, 1041–1100, https://doi.org/10.1063/1.555739, 1985.

Bodesheim, M., Schlitz, M., and Schmidt, R.: Triplet state energy dependence of the competitive formation of $O_2(^1\sum_g^+)$, $O_2(^1\Delta_g)$ and $O_2(^3\sum_g^-)$ in the sensitization of O_2 by triplet states, Chem. Phys. Lett., 221, 7–14, https://doi.org/10.1016/0009-2614(94)87008-x, 1994.

Bogler, S., Daellenbach, K. R., Bell, D. M., Prévôt, A. S. H., El Haddad, I., and Borduas-Dedekind, N.: Singlet Oxygen Seasonality in Aqueous PM_{10} is Driven by Biomass Burning and Anthropogenic Secondary Organic Aerosol, Environ. Sci. Technol., 56, 15389–15397, https://doi.org/10.1021/acs.est.2c04554, 2022.

Brett, N., Law, K. S., Arnold, S. R., Fochesatto, J. G., Raut, J.-C., Onishi, T., Gilliam, R., Fahey, K., Huff, D., Pouliot, G., Barret, B., Dieudonné, E., Pohorsky, R., Schmale, J., Baccarini, A., Bekki, S., Pappaccogli, G., Scoto, F., Decesari, S., Donateo, A., Cesler-Maloney, M., Simpson, W., Medina, P., D'Anna, B., Temime-Roussel, B., Savarino, J., Albertin, S., Mao, J., Alexander, B., Moon, A., DeCarlo, P. F., Selimovic, V., Yokelson, R., and Robinson, E. S.: Investigating processes influencing simulation of local Arctic wintertime anthropogenic pollution in Fairbanks, Alaska, during ALPACA-2022, Atmos. Chem. Phys., 25, 1063–1104, https://doi.org/10.5194/acp-25-1063-2025, 2025.

Campbell, J. R., Battaglia, M., Dingilian, K., Cesler-Maloney, M., St Clair, J. M., Hanisco, T. F., Robinson, E., Decarlo, P., Simpson, W., Nenes, A., Weber, R. J., and Mao, J.: Source and Chemistry of Hydroxymethanesulfonate (HMS) in Fairbanks, Alaska, Environ. Sci. Technol., 56, 7657–7667, https://doi.org/10.1021/acs.est.2c00410, 2022.

Campbell, J., Battaglia Jr., M., Dingilian, K., Cesler-Maloney, M., Simpson, W., Robinson, E., DeCarlo, P., Temime-Roussel, B., D'Anna, B., Holen, A., Wu, J., Pratt, K., Dibb, J., Nenes, A., Weber, R., and Mao, J.: Enhanced aqueous formation and neutralization of fine atmospheric particles driven by extreme cold, Fairbanks, Alaska, 2022, Arctic Data Center [data set], https://doi.org/10.18739/A2G73757K, 2024a.

Campbell, J. R., Battaglia Jr., M., Dingilian, K. K., Cesler-Maloney, M., Simpson, W. R., Robinson, E. S., DeCarlo, P. F., Temime-Roussel, B., Holen, A. L., Wu, J., Pratt, K. A., Dibb, J. E., Nenes, A., Weber, R. J., and Mao, J.: Enhanced aqueous formation and neutralization of fine atmospheric particles driven by extreme cold, Sci. Adv., 10, 4373, https://doi.org/10.1126/sciadv.ado4373, 2024b.

Cesler-Maloney, M., Simpson, W. R., Miles, T., Mao, J., Law, K. S., and Roberts, T. J.: Differences in Ozone and Particulate Matter Between Ground Level and 20 m Aloft are Frequent During Wintertime Surface-Based Temperature Inversions in Fairbanks, Alaska, J. Geophys. Res.-Atmos., 127, 036215, https://doi.org/10.1029/2021JD036215, 2022.

Cesler-Maloney, M., Simpson, W., Kuhn, J., Stutz, J., Thomas, J., Roberts, T., Huff, D., and Cooperdock, S.: Shallow boundary layer heights controlled by the surface-based temperature inversion strength are responsible for trapping home heating emissions near the ground level in Fairbanks, Alaska, EGUsphere [preprint], https://doi.org/10.5194/egusphere-2023-3082, 2024.

Chen, H., Ge, X., and Ye, Z.: Aqueous-Phase Secondary Organic Aerosol Formation Via Reactions with Organic Triplet Excited States – a Short Review, Current Pollution Reports, 4, 8–12, https://doi.org/10.1007/s40726-018-0079-7, 2018.

Cheng, Y., Zheng, G., Wei, C., Mu, Q., Zheng, B., Wang, Z., Gao, M., Zhang, Q., He, K., Carmichael, G., Pöschl, U., and Su, H.: Reactive nitrogen chemistry in aerosol water as a source of sulfate during haze events in China, Sci. Adv., 2, 1601530, https://doi.org/10.1126/sciadv.1601530, 2016.

Corral Arroyo, P., David, G., Alpert, P. A., Parmentier, E. A., Ammann, M., and Signorell, R.: Amplification of light within aerosol particles accelerates in-particle photochemistry, Science, 376, 293–296, https://doi.org/10.1126/science.abm7915, 2022.

Crawford, J., Shetter, R. E., Lefer, B., Cantrell, C., Junkermann, W., Madronich, S., and Calvert, J.: Cloud impacts on UV spectral actinic flux observed during the International Photolysis Frequency Measurement and Model Intercomparison (IPMMI), J. Geophys. Res.-Atmos., 108, 8545, https://doi.org/10.1029/2002jd002731, 2003.

Cziczo, D. J. and Abbatt, J. P. D.: Deliquescence, efflorescence, and supercooling of ammonium sulfate aerosols at low temperature: Implications for cirrus cloud formation and aerosol phase in the atmosphere, J. Geophys. Res.-Atmos., 104, 13781–13790, https://doi.org/10.1029/1999JD900112, 1999.

Dingilian, K., Hebert, E., Battaglia, M., Campbell, J., Cesler-Maloney, M., Simpson, W., St. Clair, J., Dibb, J., Temime-Roussel, B., D'Anna, B., Moon, A., Alexander, B., Yang, Y., Nenes, A., Mao, J., and Weber, R.: Hydroxymethanesulfonate and Sulfur (IV) in Fairbanks Winter During the Alaskan Layered Pollution and Chemical Analysis (ALPACA) Study, 2022, Arctic Data Center [data set], https://doi.org/10.18739/A2VD6P65Q, 2024a.

Dingilian, K., Hebert, E., Battaglia, M., Campbell, J. R., Cesler-Maloney, M., Simpson, W., St. Clair, J. M., Dibb, J., Temime-Roussel, B., D'Anna, B., Moon, A., Alexander, B., Yang, Y., Nenes, A., Mao, J., and Weber, R. J.: Hydroxymethanesulfonate and Sulfur(IV) in Fairbanks Winter During the ALPACA Study, ACS ES&T Air, 1, 646–659, https://doi.org/10.1021/acsestair.4c00012, 2024b.

Edwards, K. C., Kapur, S., Fang, T., Cesler-Maloney, M., Yang, Y., Holen, A. L., Wu, J., Robinson, E. S., DeCarlo, P. F., Pratt, K. A., Weber, R. J., Simpson, W. R., and Shiraiwa, M.: Residential Wood Burning and Vehicle Emissions as Major Sources of Environmentally Persistent Free Radicals in Fairbanks, Alaska, Environ. Sci. Technol., 58, 14293–14305, https://doi.org/10.1021/acs.est.4c01206, 2024.

Farley, R., Bernays, N., Jaffe, D. A., Ketcherside, D., Hu, L., Zhou, S., Collier, S., and Zhang, Q.: Persistent Influence of Wildfire Emissions in the Western United States and Characteristics of Aged Biomass Burning Organic Aerosols under Clean Air Conditions, Environ. Sci. Technol., 56, 3645–3657, https://doi.org/10.1021/acs.est.1c07301, 2022.

Finlayson-Pitts, B. J. and Pitts Jr., J. N.: Chemistry of the Upper and Lower Atmosphere: Theory, Experiments, and Applications, Academic Press, https://doi.org/10.1016/B978-0-12-257060-5.X5000-X, 2000.

Galbavy, E. S., Ram, K., and Anastasio, C.: 2-Nitrobenzaldehyde as a chemical actinometer for solution and ice photochemistry, J. Photochem. Photobiol. A Chem., 209, 186–192, https://doi.org/10.1016/j.jphotochem.2009.11.013, 2010.

Gerritz, L., Schervish, M., Lakey, P. S. J., Oeij, T., Wei, J., Nizkorodov, S. A., and Shiraiwa, M.: Photoenhanced Radical Formation in Aqueous Mixtures of Levoglucosan and Benzoquinone: Implications to Photochemical Aging of Biomass-Burning Organic Aerosols, J. Phys. Chem. A, 127, 5209–5221, https://doi.org/10.1021/acs.jpca.3c01794, 2023.

Gerritz, L., Wei, J., Fang, T., Wong, C., Klodt, A. L., Nizkorodov, S. A., and Shiraiwa, M.: Reactive Oxygen Species Formation and Peroxide and Carbonyl Decomposition in Aqueous Photolysis of Secondary Organic Aerosols, Environ. Sci. Technol., 58, 4716–4726, https://doi.org/10.1021/acs.est.3c08662, 2024.

Hearn, J. D. and Smith, G. D.: Measuring rates of reaction in supercooled organic particles with implications for atmospheric aerosol, Phys. Chem. Chem. Phys., 7, 2549–2551, https://doi.org/10.1039/b506424d, 2005.

Helms, J. R., Stubbins, A., Ritchie, J. D., Minor, E. C., Kieber, D. J., and Mopper, K.: Absorption spectral slopes and slope ratios as indicators of molecular weight, source, and photobleaching of chromophoric dissolved organic matter, Limnol. Oceanogr., 53, 955–969, https://doi.org/10.4319/lo.2008.53.3.0955, 2008.

Ibusuki, T. and Takeuchi, K.: Sulfur dioxide oxidation by oxygen catalyzed by mixtures of manganese(II) and iron(III) in aqueous solutions at environmental reaction conditions, Atmos. Environ., 21, 1555–1560, https://doi.org/10.1016/0004-6981(87)90317-9, 1986.

Ijaz, A., Temime-Roussel, B., Chazeau, B., Albertin, S., Arnold, S. R., Barrett, B., Bekki, S., Brett, N., Cesler-Maloney, M., Dieudonne, E., Dingilian, K. K., Fochesatto, J. G., Mao, J., Moon, A., Savarino, J., Simpson, W., Weber, R. J., Law, K. S., and D'Anna, B.: Complementary aerosol mass spectrometry elucidates sources of wintertime sub-micron particle pollution in Fairbanks, Alaska, during ALPACA 2022 , EGUsphere [preprint], https://doi.org/10.5194/egusphere-2024-3789, 2024.

Jiang, W., Misovich, M. V., Hettiyadura, A. P. S., Laskin, A., McFall, A. S., Anastasio, C., and Zhang, Q.: Photosensitized Reactions of a Phenolic Carbonyl from Wood Combustion in the Aqueous Phase – Chemical Evolution and Light Absorption Properties of AqSOA, Environ. Sci. Technol., 55, 5199–5211, https://doi.org/10.1021/acs.est.0c07581, 2021.

Jiang, W., Ma, L., Niedek, C., Anastasio, C., and Zhang, Q.: Chemical and Light-Absorption Properties of Water-Soluble Organic Aerosols in Northern California and Photooxidant Production by Brown Carbon Components, ACS Earth Space Chem., 7, 1107–1119, https://doi.org/10.1021/acsearthspacechem.3c00022, 2023a.

Jiang, W., Niedek, C., Anastasio, C., and Zhang, Q.: Photoaging of phenolic secondary organic aerosol in the aqueous phase: evolution of chemical and optical properties and effects of oxidants, Atmos. Chem. Phys., 23, 7103–7120, https://doi.org/10.5194/acp-23-7103-2023, 2023b.

Joo, T., Machesky, J. E., Zeng, L., Hass-Mitchell, T., Weber, R. J., Gentner, D. R., and Ng, N. L.: Secondary Brown Carbon Formation From Photooxidation of Furans From Biomass Burning, Geophys. Res. Lett., 51, 104900, https://doi.org/10.1029/2023GL104900, 2024.

Kapur, S., Edwards, K. C., Fang, T., Schervish, M., Lakey, P. S. J., Yang, Y., Robinson, E. S., DeCarlo, P. F., Simp-

son, W. R., Weber, R. J., and Shiraiwa, M.: Reactive oxygen species, environmentally persistent free radicals, and oxidative potential of outdoor and indoor particulate matter in Wintertime Fairbanks, Alaska, Aerosol Sci. Technol., 1–18, https://doi.org/10.1080/02786826.2024.2433656, 2024.

Kaur, R. and Anastasio, C.: First Measurements of Organic Triplet Excited States in Atmospheric Waters, Environ. Sci. Technol., 52, 5218–5226, https://doi.org/10.1021/acs.est.7b06699, 2018.

Kaur, R., Labins, J. R., Helbock, S. S., Jiang, W., Bein, K. J., Zhang, Q., and Anastasio, C.: Photooxidants from brown carbon and other chromophores in illuminated particle extracts, Atmos. Chem. Phys., 19, 6579–6594, https://doi.org/10.5194/acp-19-6579-2019, 2019.

Kiland, K. J., Mahrt, F., Peng, L., Nikkho, S., Zaks, J., Crescenzo, G. V., and Bertram, A. K.: Viscosity, Glass Formation, and Mixing Times within Secondary Organic Aerosol from Biomass Burning Phenolics, ACS Earth Space Chem., 7, 1388–1400, https://doi.org/10.1021/acsearthspacechem.3c00039, 2023.

Koop, T., Bookhold, J., Shiraiwa, M., and Pöschl, U.: Glass transition and phase state of organic compounds: Dependency on molecular properties and implications for secondary organic aerosols in the atmosphere, Phys. Chem. Chem. Phys., 13, 19238–19255, https://doi.org/10.1039/c1cp22617g, 2011.

Kotchenruther, R. A.: Source apportionment of $PM_{2.5}$ at multiple Northwest U.S. sites: Assessing regional winter wood smoke impacts from residential wood combustion, Atmos. Environ., 142, 210–219, https://doi.org/10.1016/j.atmosenv.2016.07.048, 2016.

Kuhn, J., Stutz, J., Bartels-Rausch, T., Thomas, J. L., Cesler-Maloney, M., Simpson, W., Dibb, J. E., Heinlein, L. M. D., and Anastasio, C.: The interplay between snow and polluted air masses in cold urban environments, Faraday Discuss, 258, 502–520, https://doi.org/10.1039/D4FD00176A, 2024.

Laskin, A., Laskin, J., and Nizkorodov, S. A.: Chemistry of Atmospheric Brown Carbon, Chem. Rev., 115, 4335–4382, https://doi.org/10.1021/cr5006167, 2015.

Laskin, A., West, C. P., and Hettiyadura, A. P. S.: Molecular insights into the composition, sources, and aging of atmospheric brown carbon, Chem. Soc. Rev., 54, 1583–1612, https://doi.org/10.1039/D3CS00609C, 2025.

Leresche, F., Salazar, J. R., Pfotenhauer, D. J., Hannigan, M. P., Majestic, B. J., and Rosario-Ortiz, F. L.: Photochemical Aging of Atmospheric Particulate Matter in the Aqueous Phase, Environ. Sci. Technol., 55, 13152–13163, https://doi.org/10.1021/acs.est.1c00978, 2021.

Li, J., Zhang, Q., Wang, G., Li, J., Wu, C., Liu, L., Wang, J., Jiang, W., Li, L., Ho, K. F., and Cao, J.: Optical properties and molecular compositions of water-soluble and water-insoluble brown carbon (BrC) aerosols in northwest China, Atmos. Chem. Phys., 20, 4889–4904, https://doi.org/10.5194/acp-20-4889-2020, 2020.

Liang, Z., Zhou, L., Chang, Y., Qin, Y., and Chan, C. K.: Biomass-burning organic aerosols as a pool of atmospheric reactive triplets to drive multiphase sulfate formation, P. Natl. Acad. Sci. USA, 121, e2416803121, https://doi.org/10.1073/pnas.2416803121, 2024.

Lyu, Y., Lam, Y. H., Li, Y., Borduas-Dedekind, N., and Nah, T.: Seasonal variations in the production of singlet oxygen and organic triplet excited states in aqueous $PM_{2.5}$ in Hong Kong SAR, South China, Atmos. Chem. Phys., 23, 9245–9263, https://doi.org/10.5194/acp-23-9245-2023, 2023.

Ma, L., Guzman, C., Niedek, C., Tran, T., Zhang, Q., and Anastasio, C.: Kinetics and Mass Yields of Aqueous Secondary Organic Aerosol from Highly Substituted Phenols Reacting with a Triplet Excited State, Environ. Sci. Technol., 55, 5772–5781, https://doi.org/10.1021/acs.est.1c00575, 2021.

Ma, L., Worland, R., Tran, T., and Anastasio, C.: Evaluation of Probes to Measure Oxidizing Organic Triplet Excited States in Aerosol Liquid Water, Environ. Sci. Technol., 57, 6052–6062, https://doi.org/10.1021/acs.est.2c09672, 2022.

Ma, L., Worland, R., Jiang, W., Niedek, C., Guzman, C., Bein, K. J., Zhang, Q., and Anastasio, C.: Predicting photooxidant concentrations in aerosol liquid water based on laboratory extracts of ambient particles, Atmos. Chem. Phys., 23, 8805–8821, https://doi.org/10.5194/acp-23-8805-2023, 2023.

Ma, L., Worland, R., Heinlein, L., Guzman, C., Jiang, W., Niedek, C., Bein, K. J., Zhang, Q., and Anastasio, C.: Seasonal variations in photooxidant formation and light absorption in aqueous extracts of ambient particles, Atmos. Chem. Phys., 24, 1–21, https://doi.org/10.5194/acp-24-1-2024, 2024.

Madronich, S. and Flocke, S.: The role of solar radiation in atmospheric chemistry, in: Handbook of Environmental Chemistry, Springer-Verlag, 1–26, https://doi.org/10.1007/978-3-540-69044-3_1, 1998.

Manfrin, A., Nizkorodov, S. A., Malecha, K. T., Getzinger, G. J., McNeill, K., and Borduas-Dedekind, N.: Reactive Oxygen Species Production from Secondary Organic Aerosols: The Importance of Singlet Oxygen, Environ. Sci. Technol., 53, 8553–8562, https://doi.org/10.1021/acs.est.9b01609, 2019.

Mao, J., Fan, S., Jacob, D. J., and Travis, K. R.: Radical loss in the atmosphere from Cu-Fe redox coupling in aerosols, Atmos. Chem. Phys., 13, 509–519, https://doi.org/10.5194/acp-13-509-2013, 2013.

Mao, J., Bali, K., Campbell, J. R., Robinson, E. S., DeCarlo, P. F., Ijaz, A., Temime-Roussel, B., Barbara, D., Ketcherside, D., Yokelson, R. J., Hu, L., Cesler-Maloney, M., Simpson, W., Guo, F., Flynn, J., St. Clair, J., Nenes, A., and Weber, R.: Multiphase sulfur chemistry facilitates particle growth in a cold and dark urban environment, Faraday Discuss, 258, 357–374, https://doi.org/10.1039/D4FD00170B, 2024.

Martin, L. R. and Hill, M. W.: The Effect of Ionic Strength on the Manganese Catalyzed Oxidation of Sulfur (IV), Atmos. Environ., 21, 2267–2270, https://doi.org/10.1016/0004-6981(87)90361-1, 1987.

McNeill, K. and Canonica, S.: Triplet state dissolved organic matter in aquatic photochemistry: Reaction mechanisms, substrate scope, and photophysical properties, Environ. Sci. Process. Impacts, 18, 1381–1399, https://doi.org/10.1039/c6em00408c, 2016.

Moon, A., Jongebloed, U., Dingilian, K., Schauer, A., Chan, Y.-C., Cesler-Maloney, M., Simpson, W., Weber, R., Tsiang, L., Yazbeck, F., Zhai, S., Wedum, A., Turner, A., Albertin, S., Bekki, S., Savarino, J., Gribanov, K., Pratt, K., Costa, E., Anastasio, C., Sunday, M., Heinlein, L., Mao, J., and Alexander, B.: Fairbanks sulfate isotope measurements during ALPACA (2022), Arctic Data Center [data set], https://doi.org/10.18739/A2Q52FF68, 2023.

Moon, A., Jongebloed, U., Dingilian, K. K., Schauer, A. J., Chan, Y.-C., Cesler-Maloney, M., Simpson, W. R., Weber, R. J., Tsiang, L., Yazbeck, F., Zhai, S., Wedum, A., Turner, A. J., Albertin, S.,

Bekki, S., Savarino, J., Gribanov, K., Pratt, K. A., Costa, E. J., Anastasio, C., Sunday, M. O., Heinlein, L. M. D., Mao, J., and Alexander, B.: Primary Sulfate Is the Dominant Source of Particulate Sulfate during Winter in Fairbanks, Alaska, ES&T Air, 1, 139–149, https://doi.org/10.1021/acsestair.3c00023, 2024.

Mu, Y., Chen, J., Herrmann, H., Ye, C., Chen, H., Hoffmann, E. H., Mettke, P., Tilgner, A., He, L., Mutzel, A., Brüggemann, M., Poulain, L., Schaefer, T., Heinold, B., Ma, Z., Liu, P., Xue, C., Zhao, X., Zhang, C., Zhang, F., Sun, H., Li, Q., Wang, L., Yang, X., Wang, J., Liu, C., and Xing, C.: Particle-phase photoreactions of Hulis and TMIs establish a strong source of H_2O_2 and particulate sulfate in the winter North China Plain, Environ. Sci. Technol., 55, 7818–7830, https://doi.org/10.1021/acs.est.1c00561, 2021.

Önnby, L., Salhi, E., McKay, G., Rosario-Ortiz, F. L., and von Gunten, U.: Ozone and chlorine reactions with dissolved organic matter – Assessment of oxidant-reactive moieties by optical measurements and the electron donating capacities, Water Res., 144, 64–75, https://doi.org/10.1016/j.watres.2018.06.059, 2018.

Ossola, R., Jönsson, O. M., Moor, K., and McNeill, K.: Singlet Oxygen Quantum Yields in Environmental Waters, Chem. Rev., 121, 4100–4146, https://doi.org/10.1021/acs.chemrev.0c00781, 2021.

Peuravuori, J. and Pihlaja, K.: Molecular size distribution and spectroscopic properties of aquatic humic substances, Anal. Chim. Acta, 337, 133–149, 1997.

Reid, J. P., Bertram, A. K., Topping, D. O., Laskin, A., Martin, S. T., Petters, M. D., Pope, F. D., and Rovelli, G.: The viscosity of atmospherically relevant organic particles, Nat. Commun., 9, 956, https://doi.org/10.1038/s41467-018-03027-z, 2018.

Remke, S. C., Bürgin, T. H., Ludvíková, L., Heger, D., Wenger, O. S., von Gunten, U., and Canonica, S.: Photochemical oxidation of phenols and anilines mediated by phenoxyl radicals in aqueous solution, Water Res., 213, 118095, https://doi.org/10.1016/j.watres.2022.118095, 2022.

Robinson, E. S., Cesler-Maloney, M., Tan, X., Mao, J., Simpson, W., and DeCarlo, P. F.: Wintertime spatial patterns of particulate matter in Fairbanks, AK during ALPACA 2022, Environ. Sci.-Atmospheres, 3, 568–580, https://doi.org/10.1039/d2ea00140c, 2023.

Robinson, E. S., Battaglia, M., Campbell, J. R., Cesler-Maloney, M., Simpson, W., Mao, J., Weber, R. J., and DeCarlo, P. F.: Multi-year, high-time resolution aerosol chemical composition and mass measurements from Fairbanks, Alaska, Environ. Sci.-Atmospheres, 4, 685–698, https://doi.org/10.1039/d4ea00008k, 2024.

Sander, R.: Compilation of Henry's law constants (version 5.0.0) for water as solvent, Atmos. Chem. Phys., 23, 10901–12440, https://doi.org/10.5194/acp-23-10901-2023, 2023.

Schmale, J., Arnold, S. R., Law, K. S., Thorp, T., Anenberg, S., Simpson, W. R., Mao, J., and Pratt, K. A.: Local Arctic Air Pollution: A Neglected but Serious Problem, Earths Fut., 6, 1385–1412, https://doi.org/10.1029/2018EF000952, 2018.

Schweitzer, G., Gronheid, R., Jordens, S., Lor, M., De Belder, G., Weil, T., Reuther, E., Müllen, K., and De Schryver, F. C.: Intramolecular directional energy transfer processes in dendrimers containing perylene and terrylene chromophores, J. Phys. Chem. A, 107, 3199–3207, https://doi.org/10.1021/jp026459s, 2003.

Seinfeld, J. H. and Pandis, S. N.: Atmospheric Chemistry and Physics: From Air Pollution to Climate Change, 3rd edn., Wiley, ISBN-13: 978-1118947401, 2016.

Shiraiwa, M., Li, Y., Tsimpidi, A. P., Karydis, V. A., Berkemeier, T., Pandis, S. N., Lelieveld, J., Koop, T., and Pöschl, U.: Global distribution of particle phase state in atmospheric secondary organic aerosols, Nat. Commun., 8, 15002, https://doi.org/10.1038/ncomms15002, 2017.

Simpson, W., Law, K., Schmale, J., Pratt, K., Arnold, S., Mao, J., Alexander, B., Anenberg, S., Baklanov, A., Bell, D., Brown, S., Creamean, J., de Boer, G., DeCarlo, P., Descari, S., Elleman, R., Flynn, J., Fochesatto, J., Ganzenfeld, L., Griffin, R., Järvi, L., Kaspari, S., Konstantinov, P., Murphy, J., Petäjä, T., Pye, H., Jean-Christophe Raut, J.-C., Roberts, T., Shiraiwa, M., Stutz, J., Thomas, J., Thornton, J., Weber, R., Webley, P., and Williams, B.: Alaskan Layered Pollution And Chemical Analysis (ALPACA) White Paper, 2019.

Simpson, W., Cesler-Maloney, M., and Hoskins-Chaddon, R.: Gas and meteorological measurements at the CTC site and Birch Hill in Fairbanks, Alaska, during the ALPACA-2022 field study, Arctic Data Center [data set], https://doi.org/10.18739/A27D2Q87W, 2023.

Simpson, W. R., Mao, J., Fochesatto, G. J., Law, K. S., DeCarlo, P. F., Schmale, J., Pratt, K. A., Arnold, S. R., Stutz, J., Dibb, J. E., Creamean, J. M., Weber, R. J., Williams, B. J., Alexander, B., Hu, L., Yokelson, R. J., Shiraiwa, M., Decesari, S., Anastasio, C., D'Anna, B., Gilliam, R. C., Nenes, A., St. Clair, J. M., Trost, B., Flynn, J. H., Savarino, J., Conner, L. D., Kettle, N., Heeringa, K. M., Albertin, S., Baccarini, A., Barret, B., Battaglia, M. A., Bekki, S., Brado, T. J., Brett, N., Brus, D., Campbell, J. R., Cesler-Maloney, M., Cooperdock, S., Cysneiros de Carvalho, K., Delbarre, H., DeMott, P. J., Dennehy, C. J. S., Dieudonné, E., Dingilian, K. K., Donateo, A., Doulgeris, K. M., Edwards, K. C., Fahey, K., Fang, T., Guo, F., Heinlein, L. M. D., Holen, A. L., Huff, D., Ijaz, A., Johnson, S., Kapur, S., Ketcherside, D. T., Levin, E., Lill, E., Moon, A. R., Onishi, T., Pappaccogli, G., Perkins, R., Pohorsky, R., Raut, J.-C., Ravetta, F., Roberts, T., Robinson, E. S., Scoto, F., Selimovic, V., Sunday, M. O., Temime-Roussel, B., Tian, X., Wu, J., and Yang, Y.: Overview of the Alaskan Layered Pollution and Chemical Analysis (ALPACA) Field Experiment, ACS ES&T Air, 1, 200–222, https://doi.org/10.1021/acsestair.3c00076, 2024.

Smith, J. D., Sio, V., Yu, L., Zhang, Q., and Anastasio, C.: Secondary organic aerosol production from aqueous reactions of atmospheric phenols with an organic triplet excited state, Environ. Sci. Technol., 48, 1049–1057, https://doi.org/10.1021/es4045715, 2014.

Smith, J. D., Kinney, H., and Anastasio, C.: Aqueous benzene-diols react with an organic triplet excited state and hydroxyl radical to form secondary organic aerosol, Phys. Chem. Chem. Phys., 17, 10227–10237, https://doi.org/10.1039/c4cp06095d, 2015.

Smith, J. D., Kinney, H., and Anastasio, C.: Phenolic carbonyls undergo rapid aqueous photodegradation to form low-volatility, light-absorbing products, Atmos. Environ., 126, 36–44, https://doi.org/10.1016/j.atmosenv.2015.11.035, 2016.

Song, H., Lu, K., Ye, C., Dong, H., Li, S., Chen, S., Wu, Z., Zheng, M., Zeng, L., Hu, M., and Zhang, Y.: A comprehensive observation-based multiphase chemical model analysis of sulfur dioxide oxidations in both summer and winter, Atmos. Chem.

Phys., 21, 13713–13727, https://doi.org/10.5194/acp-21-13713-2021, 2021.

Sunday, M. O., Dahler Heinlein, L. M., He, J., Moon, A., Kapur, S., Fang, T., Edwards, K. C., Guo, F., Dibb, J., Flynn III, J. H., Alexander, B., Shiraiwa, M., and Anastasio, C.: Hydrogen peroxide photoformation in particulate matter and its contribution to S(IV) oxidation during winter in Fairbanks, Alaska, Atmos. Chem. Phys., 25, 5087–5100, https://doi.org/10.5194/acp-25-5087-2025, 2025.

Tilgner, A., Schaefer, T., Alexander, B., Barth, M., Collett Jr., J. L., Fahey, K. M., Nenes, A., Pye, H. O. T., Herrmann, H., and McNeill, V. F.: Acidity and the multiphase chemistry of atmospheric aqueous particles and clouds, Atmos. Chem. Phys., 21, 13483–13536, https://doi.org/10.5194/acp-21-13483-2021, 2021.

Tomaz, S., Cui, T., Chen, Y., Sexton, K. G., Roberts, J. M., Warneke, C., Yokelson, R. J., Surratt, J. D., and Turpin, B. J.: Photochemical Cloud Processing of Primary Wildfire Emissions as a Potential Source of Secondary Organic Aerosol, Environ. Sci. Technol., 52, 11027–11037, https://doi.org/10.1021/acs.est.8b03293, 2018.

Tong, H., Arangio, A. M., Lakey, P. S. J., Berkemeier, T., Liu, F., Kampf, C. J., Brune, W. H., Pöschl, U., and Shiraiwa, M.: Hydroxyl radicals from secondary organic aerosol decomposition in water, Atmos. Chem. Phys., 16, 1761–1771, https://doi.org/10.5194/acp-16-1761-2016, 2016.

Virtanen, A., Joutsensaari, J., Koop, T., Kannosto, J., Yli-Pirilä, P., Leskinen, J., Mäkelä, J. M., Holopainen, J. K., Pöschl, U., Kulmala, M., Worsnop, D. R., and Laaksonen, A.: An amorphous solid state of biogenic secondary organic aerosol particles, Nature, 467, 824–827, https://doi.org/10.1038/nature09455, 2010.

Wang, J., Li, J., Ye, J., Zhao, J., Wu, Y., Hu, J., Liu, D., Nie, D., Shen, F., Huang, X., Huang, D. D., Ji, D., Sun, X., Xu, W., Guo, J., Song, S., Qin, Y., Liu, P., Turner, J. R., Lee, H. C., Hwang, S., Liao, H., Martin, S. T., Zhang, Q., Chen, M., Sun, Y., Ge, X., and Jacob, D. J.: Fast sulfate formation from oxidation of SO_2 by NO_2 and HONO observed in Beijing haze, Nat. Commun., 11, 2844, https://doi.org/10.1038/s41467-020-16683-x, 2020a.

Wang, W., Liu, M., Wang, T., Song, Y., Zhou, L., Cao, J., Hu, J., Tang, G., Chen, Z., Li, Z., Xu, Z., Peng, C., Lian, C., Chen, Y., Pan, Y., Zhang, Y., Sun, Y., Li, W., Zhu, T., Tian, H., and Ge, M.: Sulfate formation is dominated by manganese-catalyzed oxidation of SO_2 on aerosol surfaces during haze events, Nat. Commun., 12, 1993, https://doi.org/10.1038/s41467-021-22091-6, 2021.

Wang, X., Gemayel, R., Hayeck, N., Perrier, S., Charbonnel, N., Xu, C., Chen, H., Zhu, C., Zhang, L., Wang, L., Nizkorodov, S. A., Wang, X., Wang, Z., Wang, T., Mellouki, A., Riva, M., Chen, J., and George, C.: Atmospheric Photosensitization: A New Pathway for Sulfate Formation, Environ. Sci. Technol., 54, 3114–3120, https://doi.org/10.1021/acs.est.9b06347, 2020b.

Xie, M., Hays, M. D., and Holder, A. L.: Light-Absorbing organic carbon from prescribed and laboratory biomass burning and gasoline vehicle emissions, Sci. Rep., 7, 7318, https://doi.org/10.1038/s41598-017-06981-8, 2017.

Ye, C., Mu, Y., Chen, J., Chen, H., Hoffmann, E. H., Mettke, P., Tilgner, A., He, L., Mutzel, A., Brüggemann, M., Herrmann, H., Poulain, L., Schaefer, T., Heinold, B., Ma, Z., Liu, P., Xue, C., Zhao, X., Zhang, C., Zhang, F., Sun, H., Li, Q., Wang, L., Yang, X., Wang, J., Liu, C., and Xing, C.: Particle-phase photoreactions of HULIS and TMIs establish a strong source of H_2O_2 and particulate sulfate in the winter North China Plain, Environ. Sci. Technol., 55, 7818–7830, https://doi.org/10.1021/acs.est.1c00561, 2021.

Yu, C., Liu, T., Ge, D., Nie, W., Chi, X., and Ding, A.: Ionic Strength Enhances the Multiphase Oxidation Rate of Sulfur Dioxide by Ozone in Aqueous Aerosols: Implications for Sulfate Production in the Marine Atmosphere, Environ. Sci. Technol., 57, 6609–6615, https://doi.org/10.1021/acs.est.3c00212, 2023.

Yu, L., Smith, J., Laskin, A., Anastasio, C., Laskin, J., and Zhang, Q.: Chemical characterization of SOA formed from aqueous-phase reactions of phenols with the triplet excited state of carbonyl and hydroxyl radical, Atmos. Chem. Phys., 14, 13801–13816, https://doi.org/10.5194/acp-14-13801-2014, 2014.

Yu, L., Smith, J., Laskin, A., George, K. M., Anastasio, C., Laskin, J., Dillner, A. M., and Zhang, Q.: Molecular transformations of phenolic SOA during photochemical aging in the aqueous phase: competition among oligomerization, functionalization, and fragmentation, Atmos. Chem. Phys., 16, 4511–4527, https://doi.org/10.5194/acp-16-4511-2016, 2016.

Zhang, J., Shrivastava, M., Zelenyuk, A., Zaveri, R. A., Surratt, J. D., Riva, M., Bell, D., and Glasius, M.: Observationally Constrained Modeling of the Reactive Uptake of Isoprene-Derived Epoxydiols under Elevated Relative Humidity and Varying Acidity of Seed Aerosol Conditions, ACS Earth Space Chem., 7, 788–799, https://doi.org/10.1021/acsearthspacechem.2c00358, 2022.

Zobrist, B., Marcolli, C., Pedernera, D. A., and Koop, T.: Do atmospheric aerosols form glasses?, Atmos. Chem. Phys., 8, 5221–5244, https://doi.org/10.5194/acp-8-5221-2008, 2008.

Supplement of Atmos. Chem. Phys., 25, 9561–9581, 2025
https://doi.org/10.5194/acp-25-9561-2025-supplement

Atmospheric Chemistry and Physics
Open Access
EGU

Supplement of

Surprisingly robust photochemistry in subarctic particles during winter: evidence from photooxidants

Laura M. D. Heinlein et al.

Correspondence to: Cort Anastasio (canastasio@ucdavis.edu)

Table of Contents

Section S1. Sample collection and storage

At the CTC site, $PM_{2.5}$ filter samples were collected with a 4-stage cascade impactor using quartz filters (TE-QMA and TE-230-QZ). Prior to sample collection, the filters were rinsed with 18 MΩ-cm water, baked at 500 ºC for 8 hours, wrapped in aluminum foil, and stored in airtight polyethylene bags. At the House site, filter samples were collected on quartz microfiber filters (Pallflex Emfab). The filters were precleaned by gently shaking in Milli-Q water for 4 hours, dried at 100 ºC, baked at 550 ºC for 5 hours, stored in aluminum foil (treated by baking at 550 ºC for 12 hours), and placed in airtight polyethylene bags until sample collection. After sample collection, filters were again wrapped in aluminum foil, placed in air-tight polyethylene bags, transported over ice in coolers, and then stored in a -20 ºC freezer. Because filters were shared among several groups, ¼ of each filter was cut off at UC Irvine or the University of Washington, wrapped in aluminum foil, placed in air-tight polyethylene bags, and shipped to UC Davis in a cooler over ice. The quarter filters were then stored at Davis in a -20 ºC freezer until extraction.

Section S2. Screening factor calculation

In the solar simulator, as light passes through the 1 mL reaction tube and is absorbed by the solution, the photon flux decreases (Smith et al., 2016). To account for this attenuation of light though the reaction tube, we calculated the screening factor (S_λ) for each extract:

$$S_\lambda = \frac{\sum[(1 - 10^{-A_\lambda}) \times I_\lambda]}{\sum[(2.303 \times A_\lambda) \times I_\lambda]} \quad \text{(S1)}$$

where A_λ is the absorbance of the particulate matter extract at wavelength λ (unitless) and I_λ is the photon flux of the solar simulator at wavelength λ (Smith et al., 2016). The measured pseudo-first order decay rates of probes are then corrected for screening using equation 2.

Section S3. Rate of light absorbance calculation

The rate of light absorbance in a PM extract in the solar simulator was calculated with

$$R_{\text{abs,EXP,PME}} = \frac{[\text{DOC}]_{\text{PME}}}{10^3} \times \sum_{300\text{ nm}}^{550\text{ nm}} (\text{MAC}_\lambda \times I_{\lambda,\text{EXP}} \times \Delta\lambda) \quad \text{(S2)}$$

where $[DOC]_{PME}$ is the dissolved organic carbon concentration in the extract (mg L^{-1}), the 10^3 factor is a unit conversion of mg to g, MAC_λ is the DOC-normalized mass absorption cross section at wavelength λ (cm^2 g^{-1}), $I_{\lambda,EXP}$ is the surface-area-normalized photon flux at wavelength λ in the illuminated quartz tube (mol-photons cm^{-2} nm^{-1} s^{-1}), and Δλ is the wavelength interval between discreet I_λ values (nm) (Kaur et al., 2019). In our simulated sunlight illumination system, we determined $I_{\lambda,EXP}$ as described in Hullar et al. (2020). Note that this $R_{abs,EXP,PME}$ only accounts for the light absorbed by water-soluble species that were extracted from the $PM_{2.5}$ filters into our extracts. Water-insoluble BrC, which also absorbs light and produces photooxidants, is not included in our water extracts.

Section S4. Experimental kinetic calculation: oxidant concentrations and oxidant production rates

All rates of light absorbance, photooxidant concentrations, and photooxidant production rates in this paper are reported under two actinic flux conditions: (1) at j_{2NB} = 0.0045 s^{-1}, the photolysis frequency of 2-nitrobenzaldehyde for Fairbanks midday actinic flux on February 1st, 2022 determined using actinic sunlight modeled by Tropospheric Ultraviolet and Visible (TUV) Radiation (Madronich and Flocke, 1998), or (2) at the photon flux condition determined for each specific composite period (Section 2.6.1).

S4.1 Hydroxyl Radical

The •OH steady-state concentrations under laboratory conditions were measured using a low concentration (10 μM) of the probe benzoic acid (BA) (Anastasio and McGregor, 2001; Kaur et al., 2019; Ma et al., 2024). •OH concentrations were determined for each sample by simultaneously monitoring the loss of BA and the production of para-hydroxybenzoic acid (*p*-HBA) (Ma et al., 2022, 2023, 2024). The loss of BA was fit and normalized to a standard photon flux using equations 1 and 2 to determine the first-order rate constant for BA loss, $k'_{BA,EXP}$. The experimental •OH concentration in our PM extract (PME) was determined with

$$[\bullet OH]_{EXP,PME} = \frac{k'_{BA,EXP}}{k_{\bullet OH+BA}} \quad (S3)$$

where $k_{\bullet OH+BA}$ is the second-order rate constant for the reaction of •OH with BA at the pH of the extract, determined based on the rate constants for •OH with benzoic acid and benzoate (4.3×10^9 M^{-1} s^{-1} for benzoic acid, Ashton et al., 1995; Wander et al., 1968; 5.9×10^9 M^{-1} s^{-1} for benzoate, Ross et al., 1994) and the mole fractions of neutral and deprotonated benzoic acid (pK_a = 4.2; Wander et al., 1968). The production of *p*-HBA was fit using

$$[p-\mathrm{HBA}]_t = [p-\mathrm{HBA}]_0 + A(1-e^{-Bt}) \quad (S4)$$

where $[p\text{-HBA}]_0$ is the initial concentration, $[p\text{-HBA}]_t$ is the concentration at time t, and A and B are fitted parameters (Ma et al., 2023, 2024). The product of A and B is the initial rate of p-HBA production ($R_{p\text{-HBA,EXP}}$), which is used to calculate the steady-state •OH concentration:

$$[\bullet\mathrm{OH}]_{\mathrm{EXP,PME}} = \frac{R_{p-\mathrm{HBA,EXP}}}{[\mathrm{BA}]_0 \times k_{\bullet\mathrm{OH+BA}} \times Y_{p-\mathrm{HBA}}} \quad \text{(S5)}$$

where $[\mathrm{BA}]_0$ is the initial BA concentration and $Y_{p\text{-HBA}}$ is the yield of p-HBA from the reaction of •OH and BA (17%) (Anastasio and McGregor, 2001). The reported •OH concentration for a given extract is the average of the values determined by BA loss and p-HBA production. The average (±1σ) relative percent difference in •OH concentration determined for the two methods is 18(±51)%.

The steady-state •OH concentration was used to estimate the production rate of •OH in each extract with

$$P_{\bullet\mathrm{OH,EXP,PME}} = [\bullet\mathrm{OH}]_{\mathrm{EXP,PME}} \times k_{\bullet\mathrm{OH+DOC}} \times [\mathrm{DOC}]_{\mathrm{PME}} \quad \text{(S6)}$$

where $k_{\bullet\mathrm{OH+DOC}}$ is the general second-order rate constant for reaction of •OH with atmospheric DOC, 3.8(±1.9) × 10^8 L mol-C^{-1} s^{-1} (Arakaki et al., 2013). This assumes that DOC is the dominant •OH sink (Ma et al., 2023), which should be true for our DOC-rich extracts.

S4.2 Singlet Molecular Oxygen

Steady-state $^1O_2$* concentrations were measured using a low concentration (10 μM) of the probe furfuryl alcohol (FFA) (Anastasio and McGregor, 2001; Appiani et al., 2017; Bogler et al., 2022; Kaur et al., 2019; Ma et al., 2024). Initially, we used the D_2O diagnostic method to measure $^1O_2$*. With this technique, two parallel experiments were performed: PM extracts were diluted 2-fold with either Milli-Q H_2O or D_2O, which varies the rate constant for $^1O_2$* quenching by the solvent (Ma et al., 2023). While this technique has been successfully used to quantify $^1O_2$* in the past under more moderate pH conditions (Anastasio and McGregor, 2001; Haag and Hoigne, 1986; Ma et al., 2023), in our pH 1 extracts the D_2O method systematically underestimated [$^1O_2$*] compared to the result determined measuring FFA loss in Milli-Q (with correction for the loss of FFA due to •OH). Thus we measured FFA decay in our pH 1 extract without D_2O, assuming the dominant loss of $^1O_2$* was to the solvent H_2O. The normalized pseudo-first-order rate constant for FFA loss (k'_{FFA}) was determined using equations 2 and 3. We corrected for FFA loss due to •OH in order to determine the rate constant for FFA loss due to $^1O_2$* using

$$k'_{\mathrm{FFA},1O2*} = k'_{\mathrm{FFA}} - k_{\bullet\mathrm{OH+FFA}} \times [\bullet\mathrm{OH}]_{\mathrm{EXP,PME}} \quad \text{(S7)}$$

where $k_{\bullet OH+FFA}$ is the second-order rate constant for FFA loss due to •OH, 1.5×10^{10} M^{-1} s^{-1} (Ross and Ross, 1977). The steady-state $^1O_2$* concentrations were then calculated using an equation analogous to equation S3, with the denominator being the second-order rate constant for FFA reacting with $^1O_2$* (at 10 °C, $k_{1O2*+FFA}$ is 8.06×10^7 M^{-1} s^{-1}; Appiani et al., 2017). The production rate of $^1O_2$* was predicted with an equation similar to equation S6, assuming that in the dilute particle extracts $^1O_2$* loss was mainly due to quenching by H_2O ($k'_{1O2*,H2O}$ = $2.76(\pm0.02)\times10^5$ s^{-1}), with minor loss due to $^1O_2$* reacting with DOC ($k_{1O2*+DOC}$ = 1×10^5 M^{-1} s^{-1}) (Appiani et al., 2017; Ma et al., 2023). In the dilute extracts, this is a reasonable assumption because H_2O and DOC are the two dominant $^1O_2$* sinks (Ma et al., 2023).

S4.3 Triplet Excited States

The steady-state concentration of ^3C* was determined using a low concentration (10 μM) of the probe syringol (SYR), which reacts with the subset of the triplet population that is oxidizing (Ma et al., 2022, 2023). A limitation to the SYR probe is that after SYR reacts with ^3C*, the oxidized syringyl phenoxyl radical can be reduced by other phenols or dissolved copper in solution to regenerate the parent SYR probe (Ma et al., 2022). This regeneration inhibits SYR loss and leads to an underestimate of ^3C* concentrations (Ma et al., 2022, 2023; Wenk and Canonica, 2012). To account for probe regeneration, we measured the inhibition factor ($IF_{SYR,corr}$), which quantifies the fraction of ^3C* and SYR reactions that lead to SYR loss (Section S5). Additionally, because SYR reacts with •OH and $^1O_2$*, we correct k'_{SYR} for SYR loss due to reactions with •OH and $^1O_2$*. Accounting for all corrections, the steady state ^3C* concentration was then determined by

$$[^3C*]_{EXP,PME} = \frac{k'_{SYR,EXP} - k_{SYR+\bullet OH} \times [\bullet OH]_{EXP,PME} - k_{SYR+1O2*} \times [^1O_2*]_{EXP,PME}}{k_{SYR+3C*} \times IF_{SYR,corr}} \quad (S8)$$

where $k_{SYR+\bullet OH}$ and $k_{SYR+1O2*}$ are the second-order rate constants for loss of SYR due to reaction with •OH and $^1O_2$*, respectively (Ma et al., 2022). Finally, the ^3C* production rate in extracts was estimated using an equation analogous to equation S6, calculated using reactions of triplets with dissolved O_2 as the dominant sink (k_{3C*+O2} = 2.8×10^9 M^{-1} s^{-1}) and with DOC as a minor sink ($k_{3C*+DOC,SYR}$ = 7×10^7 M^{-1} s^{-1}) (Kaur et al., 2019; Ma et al., 2023). In the dilute extracts, this is a reasonable assumption because other ^3C* sinks, such as S(IV), are expected to be negligible in our PM extracts (Ma et al., 2023).

Section S5. Inhibition factor (Ma et al., 2022)

DOC in dilute particle extract can artificially suppress $[^3C*]_{EXP,PME}$. When ^3C* react with SYR, the product is a phenoxy radical, which can abstract a hydrogen from DOC to reform SYR, causing an artificial suppression in SYR loss. However, because DOC is a ^3C* sink, DOC also causes a real suppression in $[^3C*]_{EXP,PME}$ concentration and thus a smaller observed k'_{SYR}. We measure two inhibition factors to account for both types of inhibition by DOC.

The first inhibition factor we measured is the inhibition of the SYR probe (IF_{SYR}) which represents both inhibition due to quenching by DOC and inhibition due to the regeneration of the SYR probe. To measure IF_{SYR}, we performed three separate experiments. First, we spike 1 mL of a dilute extract with 10 μM SYR and measure the pseudo-first order decay of SYR ($k'_{SYR+PME}$). Next, we spike 1 mL of the dilute extract with 10 μM SYR and 80 μM of 3,4-dimethoxybenzaldehyde (DMB), a photosensitizer that produces $^3C^*$ ($k'_{SYR+DMB+PME}$). Lastly, we spike 1 mL of sulfuric acid (either pH 1 or pH 5, depending on pH of the extract we are testing) with 10 μM SYR and 80 μM DMB and measured the decay of SYR over time ($k'_{SYR+DMB}$). We then calculate IF_{SYR} by

$$IF_{SYR} = \frac{k'_{SYR+PME+DMB} - k'_{SYR+PME}}{k'_{SYR+DMB}}. \quad (S9)$$

DMB produces $^3C^*$, which react with SYR and lead to enhanced SYR loss, so we expect $k'_{SYR+DMB+PME}$ to be larger than $k'_{SYR+PME}$. If no inhibition occurs, $k'_{SYR+DMB}$ will be equivalent to the sum of $k'_{SYR+DMB+PME}$ and $k'_{SYR+PME}$ and IF_{SYR} will be 1. However, if either type of inhibition occurs, IF_{SYR} will be less than 1. Because IF_{SYR} accounts for both types of inhibition, but the $[^3C^*]_{EXP,PME}$ must only be corrected for the inhibition caused by regeneration of the SYR probe, we measure a second inhibition factor which only accounts for inhibition due to quenching of $^3C^*$ by DOC.

The second inhibition factor we measure is the inhibition of the probe FFA (IF_{FFA}). Analogous to IF_{SYR}, IF_{FFA} is measured by performing three experiments. First, we spike 1 mL of a dilute extract with 10 μM FFA and measure the decay of FFA over the illumination period ($k'_{FFA+PME}$). Next, we spike 1 mL of the dilute extract with 10 μM FFA and 80 μM of 3,4-dimethoxybenzaldehyde (DMB) ($k'_{FFA+DMB+PME}$). Lastly, we spike 1 mL of sulfuric acid (either pH 1 or pH 5) with 10 μM FFA and 80 μM DMB and measure the decay of FFA over time ($k'_{FFA+DMB}$). We then calculate IF_{FFA} with an equation analogous to equation S9. Finally, we correct IF_{SYR} by IF_{FFA} using

$$IF_{SYR,corr} = \frac{IF_{SYR}}{IF_{FFA}} \quad (S10)$$

where $IF_{SYR,corr}$ only accounts for the inhibition caused by the regeneration of the SYR probe.

Section S6. Calculating the concentration of dissolved organic carbon in aerosol liquid water

The DOC concentration in ALW was calculated using the flow rate of filter collection and the DOC measured in our PM extracts. First, the volume of air collected (m^3) per filter composite was calculated with

$$V_{air} = \sum_1^n \frac{Q \times t \times A_{extract}}{A_{total}} \quad (S11)$$

where n is the number of filters in each composite, Q is the flow rate reported for each filter ($m^3\ s^{-1}$; Edwards et al., 2024; Moon et al., 2024), t is the collection time for each filter (s), A_{extract} is the area from each filter that was used to prepare the extract (cm^2), and A_{total} is the total area of a complete (i.e., uncut) filter (cm^2). V_{air} is calculated by adding up the volume of air sampled across the n filters used to make a given composite.

Next, the DOC concentration in ALW (mol-C $L\text{-}aq^{-1}$) was calculated with

$$[\mathrm{DOC}]_{\mathrm{ALW}} = \frac{[\mathrm{DOC}]_{\mathrm{PME}} \times V_{\mathrm{aq}}}{V_{\mathrm{air}} \times \mathrm{ALWC}} \quad \text{(S12)}$$

where $[\mathrm{DOC}]_{\mathrm{PME}}$ is the concentration of dissolved organic carbon measured in our PM filter extracts (mol-C L^{-1}), V_{aq} is the total volume of solution used to extract the filters in a composite (L), and ALWC is the aerosol liquid water content reported by Campbell et al. (2024) averaged over each composite (L-aq $L\text{-}air^{-1}$). Finally, the concentration factor (CF) between ALW conditions and our PM extracts was determined using

$$CF = \frac{[\mathrm{DOC}]_{\mathrm{ALW}}}{[\mathrm{DOC}]_{\mathrm{PME}}} \quad \text{(S13)}$$

Values are reported in Table S12. The CF was used to extrapolate values measured in our dilute extracts (e.g., PM-mass/H_2O-mass ratios and P_{ox}) to ALW conditions.

Section S7. Estimating the inorganic S(IV) activities and activity coefficients

S7.1. Calculating the Inorganic S(IV) Activity

A large uncertainty in our model of S(IV) oxidation pathways is the activity of inorganic S(IV). Measured S(IV) in the particles was categorized based on its susceptibility to oxidation by HOOH: total S(IV) measured by ion chromatography in filter extracts was considered the sum of inorganic S(IV) and hydroxymethanesulfonate (HMS), while HMS was determined as the S(IV) measured after hydrogen peroxide was added to the extracts to remove inorganic S(IV) (Dingilian et al., 2024). The difference of these two measurements should be the inorganic S(IV) amount. However, measured inorganic S(IV) concentrations in ALW (0.1–0.7 M, Dingilian et al., 2024) were roughly three orders of magnitude larger than predicted from Henry's law partitioning of SO_2 (corrected for temperature and ionic strength) assuming the ALW is pH 5 (resulting in 0.02-0.3 mM inorganic S(IV)) and six orders of magnitude higher assuming pH 1 ALW (0.02-0.2 μM).

To constrain the modeled particulate inorganic S(IV), we modeled the rate of secondary SO_4^{2-} formation as a function of inorganic S(IV) activity (Figure 8a-d). We then defined the model estimate of inorganic S(IV) activity as the point where the

modeled fraction of secondary sulfate from HOOH – the dominant secondary sulfate source (Sunday et al., 2024) – matched the fraction measured by sulfate isotope measurements (Moon et al., 2024). Under the high-NO_x conditions in Fairbanks, gas-phase HOOH concentrations are expected to be low (Ye et al., 2018). Sunday et al. (2024) describe that in-particle photochemistry is the main source of HOOH, with HOOH likely photochemically formed by $^3C^*$ reactions with phenols (Anastasio et al., 1997; Sunday et al., 2024). Our model uses the in-particle formation rates of sulfate reported by Sunday et al. (2024). Under the high-SO_2 conditions of ALPACA, HOOH is a unique condensed-phase oxidant because its rate of SO_4^{2-} production is independent of {inorganic S(IV)}, a consequence of S(IV) being by far the most important sink for particle-phase HOOH (Sunday et al., 2024). In contrast, the other condensed-phase SO_4^{2-} formation pathways studied here become slower as {inorganic S(IV)} decreases. This property of the HOOH pathway allowed us to estimate the inorganic S(IV) activity.

S7.2 Calculating the Inorganic S(IV) Activity Coefficient

We estimated the activity coefficient of inorganic S(IV) using the ionic-strength correction to Henry's Law for SO_2 described in Millero et al. (1989). The activity coefficient for inorganic S(IV) was estimated using

$$\gamma_{I_s} = \frac{H_{SO_2}}{H_{SO_2}^{I_s=0}} \tag{S14}$$

where $H_{SO_2}^{I_s=0}$ is temperature-adjusted Henry's Law constant for SO_2, determined with

$$H_{SO_2}^{I_s=0} = 1.23 \times e^{\left(3145.3\times\left(\frac{1}{T}-\frac{1}{298}\right)\right)} \tag{S15}$$

(Seinfeld and Pandis, 2016) and H_{SO_2} is the Henry's Law constant for SO_2 at the same temperature but a non-zero ionic strength, determined with

$$log_{10}\left(\frac{H_{SO_2}}{H_{SO_2}^{I_s=0}}\right) = \left(\frac{22.3}{T} - 0.0997\right) \times I_s \quad (I_{s,max} = 6\ M) \tag{S16}$$

(Millero et al., 1989). While the ionic strength correction has been tested for $I_s \leq 6$ M, we use it for all our ALW calculations, where I_s values are as high as 23 M, due to of a lack of alternatives. The range of activity coefficients for aqueous SO_2 calculated in this work were 0.69-0.82 (Table S20).

Section S8. Isotopic signature of sulfate formed by $^3C^*$

We expect the dominant mechanism of SO_4^{2-} formation by $^3C^*$ to be either electron transfer or proton-coupled electron transfer from inorganic S(IV) to the oxidizing triplet excited state (McNeill and Canonica, 2016; Moon et al., 2024; Wang et al., 2020). The resulting isotopic signature of SO_4^{2-} formed by $^3C^*$ is equivalent to that of SO_4^{2-} formed from transition metal ions (TMI) (Moon et al., 2024). This indicates that the secondary SO_4^{2-} formed by TMI reported by Moon et al. (2024) represents the SO_4^{2-} formed by both $^3C^*$ and TMI.

Section S9. Determination of monthly photolysis frequencies for O_3, HONO, and BrC

Rate constants for photolysis of HONO and O_3 (i.e., $j_{HONO\rightarrow\bullet OH}$ and $j_{O3\rightarrow O(1D)}$) on the 15th of each month were determined with TUV using constant column O_3 and aerosol optical depth (AOD), and with albedo estimated using ALPACA measurements (Table S22). Values of $j_{O3\rightarrow O(1D)}$ were converted to $j_{O3\rightarrow\bullet OH}$ by estimating the fraction of $O(^1D)$ lost due to reaction with H_2O (Table S23). First, we assumed the dominant loss pathways of $O(^1D)$ were H_2O, N_2, and O_2 (Seinfeld & Pandis, 2016). The H_2O gas concentration was determined using the monthly average relative humidity reported by the US Climate Research Network and temperatures reported by the Alaska Department of Transportation, both listed on the NOAA Environmental Research Division's Data Access Program Website (AK Fairbanks 11 NE, 2024). We calculated the temperature-dependent saturation vapor pressure for water as described in Seinfeld and Pandis (2016). The concentration of water was estimated by multiplying the saturation vapor pressure by the relative humidity. The temperature-dependent total concentration of gas molecules (i.e., Loschmidt's constant) was calculated using the ideal gas law and used to convert the concentration of H_2O to mlc cm^{-3}. We assume N_2 and O_2 were 78.8% and 20.95% of the total gas concentration, respectively. The pseudo-first order rate constants for $O(^1D)$ loss due to reaction with H_2O, N_2 and O_2 were then calculated using the respective temperature-corrected second-order rate constants (Seinfeld & Pandis, 2016). Using the pseudo-first order loss rate constants, the fraction of $O(^1D)$ loss due to reaction with H_2O ($f_{O(1D),H2O}$) was determined with

$$f_{O(1D),H2O} = \frac{k'_{O(1D),H2O}}{k'_{O(1D),H2O} + k'_{O(1D),N2} + k'_{O(1D),O2}} \quad \text{(S17)}$$

where each $k'_{O(1D)}$ term represents the pseudo-first order rate constant for $O(^1D)$ loss due to H_2O, N_2 and O_2. Finally, the rate of $^\bullet$OH formation from ozone photolysis, $P_{O3\rightarrow\bullet OH}$, was calculated by multiplying $P_{O3\rightarrow O(1D)}$ with the fraction of $O(^1D)$ loss due to reaction with H_2O

$$P_{O3\rightarrow\bullet OH} = P_{O3\rightarrow O(1D)} \times f_{O(1D),H2O} \times 2 \quad \text{(S18)}$$

where the factor of two accounts for the molar ratio of two $^\bullet$OH produced per $O(^1D)$ lost to reaction with water vapor. The value of $j_{O3\rightarrow\bullet OH}$ was then determined by dividing $P_{O3\rightarrow\bullet OH}$ by the O_3 concentration.

Rate constants for formation of oxidizing triplets following light absorption by brown carbon ($j_{BrC \rightarrow 3C*}$) were determined using TUV-modelled I_λ, the average MAC_λ determined from all House site samples, and the average Φ_{3C*} (2.7%) determined in this work. Values were determined for the wavelength range of 300 to 550 nm. TUV overestimates low-energy wavelengths in the winter in Fairbank (Figure S2a), leading to a 3-fold overestimate of $j_{O3 \rightarrow O(1D)}$ in winter (Figure S2b). This overestimate has minimal impact on $j_{HONO \rightarrow \bullet OH}$ or $j_{BrC \rightarrow 3C*}$ because these chromophores absorb most strongly at wavelengths greater than 325 nm (Figure S2c).

Section S10. Determination of monthly average concentrations of O_3, HONO, and BrC

Monthly average O_3 concentrations were determined by averaging the daily maximum 8-hour average O_3 reported by the Alaska DEC (Air Quality Monitoring Data, 2024), making the O_3 concentrations upper-bound estimates. HONO concentrations were estimated by first assuming the HONO-to-NO_2 ratio of 2.02(±0.05)% measured during ALPACA applies year-round (Kuhn et al., in preparation; Simpson et al., 2024). Next, the monthly NO_2 concentration was determined by averaging the daily peak 1-hour NO_2 concentrations reported by ADEC (Air Quality Monitoring Data, 2024), making the HONO concentration an upper-bound estimate. We do not account for changes in HONO sources throughout the year, which likely changes the HONO-to-NO_2 ratio, but our estimate provides a reasonable upper-bound estimate of HONO (Kim et al., 2014).

For estimating particulate brown carbon concentrations, we first calculated the monthly average $PM_{2.5}$ concentration at the CTC site using daily average $PM_{2.5}$ concentrations reported by AKDEC (Air Quality Monitoring Data, 2024). Next, we assumed 52% of the total $PM_{2.5}$ is OA, the annual average OA-to-$PM_{2.5}$ fraction for Fairbanks reported by Kotchenruther (2016). This results in OA concentrations similar to the water-soluble DOC we measured in our filter extracts in Fairbanks during January and February of 2022 (Figure 4). During the summer, $PM_{2.5}$ and OA concentrations are highly variable due to the influence of wildfire smoke: the summer of 2021 (depicted in Figure 9b) was only moderately impacted by wildfire smoke, while summers with severe wildfire smoke have much larger OA and BrC concentrations. Once the monthly average OA concentration was determined, we used the average MAC_λ from water-soluble organic carbon measured with the House site samples to calculate $j_{BrC \rightarrow 3C*}$. We do not determine the fraction of OA that is light-absorbing BrC, but instead we determine the light absorbance by the BrC within the entire OA population using the OA-averaged MAC values.

Table S1. Sample collection dates and times for 2022 ALPACA campaign

Composite Name [a]	House Site:		CTC Site:	
	Composite Filter Sample Collection [e]		*Composite Filter Sample Collection* [e]	
	Start	End	Start	End
1/15 [b]	1/13 17:10	1/17 09:41	N/A	N/A
1/21	1/17 10:00	1/25 09:30	1/17 13:59	1/25 08:52
1/27	1/26 10:00	1/28 09:30	1/26 10:20	1/28 09:06
1/31 [c]	1/29 10:00	2/3 09:30	1/29 09:31	2/3 09:00
2/4	2/3 10:00	2/6 09:30	2/3 09:46	2/6 09:04
2/7	2/6 10:00	2/8 09:30	2/6 09:38	2/8 08:59
2/14	2/8 10:00	2/21 09:30	2/8 09:30	2/21 09:05
2/22	2/21 10:00	2/23 09:30	2/21 09:33	2/23 09:05
2/24	2/23 10:00	2/26 09:30	2/23 09:45	2/26 08:41
Field Blank [d]	*House Field Blank Composite*		*CTC Field Blank Composite*	
	1/18 09:00 (30 second collection)		2/9 09:34	2/9 09:37
	1/25 09:00 (30 second collection)		2/20 09:29	2/20 09:31

[a] Composites are named by the midpoint date of the sampling period. Start and end times are in 24-hr format.

[b] The House site contains a 45.5-hour filter sample between 1/14 12:40 and 1/16 10:16 that was included in the 1/15 composite. When this filter was extracted into water, it had higher solute concentrations purely based on having a longer filter collection time compared to the 24-hour samples: the 1/15 composite was a 4-day composite but was only extracted into the volume of solvent equivalent to 3-day composite, leading to a 0.75 concentration factor difference. The data reported throughout the manuscript for the 1/15 sample is corrected for the high solute concentrations due to the longer sampling time. In the SI, each table with relevant data from the 1/15 sample indicates whether the data has been corrected for this.

[c] Between 1/30 and 2/3, we collected separate day and night filter samples at the CTC site, covering 7 and 17 hours, respectively.

[d] Field blanks were prepared for each site by compositing the corresponding two field blank filter samples.

[e] Each filter composite is composed of several 24-hour filters combined to create a multiday composite.

Table S2. pH values of particle extracts.

Site	Sample		pH	
			Extraction Solution [a]	PM Extract [b]
House	1/15		1.3	0.87
	1/21		1.3	1.23
	1/27		5.6	4.39 [c]
	1/31		1.3	1.28
	2/4		1.3	1.10
	2/7		1.3	0.88
	2/14		1.3	1.22
	2/22		1.3	1.10
	2/24		1.3	1.15
	Field Blank		1.3	1.31
CTC	1/21		1.3	1.26
	2/7		1.3	1.22
	1/21		5.0	5.11
	2/22		5.0	5.04 [d]
	2/24		5.0	4.82 [e]
	2/14 [f]	10.0	1.3	1.01
		2.0	1.3	1.02
		0.70	1.3	1.01
		0.40	1.7 [g]	1.08
		0.30	1.8 [g]	1.13
	Field Blank		5.0	4.90 [h]

[a] This is the pH of the H_2SO_4 solution (generally either 5×10^{-2} or 1×10^{-5} M) that was used to extract the $PM_{2.5}$ filters.

[b] This is the pH of the particle extract, which was used for photochemical experiments.

[c] The pH after extraction was 6.73, which was adjusted to 4.39 with 75 µL of 10 mM H_2SO_4.

[d] The pH after extraction was 5.82, which was adjusted to 5.04 with 53 µL of 10 mM H_2SO_4.

[e] The pH after extraction was 5.39, which was adjusted to 4.82 with 20 µL of 10 mM H_2SO_4 and 13 µL of 10 mM NaOH.

[f] A series of dilutions were made for this sample, where different volumes of H_2SO_4 solution were used to extract each filter square. The numbers on the different rows for this sample (10.0, 2.0, 0.70, etc.) represent the volume of solution (in mL) used for a given dilution. The solution volume used for the other samples was 1.0 mL.

[g] After using rotary evaporation to remove water, the pH of the 0.4x and 0.3x solutions are both expected to be 1.3.

[h] The pH after extraction was 6.81, which was adjusted to 4.90 with 85 µL of 10 mM H_2SO_4.

Table S3. Chemical probes (P) and their rate constants with oxidants (k_{P+Ox})

Probe		$k_{P+\bullet OH}$ (M^{-1} s^{-1})	k_{P+1O2*} (M^{-1} s^{-1})	k_{P+3C*} (M^{-1} s^{-1})
Benzoic Acid [a]	pH 1	4.30×10^{9}	-	-
	pH 5	5.69×10^{9}		
Furfuryl Alcohol		1.50×10^{10} [b]	8.06×10^{7} [c]	-
Syringol (SYR) [d]	pH 1	$1.5(\pm0.7)\times10^{10}$	$3.6(\pm0.7)\times10^{7}$	$6.7(\pm1.5)\times10^{9}$ [e]
	pH 5	$2.0(\pm0.4)\times10^{10}$		

[a] At pH 1, where there is no significant dissociation of benzoic acid into benzoate, the rate constant is equal to the value for benzoic acid (4.3×10^{9} M^{-1} s^{-1}; Anastasio and McGregor, 2001; Ashton et al., 1995; Wander et al., 1968). At pH 5 where only 13.4% of benzoic acid/benzoate is protonated, the rate constant is a mole-fraction-weighted rate constant for the reaction of •OH with benzoate (5.9×10^{9} M^{-1} s^{-1}; Anastasio and McGregor, 2001) and benzoic acid. The resulting a mole-fraction-weighted rate constant is 5.69×10^{9} M^{-1} s^{-1}.

[b] The rate constant of FFA with •OH was reported by (Ross and Ross, 1977).

[c] Furfuryl alcohol rate constant is temperature-corrected to 10 °C (Appiani et al., 2017). Other rate constants listed in the table are not adjusted for temperature.

[d] $k_{SYR+\bullet OH}$ and $k_{SYR+3C*}$ were measured at pH 2. We use the pH 2 •OH values for our pH 1 solutions and use the pH 2 rate constants for both pH 1 and pH 5 experiments (Ma et al., 2022; Smith et al., 2015).

[e] Smith et al. (2015) measured $k_{SYR+3C*}$ using triplet 3,4-dimethoxybenzaldehyde (^{3}DMB*) at pH 2 and 5 and found notable differences in k_{P+3C*}: $6.7(\pm1.5)\times10^{9}$ at pH 2 and $3.5(\pm0.8)\times10^{9}$ M^{-1} s^{-1} at pH 5. The pH dependence is because the p*K*a of 3,4-DMB is 3.3, suggesting the pH dependence is specific to the triplet state of 3,4-DMB and therefore should not be applied to the entire pool of ^{3}C* measured by syringol. We assume the k_{P+3C*} at both pH 1 and pH 5 is equivalent to $6.7(\pm1.5)\times10^{9}$ M^{-1} s^{-1}, the rate constant measured by Smith et al. (2015) at pH 2.

Table S4. Parameters for calculating mass transport of •OH(g) to particles and drops: Part I

Water Content [a]	Aerosol Liquid Water Conditions	Cloud/Fog Drop Conditions
PM-mass/H_2O-mass ratio (μg-PM/μg-H_2O)	1	6×10^{-5}
Particle/Drop Diameter (μm)	0.7	14
Particle/Drop Volume (cm^3)	1.8×10^{-13}	1.4×10^{-9}
assume $C_s = 0$ [b]		
Mass Accommodation Coefficient	1	
•OH(g) (mlc cm^{-3})	3.0×10^5	

[a] The water content of particles qualitatively names the condition quantitatively defined by the PM-mass/H_2O-mass ratio, i.e., the mass of a dry particle relative to the mass of liquid water.

[b] Assuming the concentration of •OH at the surface of the particle (C_s) is 0 makes our calculated $P_{\bullet OH,MT}$ an upper-bound estimate.

Table S5. Parameters for calculating mass transport of •OH(g) to particles and drops: Part II [a]

Sample	Gas-Phase Diffusion Coefficient ($cm^2\ s^{-1}$)	Mean Molecular Speed ($cm\ s^{-1}$)	Mean Free Path (cm) (assumes zero kinetic order theory)
1/15	0.20	5.62×10^4	1.1×10^{-5}
1/21	0.19	5.59×10^4	1.0×10^{-5}
1/27	0.19	5.60×10^4	1.0×10^{-5}
1/31	0.18	5.49×10^4	9.9×10^{-5}
2/4	0.20	5.64×10^4	1.1×10^{-5}
2/7	0.20	5.61×10^4	1.0×10^{-5}
2/14	0.20	5.62×10^4	1.1×10^{-5}
2/22	0.21	5.76×10^4	1.1×10^{-5}
2/24	0.22	5.78×10^4	1.1×10^{-5}

[a] Equations are from Seinfeld & Pandis (2016).

Table S6. Parameters for calculating mass transport of •OH(g) to particles and drops: Part III [a]

Sample	Aerosol Liquid Water Conditions [b]					Cloud/Fog Drop Conditions [b]				
	Knudsen Number (Kn)	Fuch's Transition Regime Correction Factor	Continuum Flux (mlc drop^{-1} s^{-1})	Transition Flux (mlc drop^{-1} s^{-1})	$P_{\bullet OH,MT}$ (M s^{-1})	Knudsen Number (Kn)	Fuch's Transition Regime Correction Factor	Continuum Flux (mlc drop^{-1} s^{-1})	Transition Flux (mlc drop^{-1} s^{-1})	$P_{\bullet OH,MT}$ (M s^{-1})
1/15	0.30	0.80	26	21	1.9×10^{-7}	1.50×10^{-2}	0.989	520	514	5.9×10^{-10}
1/21	0.30	0.80	25	20	1.9×10^{-7}	1.48×10^{-2}	0.989	510	504	5.8×10^{-10}
1/27	0.30	0.80	26	20	1.9×10^{-7}	1.49×10^{-2}	0.989	513	508	5.9×10^{-10}
1/31	0.28	0.81	24	19	1.8×10^{-7}	1.42×10^{-2}	0.990	479	474	5.5×10^{-10}
2/4	0.30	0.79	26	21	1.9×10^{-7}	1.52×10^{-2}	0.989	527	521	6.0×10^{-10}
2/7	0.30	0.80	26	21	1.9×10^{-7}	1.50×10^{-2}	0.989	517	511	5.9×10^{-10}
2/14	0.30	0.80	26	21	1.9×10^{-7}	1.50×10^{-2}	0.989	520	514	5.9×10^{-10}
2/22	0.32	0.78	28	22	2.1×10^{-7}	1.60×10^{-2}	0.989	567	560	6.5×10^{-10}
2/24	0.32	0.78	29	22	2.1×10^{-7}	1.61×10^{-2}	0.989	574	567	6.6×10^{-10}

[a] Equations are from Seinfeld & Pandis (2016). $P_{\bullet OH,MT}$ is the rate of •OH(g) partitioning to the particles/drops, expressed in terms of the aqueous volume, i.e., mol-•OH L^{-1}-solution s^{-1}.

[b] The water content of particles qualitatively names the condition quantitatively defined by the PM-mass/H_2O-mass ratio, i.e., the mass of dry particle solutes relative to the mass of liquid water. Cloud/fog droplets have a higher liquid water content and larger particle diameters than aerosol particles (Table S4). Particle diameter is especially important for mass transport because $P_{\bullet OH,MT}$ (expressed in terms of liquid volume) decreases with increasing particle diameter, meaning aerosol liquid water has much higher $P_{\bullet OH,MT}$ compared to cloud/fog drop conditions.

Table S7. Characterization of sample composite periods: average $PM_{2.5}$, temperature, relative humidity, and actinic flux

Composite	$PM_{2.5}$ [a] ($\mu g\ m^{-3}$)	Average Temp.[b] (°C)	Relative Humidity [c] (%)	Albedo (fraction) [d]	Downwelling $I_{\lambda,310\text{-}550\ nm}$ [e] (photon $cm^{-2}\ s^{-1}$)	
					Solar Noon	Midday Three-Hour Average
1/15	7.5	-19	N/A	N/A	N/A	N/A
1/21	12.0	-22	86	0.82	1.0×10^{16}	7.2×10^{15}
1/27	17.7	-21	77	0.81	1.7×10^{16}	1.2×10^{16}
1/31	26.1	-31	75	0.72	3.2×10^{16}	2.3×10^{16}
2/4	8.6	-18	80	0.85	1.0×10^{16}	8.7×10^{15}
2/7	4.3	-20	77	0.90	1.3×10^{16}	1.1×10^{16}
2/14	7.2	-20	80	0.87	2.7×10^{16}	2.0×10^{16}
2/22	3.6	-7	90	0.96	1.4×10^{16}	1.1×10^{16}
2/24	12.5	-5	90	0.85	3.5×10^{16}	2.9×10^{16}

[a] $PM_{2.5}$ measured at the NCore site by the Alaska Department of Environmental conservation. Data is available at https://www.epa.gov/outdoor-air-quality-data/download-daily-data.

[b] Temperature measured at the CTC site. Data is available at https://arcticdata.io/catalog/portals/ALPACA/Data.

[c] Relative Humidity reported at Airport Road by Environmental Research Division's Data Access Program (ERDDAP). Data is available at https://erddap.sensors.ioos.us/erddap/tabledap/alaska-dot-rwis-255.html.

[d] Surface albedo determined using the ratio of the upwelling j_{NO2} to the downwelling j_{NO2} determined at the NCore site.

[e] Downwelling actinic fluxes measured using the Diode-Array Actinic Flux Spectroradiometer at the NCore site in downtown Fairbanks (Simpson et al., 2024). The "Solar Noon" column reflects daily I_λ measured at 13:30, around solar noon, averaged over a given composite. The "Downwelling Midday Three-Hour Average" column reflects the daily I_λ averaged between 12:00 and 15:00 – the peak three hours of sunlight, then again averaged over each day in each composite. We converted the downwelling actinic flux to the total (downwelling and upwelling) flux by multiplying it by the sum of (1 + albedo).

Table S8. Parameters used in TUV to model actinic fluxes during ALPACA

Latitude		64.840
Longitude		-147.720
Overhead Column Ozone (du) [a]		300
Surface Albedo (fraction)		0.85
Ground Elevation (km above sea level)		0.15
Measurement Altitude (km above sea level)		0.16
Clouds [a]	Optical Depth	0
	Base	4
	Top	5
Aerosols [a]	Optical Depth	0.235
	S-S Albedo	0.99
	Alpha	1

[a] Standard input parameters in the TUV model; these are not specific to Fairbanks.

Table S9. Characterization of water-soluble brown carbon in PM extracts (PME)

Site	Sample		PM-Mass/H_2O-Mass Ratio ($\mu g\ \mu g^{-1}$) [a]	$[DOC]_{PME}$ (mM)	MAC_{300} (m^2 g-C^{-1}) [b]	MAC_{365} (m^2 g-C^{-1}) [b]	AAE [c]	E2/E3 [d]
House	1/15, pH 1 [e]		$2.8(\pm0.2)\times10^{-4}$	2.8(±0.2)	3.75	1.01	9.4	6.4
	1/21, pH 1		$2.6(\pm0.1)\times10^{-4}$	3.0(±0.2)	3.31	0.863	9.1	6.5
	1/27, pH 4.5		$3.0(\pm0.6)\times10^{-4}$	3.18(±0.06)	3.78	1.05	8.2	6.4
	1/31, pH 1		$3.2(\pm0.1)\times10^{-4}$	4.90(±0.06)	4.04	0.964	8.8	7.1
	2/4, pH 1		$1.7(\pm0.3)\times10^{-4}$	1.7(±0.2)	4.61	1.07	9.3	7.4
	2/7, pH 1		$4.7(\pm0.1)\times10^{-4}$	1.84(±0.02)	2.66	0.583	10.2	8.0
	2/14, pH 1		$1.9(\pm0.6)\times10^{-4}$	2.22(±0.04)	3.20	0.768	9.4	7.3
	2/22, pH 1		$1.8(\pm0.2)\times10^{-4}$	2.24(±0.09)	1.88	0.402	10.2	7.9
	2/24, pH 1		$3.3(\pm0.4)\times10^{-4}$	3.0(±0.1)	2.65	0.680	9.4	6.8
	Field Blank, pH 1		$1.2(\pm0.2)\times10^{-4}$	0.23(±0.01)	0.246	0	N/A	
CTC	1/21, pH 1		$2.1(\pm0.1)\times10^{-4}$	2.70(±0.06)	3.41	0.999	8.3	6.4
	1/21, pH 5		$2.1(\pm0.1)\times10^{-4}$	2.70(±0.02)	3.55	1.10	9.1	7.0
	2/7, pH 1		$1.8(\pm0.1)\times10^{-4}$	1.86(±0.03)	2.16	0.577	7.3	5.8
	2/22, pH 5		$2.2(\pm0.4)\times10^{-4}$	2.15(±0.03)	2.12	0.611	7.7	6.7
	2/24, pH 5		$2.1(\pm0.1)\times10^{-4}$	2.99(±0.06)	2.44	0.757	7.2	6.2
	2/14, pH 1 [f]	10	$1.79(\pm0.04)\times10^{-5}$	0.227(±0.003)	3.21	0.837	8.7	7.3
		2.0	$8.9(\pm0.2)\times10^{-5}$	1.15(±0.01)	3.13	0.831	8.9	7.1
		0.70	$2.55(\pm0.04)\times10^{-4}$	2.96(±0.01)	3.65	1.00	8.9	6.7
		0.40	$4.46(\pm0.09)\times10^{-4}$	5.14(±0.06)	3.20	0.926	8.6	6.3
		0.30	$6.0(\pm0.1)\times10^{-4}$	6.55(±0.04)	3.18	0.966	7.9	6.0
	Field Blank, pH 5		$1.7(\pm0.3)\times10^{-4}$	0.122(±0.002)	0.878	0.328	N/A	

[a] PM-mass/H_2O-mass ratio reflects the concentration of a given extract, expressed as the ratio of dry PM mass extracted from a filter to the amount of liquid water in the extract. The extracted PM mass was measured from filters extracted into Milli-Q water, and therefore we list the same PM Mass/H_2O Mass ratio for the two extracts of the CTC 1/21 composite prepared separately at pH 1.3 and pH 5. The blank filters have non-zero PM-mass/H_2O-mass ratios because part of the filter degrades upon extraction.

[b] MAC_λ values are calculated using the absorbance and DOC concentrations measured in the PM extracts. MAC_λ values reported above use the DOC concentrations measured in the extracts, blank corrected for field blank DOC (reported for the two sites above). This assumes that the minor DOC contamination has minimal impact on the measured absorbance of extracts, a fair assumption because the background DOC concentrations are low (< 10% of the measured DOC concentration) and the MAC_λ of the blanks are lower than the field samples.

[c] AAE is the absorption Angstrom exponent, calculated between 300 and 450 nm.

[d] E2/E3 is the ratio of BrC absorbance at 250 nm to that at 365 nm (Helms et al., 2008; Peuravuori and Pihlaja, 1997).

[e] Note that the 1/15 composite was a 4-day composite but was only extracted into the volume of solvent equivalent to 3-day composite, as it used a filter sample collected for 45.5 hours instead of the standard 24-hours. The DOC concentration shown here was measured directly in the extract and not corrected for the 75% dilution factor, which needs to be used to compare the PM-Mass/H_2O-Mass Ratio and DOC concentration in the 1/15 composite to the all other composites. The

DOC concentration in ALW corrects for this difference in the calculation for DOC in ALW, which accounts for variability in the air volume collected on each filter, as described in section S6.

[f] For the CTC 2/14 dilution series, the PM-mass/H_2O-mass ratio was only determined for the 0.70 dilution sample, the PM-mass/H_2O-mass ratio values for the 10, 2.0, 0.40, and 0.30 dilutions were calculated by extrapolation. See Table S2 for a description of this dilution series. The DOC concentrations and absorbance parameters were measured for each dilution.

Table S10. Solar simulator experimental data I: *p*-HBA formation and first-order rate constants for probe loss

Site	Sample		Rate of *p*-HBA Production (μM min^{-1}) [b]	Experimental Probe Loss (j_{2NB} = 0.0045 s^{-1}) [a]		
				$k'_{EXP,BA}$ (s^{-1}) [b]	$k'_{EXP,FFA}$ (s^{-1})	$k'_{EXP,SYR}$ (s^{-1})
House	1/15, pH 1 [c]		2.2(±0.2)×10^{-3}	8.8(±0.7)×10^{-6}	1.2(±0.2)×10^{-4}	9.2(±1.1)×10^{-4}
	1/21, pH 1		1.0(±0.1)×10^{-3}	7.9(±0.7)×10^{-6}	1.3(±0.05)×10^{-4}	1.2(±0.05)×10^{-3}
	1/27, pH 4.5		6.1(±0.1)×10^{-3}	2.7(±0.2)×10^{-6}	1.2(±0.05)×10^{-4}	1.5(±0.07)×10^{-4}
	1/31, pH 1		3.2(±0.1)×10^{-3}	7.7(±0.5)×10^{-6}	1.4(±0.07)×10^{-4}	9.2(±0.5)×10^{-4}
	2/4, pH 1		1.2(±0.2)×10^{-3}	6.5(±1.1)×10^{-6}	1.4(±0.9)×10^{-3}	3.8(±0.2)×10^{-4}
	2/7, pH 1		6.3(±0.9)×10^{-4}	3.3(±0.2)×10^{-6}	8.6(±0.2)×10^{-5}	7.9(±0.7)×10^{-4}
	2/14, pH 1		3.2(±0.2)×10^{-3}	1.8(±0.09)×10^{-5}	1.1(±0.09)×10^{-4}	9.2(±0.5)×10^{-4}
	2/22, pH 1		1.1(±0.1)×10^{-3}	5.0(±0.5)×10^{-6}	8.3(±0.5)×10^{-5}	7.7(±0.5)×10^{-4}
	2/24, pH 1		7.4(±1.1)×10^{-4}	7.0(±0.5)×10^{-6}	1.2(±0.07)×10^{-4}	7.4(±0.5)×10^{-4}
	Field Blank, pH 1		1.2(±0.2)×10^{-4}	1.6(±0.09)×10^{-6}	1.1(±0.05)×10^{-5}	9.2(±1.4)×10^{-6}
CTC	1/21, pH 1		8.3(±1.6)×10^{-4}	7.9(±0.2)×10^{-6}	2.6(±0.2)×10^{-5}	1.4(±0.07)×10^{-3}
	1/21, pH 5		3.2(±0.2)×10^{-4}	3.4(±0.09)×10^{-6}	1.4(±0.07)×10^{-4}	5.0(±0.2)×10^{-4}
	2/7, pH 1		5.9(±0.2)×10^{-4}	5.4(±0.2)×10^{-6}	1.3(±0.09)×10^{-4}	9.7(±0.5)×10^{-4}
	2/22, pH 5		1.8(±0.2)×10^{-4}	1.5(±0.2)×10^{-6}	8.1(±0.2)×10^{-5}	7.2(±0.9)×10^{-5}
	2/24, pH 5		2.0(±0.4)×10^{-4}	1.5(±0.1)×10^{-6}	9.5(±0.9)×10^{-5}	1.5(±0.09)×10^{-4}
	2/14, pH 1 [d]	10	2.1(±0.4)×10^{-4}	2.4(±0.1)×10^{-6}	2.9(±0.1)×10^{-5}	1.1(±0.07)×10^{-4}
		2.0	6.3(±0.7)×10^{-4}	4.7(±0.2)×10^{-6}	1.0(±0.07)×10^{-4}	3.1(±0.2)×10^{-4}
		0.70	4.5(±1.4)×10^{-4}	7.7(±0.5)×10^{-6}	2.5(±0.1)×10^{-4}	5.4(±0.5)×10^{-4}
		0.40	5.2(±0.9)×10^{-4}	5.6(±0.7)×10^{-6}	2.7(±0.2)×10^{-4}	5.0(±0.2)×10^{-4}
		0.30	7.2(±0.5)×10^{-4}	4.7(±0.5)×10^{-6}	2.0(±0.1)×10^{-4}	4.3(±0.2)×10^{-4}
	Field Blank, pH 5		4.5(±0.9)×10^{-5}	2.7(±1.6)×10^{-7}	1.4(±0.5)×10^{-6}	0.9(±1.8)×10^{-6}

[a] The *k*' for experimental probe loss is the pseudo-first order rate constant for probe loss observed from every experiment where 1 mL of PME was spiked with 10 μM of each probe and illuminated in our solar simulator. These values are normalized to a single j_{2NB} value to account for variations in the intensity of the lamp in the solar simulator between experiment days.

[b] The rate of *p*-HBA production and the loss of BA were both used to calculate [•OH]. The [•OH] reported here is the average of the [•OH] determined by both methods.

[c] Note that the 1/15 composite was a 4-day composite but was only extracted into the volume of solvent equivalent to 3-day composite, as it used a filter sample collected for 45.5 hours instead of the standard 24-hours. The values shown here were measured for the true DOC concentration in the extract and not corrected for the 75% dilution factor. We calculated the photooxidant concentrations in the 1/15 extract using the $k'_{EXP,P}$ reported here, which we then corrected for the higher solute concentrations using the trends observed in our dilution experiment: •OH concentrations are not dependent on solute concentrations, but $^3C^*$ and $^1O_2^*$ concentrations are. As such, we did not adjust the •OH concentration, but we did adjust the $^3C^*$ and $^1O_2^*$ concentrations by the ratio of the volume of solute used for the extraction to the volume that would have been used for the extraction is the 45.5-hour filter has been two 23.5 hour filters. The 1/15 composite was a 4-day composite but was only extracted into the volume of solvent equivalent to 3-day composite, the solute concentration

should be 75% of the 1/15 House site extract. As such, in our calculations, the $^3C^*$ and $^1O_2^*$ concentrations were multiplied by 0.75 to reflect this so that the concentrations shown in Figures 5 and 7 account for this.[d] See Table S2 for a description of this dilution series.

Table S11. Solar simulator experimental data II: Rate of light absorbance, screening factor, and inhibition factor

Site	Sample		$R_{abs,EXP,PME}$ (mol L^{-1} s^{-1}) [a]	Screening Factor (300 - 500 nm, unitless) [b]	Inhibition Factor (*IF*, unitless)		
					FFA [c]	SYR (uncorrected)	SYR_{corr} (corrected) [d]
House	1/15, pH 1 [e]		8.0×10^{-6}	0.93	0.57(±0.093)	0.21(±0.075)	0.38(±0.15)
	1/21, pH 1		7.9×10^{-6}	0.94	0.78(±0.065)	0.84(±0.11)	1
	1/27, pH 4.5		1.1×10^{-5}	0.93	0.35(±0.034)	0.063(±0.0080)	0.18(±0.028)
	1/31, pH 1		1.6×10^{-5}	0.89	1.5(±0.14)	0.20(±0.040)	
	2/4, pH 1		5.3×10^{-6}	0.96	0.36(±0.034)	0.23(±0.039)	0.64(±0.13)
	2/7, pH 1		2.9×10^{-6}	0.97	0.99(±0.11)	0.93(±0.21)	0.94(±0.23)
	2/14, pH 1		4.9×10^{-6}	0.96	0.59(±0.057)	1.1(±0.13)	1
	2/22, pH 1		2.5×10^{-6}	0.97	0.98(±0.55)	1.3(±0.12)	1
	2/24, pH 1		4.7×10^{-6}	0.95	0.68(±0.046)	0.64(±0.080)	0.94(±0.13)
	Field Blank, pH 1		1.0×10^{-7}	1.00	0.70(±0.060)	0.95(±0.058)	1
CTC	1/21, pH 1		9.0×10^{-6}	0.86	0.67(±0.055)	0.99(±0.17)	1
	1/21, pH 5		1.1×10^{-5}	0.87	0.53(±0.070)	0.14(±0.047)	0.26(±0.090)
	2/7, pH 1		1.1×10^{-6}	0.84	0.59(±0.050)	1.1(±0.10)	1
	2/22, pH 5		4.9×10^{-6}	0.87	0.76(±0.045)	0.018(±0.0050)	0.024(±0.0070)
	2/24, pH 5		9.5×10^{-6}	0.88	0.63(±0.065)	0.033(±0.016)	0.053(±0.026)
	2/14, pH 1 [f]	10	6.4×10^{-7}	1.00	0.78(±0.049)	0.54(±0.050)	0.69(±0.078)
		2.0	3.2×10^{-6}	0.98	0.59(±0.044)	0.29(±0.037)	0.49(±0.072)
		0.70	9.8×10^{-6}	0.93	0.35(±0.024)	0.064(±0.030)	0.18(±0.088)
		0.40	1.6×10^{-5}	0.89	nd [g]		0.090
		0.30	2.5×10^{-5}	0.88	1.2(±0.10)	0.066(±0.026)	
	Field Blank, pH 5		2.7×10^{-7}	1.00	0.95(±0.30)	1.2(±0.14)	1

[a] $R_{abs,EXP,PME}$ is the rate of light absorbance in the PM extract in the solar simulator, summed between 300 and 550 nm. Values were calculated for a photon flux condition of $j_{2NB} = 0.0045$ s^{-1}, the calculated rate constant for 2NB photolysis on midday of February 1st in Fairbanks under clear sky conditions.

[b] Screening factor calculation explained in Section S2.

[c] When IF_{FFA} is greater than 1, we assume there is no suppression of [^{3}C*] due to quenching by DOC and therefore IF_{FFA} is equal to 1, meaning $IF_{SYR,corr}$ is equal to IF_{SYR} (Ma et al., 2023).

[d] When IF_{SYR} is greater than IF_{FFA}, we assume no inhibition of SYR occurs and set $IF_{SYR,corr}$ equal to 1 (Ma et al., 2023).

[e] Note that the 1/15 composite was a 4-day composite but was only extracted into the volume of solvent equivalent to 3-day composite, as it used a filter sample collected for 45.5 hours instead of the standard 24-hours. The rate of light absorbance in PME shown here was calculated for the true DOC concentration in the extract and not corrected for the 75% dilution factor, which needs to be used to compare the rate of light absorbance in PME for the 1/15 composite to the rate of light absorbance in PME in all other composites.[f] See Table S2 for a description of this dilution series.

[g] Due to limited available sample volume, *IF* values were not measured for the CTC 2/14 0.40 dilution series sample. Instead, this *IF* value was estimated for this sample using the linear relationship between $1/IF_{SYR,corr}$ and $[DOC]_{PME}$ from the other solutions (Ma et al., 2023).

Table S12. Exploring sources of •OH in PM extracts

Site	Sample	$P_{\bullet OH,EXP,PME}$ (M s^{-1}) [a]	NO_2^- (μM)	NO_3^- (μM)	$P_{\bullet OH,NO2-}$ (M s^{-1}) [a,b]	$P_{\bullet OH,NO3-}$ (M s^{-1}) [a,b]	P_{HOOH} (M s^{-1}) [a]
House	1/15, pH 1 [c]	3.8×10^{-9}	0	272	0	2.4×10^{-11}	6.9×10^{-9}
	1/21, pH 1	2.5×10^{-9}	0	268	0	2.4×10^{-11}	8.3×10^{-9}
	1/27, pH 4.5	1.0×10^{-9}	0	437	0	3.9×10^{-11}	3.6×10^{-9}
	1/31, pH 1	9.3×10^{-9}	0	291	0	2.6×10^{-11}	2.2×10^{-8}
	2/4, pH 1	1.4×10^{-9}	0	170	0	1.5×10^{-11}	4.9×10^{-9}
	2/7, pH 1	7.7×10^{-10}	0	84	0	7.6×10^{-12}	4.1×10^{-9}
	2/14, pH 1	1.6×10^{-9}	0	163	0	1.5×10^{-11}	5.7×10^{-9}
	2/22, pH 1	1.7×10^{-9}	0	145	0	1.3×10^{-11}	2.5×10^{-9}
	2/24, pH 1	2.0×10^{-9}	1	276	1.7×10^{-11}	2.5×10^{-11}	4.8×10^{-9}

[a] All rates shown here are normalized to $j_{2NB,AK} = 0.0045\ s^{-1}$ conditions. $P_{\bullet OH,EXP,PME}$ is the estimated rate of •OH formation in the extract, calculated from the measured [•OH] (equation S6). $P_{\bullet OH,NO2-}$ and $P_{\bullet OH,NO3-}$ are the rates of •OH formation from the direct photolysis of nitrite and nitrate, respectively, in the extract and P_{HOOH} is the production rate of HOOH determined in each extract (Sunday et al., 2024).

[b] $j_{NO3-\rightarrow\bullet OH}$ ($1.4\times10^{-7}\ s^{-1}$) and $j_{NO2-\rightarrow\bullet OH}$ ($2.6\times10^{-5}\ s^{-1}$) are rate constants reported by Anastasio & McGregor (2001) for our solar simulator, normalized to Davis midday winter solstice sunlight, where $j_{2NB} = 0.007\ s^{-1}$. Here, we adjusted the rate constants for •OH formation from nitrate and nitrite to Fairbanks conditions on February 1st ($j_{2NB,AK} = 0.0045\ s^{-1}$), i.e., $j_{NO3-\rightarrow\bullet OH} = 9.0\times10^{-8}\ s^{-1}$ and $j_{NO2-\rightarrow\bullet OH} = 1.7\times10^{-5}\ s^{-1}$.

[c] Note that the 1/15 composite was a 4-day composite but was only extracted into the volume of solvent equivalent to 3-day composite, as it used a filter sample collected for 45.5 hours instead of the standard 24-hours. The production rates and concentrations in PME shown here were calculated for the true DOC concentration in the extract and not corrected for the 75% dilution factor, which needs to be used to compare the 1/15 composite to other composites.

Table S13. Kinetic model for dilution series: Dominant loss pathways for oxidants [a]

Sample: CTC 2/14, pH 1	k' for •OH loss to DOC (s^{-1}) [b]	Percent of $^3C^*$ loss [c]		Percent of $^1O_2^*$ loss	
		to DOC	to O_2	to DOC	to H_2O
PME 10	7.9×10^4	2	98	0.01	99.99
PME 2.0	4.1×10^5	9	91	0.04	99.96
PME 0.70	1.1×10^6	20	80	0.10	99.90
PME 0.40	1.8×10^6	31	69	0.17	99.83
PME 0.30	2.3×10^6	36	64	0.22	99.78
Extrapolation to ALW	8.6×10^9	99.95	0.05	89	11

[a] Dilution series was performed on the CTC 2/14 pH 1 composite. See Table S2 for more information about the dilution series.

[b] First-order rate constant for OH loss due to reaction with DOC, estimated as the product of the measured DOC concentration and the second-order rate constant for DOC + •OH, $3.8(\pm1.9)\times10^8$ L mol-C^{-1} s^{-1}, from Arakaki et al. (2013).

[c] Rate constants for triplets reacting with DOC and dissolved oxygen are in Section S4. $[O_2]$ in Fairbanks particle water was determined using the temperature-adjusted Henry's Law constant (Sander, 2023) assuming solutions are air saturated. In laboratory conditions at 10 °C, $[O_2]$ was assumed to be 272 μM; this value was used for the dilution series calculations shown in the table. For ALW conditions predicted in Fairbanks and shown in the table, we used the average temperature for this sample (-20 °C; Table S7).

Table S14. Parameters for modelling photooxidant concentrations from PM extracts to aerosol liquid water conditions

Oxidant	Rate Constant	Value	Source
$^{\bullet}OH$	$k_{\bullet OH+DOC}$ (L mol^{-1}-C s^{-1})	3.8(±1.9)×10^{8}	(Arakaki et al., 2013)
$^1O_2$*	$k'_{1O2*+H2O}$ (s^{-1})	2.8(±0.02)×10^{5}	(Appiani et al., 2017)
	$k_{1O2*+DOC}$ (L mol^{-1}-C s^{-1})	1.0×10^{5}	(Ma et al., 2023)
^3C*	$k_{3C*+DOC,SYR}$ (L mol^{-1}-C s^{-1}) [a]	7.0×10^{7}	(Ma et al., 2024)
	$k_{3C*+DOC,FFA}$ (L mol^{-1}-C s^{-1}) [b]	1.0×10^{7}	(Ma et al., 2024)
	k_{3C*+O2} (M^{-1} s^{-1})	2.8×10^{9}	(Kaur et al., 2019)

[a] This rate constant for reactions of DOC with oxidizing ^3C* was measured by Ma et al. (2024) using syringol as a probe.
[b] This rate constant for the reaction of DOC with the entire pool of ^3C* was measured by Ma et al. (2024) using furfuryl alcohol as a probe for $^1O_2$*. Singlet oxygen is a proxy for the entire pool of ^3C* since every triplet should be able to produce $^1O_2$*, while only oxidizing triplets can react with syringol.

Table S15. Estimated aerosol liquid water characteristics: Rate of light absorbance, DOC, and concentration factor

Site	Sample	$R_{abs,AK,ALW}$ (mol L^{-1} s^{-1}) [a]	$[DOC]_{ALW}$ (M)	*CF*, or $[DOC]_{ALW}$ / $[DOC]_{PME}$ [b]
House	1/15, pH 1	3.0×10^{-2}	16(±1)	6.2×10^{3}
	1/21, pH 1	2.0×10^{-2}	17(±1)	6.0×10^{3}
	1/27, pH 4.5	4.3×10^{-2}	19.0(±0.4)	6.4×10^{3}
	1/31, pH 1	6.5×10^{-2}	21.1(±0.3)	4.5×10^{3}
	2/4, pH 1	4.9×10^{-2}	22(±2)	1.5×10^{4}
	2/7, pH 1	9.9×10^{-2}	62(±1)	3.9×10^{4}
	2/14, pH 1	7.3×10^{-2}	23.6(±0.5)	1.2×10^{4}
	2/22, pH 1	1.6×10^{-2}	15.2(±0.7)	7.6×10^{3}
	2/24, pH 1	2.4×10^{-2}	6.2(±0.2)	2.3×10^{3}
CTC	1/21, pH 1	1.7×10^{-2}	9.6(±0.3)	3.7×10^{3}
	1/21, pH 5	1.9×10^{-2}	9.6(±0.2)	3.7×10^{3}
	2/14, pH 1	8.7×10^{-2}	23.0(±0.1)	8.3×10^{3}
	2/7, pH 1	3.4×10^{-3}	47(±1)	2.7×10^{4}
	2/22, pH 5	1.8×10^{-2}	8.9(±0.2)	5.4×10^{3}
	2/24, pH 5	5.5×10^{-2}	4.8(±0.1)	1.7×10^{3}

[a] Rate of light absorbance in particle water under the midday Fairbanks sunlight measured for the middle day of each composite, $R_{abs,AK,ALW}$, calculated over the range of 300 to 550 nm.

[b] The ratio of DOC concentration in aerosol liquid water compared to that in the lab PM extract. This is the factor by which the PME concentration of a stable species (i.e., not a photooxidant) is multiplied by to estimate the ALW concentration. The ratio was determined as described in Section S6. For the dilution series sample (CTC 2/14), the *CF* is expressed based on the DOC concentration expected for a filter square extracted with the standard volume (1.0 mL) of solution, which was interpolated from the DOC values of the dilutions.

Table S16. Modelling photooxidant production in PME and ALW under Fairbanks actinic flux conditions

	Sample	$[O_2]_{ALW}$ (μM) [a]	•OH				$^3C^*$				$^1O_2^*$				
			$P_{•OH,MT}$ [b] ($M\ s^{-1}$)		k'_{DOC} [c] (s^{-1})		Loss of $^3C^*$ to DOC (%)		Loss of $^3C^*$ to O_2 (%)		$\Delta P_{1O2*}/\Delta DOC$ ($10^5\ s^{-1}$)	Loss of $^1O_2^*$ to DOC (%)		Loss of $^1O_2^*$ to H_2O (%)	
			PME ($\times10^{10}$)	ALW ($\times10^{7}$)	PME ($\times10^{-5}$)	ALW ($\times10^{-9}$)	PME	ALW	PME	ALW		PME	ALW	PME	ALW
House	1/15, pH 1	641	5.9	1.9	11	6	10	> 99	90	< 1	4.5	< 1	87	> 99	13
	1/21, pH 1	685	5.8	1.9	12	10	10		90		5.1		92		8
	1/27, pH 4.5	669	5.9	1.9	12	7	11		89		6.1		89		11
	1/31, pH 1	845	5.5	1.8	19	6	13		87		5.4		88		12
	2/4, pH 1	615	6.0	1.9	6.5	5	6		94		14		86		14
	2/7, pH 1	654	5.9	1.9	7.0	10	7		93		12		94		6
	2/14, pH 1	643	5.9	1.9	8.4	9	8		92		17		91		9
	2/22, pH 1	487	6.5	2.1	8.5	10	10		90		7.4		94		6
	2/24, pH 1	469	6.6	2.1	11	7	14		86		21		90		10
CTC	1/21, pH 1	685	5.8	1.9	10	5	9		91		9.3		87		13
	1/21, pH 5	685	5.8	1.9	10	5	9		91		7.4		87		13
	2/7, pH 1	654	5.9	1.9	7.1	10	7		93		18		93		7
	2/14, pH 1	643	5.9	1.9	11	8.7	10		90		27		78		9
	2/22, pH 5	487	6.5	2.1	8.2	7	10		90		9.7		90		10
	2/24, pH 5	469	6.6	2.1	11	6	14		86		3.1		87		13

[a] $[O_2]$ in ALW was estimated using the temperature-corrected Henry's Law constant (Sander, 2023) and the composite-average Fairbanks temperature listed in Table S1.

[b] Rate of mass transport of gas-phase •OH to ambient water drops (where PME conditions are equivalent to a cloud/fog drop) or particles (ALW conditions), calculated using the parameters described in Tables S4 – S6. PME and ALW values are multiplied by 10^{10} and 10^7, respectively, to make them easier to display in the table. For example, the House 1/15 rates are 5.9×10^{-10} and 1.9×10^{-7} M s^{-1} for PME (cloud/fog) and ALW conditions, respectively.

[c] Pseudo-first-order rate constant for •OH loss due to reaction with DOC. PME and ALW values are multiplied by 10^{-5} and 10^{-9}, respectively; e.g., the House 1/15 rate constants are 11×10^5 and 6×10^9 s^{-1} for PME (cloud/fog) and ALW conditions, respectively.

Table S17 (a) and (b). Lifetimes of organic compounds due to reactions with (a) $^3C^*$ and $^\bullet OH$ and (b) $^1O_2^*$ and $^\bullet OH$.

Compound	Rate Constant (M^{-1} s^{-1}) [a]		Lifetime of Compound [c]	
	$^3C^*$	$^\bullet OH$	$^3C^*$ (hrs)	$^\bullet OH$ (hrs)
Syringyl Acetone	4.5×10^9	1.4×10^{10}	0.074	9.1
Syringic Acid	3.2×10^9	9.4×10^9	0.10	14
Syringol	6.7×10^9	1.5×10^{10}	0.50	8.5
Guaiacyl Acetone	3.3×10^9	8.8×10^9	0.10	15
Guaicol	3.2×10^9	6.8×10^9	0.10	19
Ferulic Acid	3.4×10^9	1.3×10^{10}	0.098	9.8

Compound	Rate Constant (M^{-1} s^{-1}) [b]		Lifetime of Compound [c]	
	$^1O_2^*$	$^\bullet OH$	$^1O_2^*$ (hrs)	$^\bullet OH$ (hrs)
Benzimidazole	2.5×10^6	7.9×10^9	12	16
Imidazole	4.0×10^7	6.4×10^9	0.75	20
Indole	4.5×10^7	1.4×10^{10}	0.67	9.3
Vanillin	4.6×10^6 [d]	4.2×10^9 [e]	6.6	30
Syringol	3.6×10^7	1.5×10^{10} [f]	0.84	8.5
4-Nitrophenol	2.5×10^6	4.1×10^9	12.1	31
Histidine	7.0×10^7	4.8×10^9	0.43	27
Tyrosine	8.0×10^6	1.3×10^{10}	3.8	9.8
Tryptophan	3.4×10^7	1.3×10^{10}	0.89	9.8
Methionine	1.6×10^7	7.4×10^9	1.9	17
Cysteine	8.3×10^6	1.9×10^{10}	3.6	6.7
Resorcinol	2.0×10^7	5.8×10^9	1.5	22
Hydroquinone	2.5×10^7	1.1×10^{10}	1.2	12
Niclosamide	2.3×10^7	7.5×10^9	1.3	17

[a] Rate constants reported by Ma et al. (2021) and Arciva et al. (2022) were measured at pH 2 and at 20 °C.
[b] Rate constants reported by Manfrin et al. (2019) unless otherwise noted.
[c] Lifetimes were determined using the average peak three-hour photooxidant concentrations from all House site samples; $[^3C^*] = 8.4\times10^{-13}$ M; $[^1O_2^*] = 9.2\times10^{-12}$ M; $[^\bullet OH] = 2.2\times10^{-15}$ M.

[e] Manfrin et al. (2019) lists a $k_{vanillin+1O2*}$ of 3.6×10^5 M^{-1} s^{-1}, which was measured by Machado et al. (1997) in methanol and is an order of magnitude smaller than the 4.6×10^6 M^{-1} s^{-1} measured by Zhou et al., 2023) in water. We calculate the lifetime of vanillin with respect to $^1O_2$* using the Zhou et al. (2023) value reported in the table.

[e] Manfrin et al. (2019) use an estimated $k_{vanillin+\bullet OH}$ of 4×10^8 M^{-1} s^{-1}, which is 10 times smaller than the rate constant for vanillyl alcohol and $^\bullet$OH at pH 2 measured by Arciva et al. (2022). Here, use the measured $k_{vanillyl\ alcohol+\bullet OH}$ of 8.2×10^9 M^{-1} s^{-1} reported by Arciva et al. (2022) as a proxy for the rate constant of vanillin with $^\bullet$OH.

[f] Manfrin et al. (2019) reported a $k_{syringol+\bullet OH}$ of 5.8×10^{10} M^{-1} s^{-1}, which is roughly four times higher than the rate constant at pH 2 measured by Smith et al. (2015).

Table S18. Kinetics and assumptions used to model secondary SO_4^{2-} Formation. All oxidants and oxidation pathways are aqueous unless noted otherwise.

Oxidant	Reaction Kinetics	Description & Assumptions	Reference
$^3C^*$	$k_{3C^*+S(IV)} = 1.3\times10^8\ M^{-1}\ s^{-1}$	The rate constant listed here is assumed to be the same for all three inorganic S(IV) species: $SO_2{\cdot}H_2O$, HSO_3^-, and SO_3^{2-}. The rate constant was not adjusted for temperature. The $^3C^*$ activity coefficient is assumed to be 1.	(Wang et al., 2020)
HOOH	$P_{SO42-} = P_{HOOH}$ (S19)	The production rate of SO_4^{2-} from HOOH is equal to the production rate of HOOH in the range of [inorganic S(IV)] predicted for Fairbanks particles (Sunday et al., 2024). The production rate was not adjusted for temperature. The HOOH activity coefficient is assumed to be 1.	(Anastasio et al., 1997; Sunday et al., 2024)
O_3	$log\frac{P_{measured}}{P_{predicted,I=0}} = a\left(\frac{\sqrt{I}}{1+\sqrt{I}}\right) + bI$ (S20) a = 1.475(±0.004) b = 0.070(±0.001) kg mol^{-1} $P_{aq,O_3} = \frac{P_{measured}}{P_{predicted,I=0}}\left(k_0[SO_2\cdot H_2O] + k_1[HSO_3^-] + k_2[SO_3^{2-}]\right)$ (S21) $H_{O_3} = e^{\left(\frac{2297}{T} - 2.659\times I_s + 688\times\frac{I_s}{T} - 12.19\right)}$ (S22) $k_0 = 2.4\times10^4\ M^{-1}\ s^{-1}$ $k_1 = 3.7\times10^5\ M^{-1}\ s^{-1}$ $k_2 = 1.5\times10^9\ M^{-1}\ s^{-1}$	Equations were determined by fitting experimentally determined ratios of S(IV) oxidation rates, $\frac{P_{measured}}{P_{predicted,I=0}}$, with ionic strengths between 2 and 14 mol kg^{-1} (Yu et al., 2023). [O_3] was predicted with the Henry's Law constant adjusted for temperature and ionic strength. The correction for ionic strength of the Henry's Law constant for ozone was validated only until I_s = 0.6 M but is used here until I_s = 23 M. The rate constant was not adjusted for temperature.	(Yu et al., 2023)
TMI + O_2	pH ≤ 4.2 $P_{SO_4^{2-}} = k_3[H^+]^{-0.74}[S(IV)][Mn(II)][Fe(III)]$ (S23) $k_3 = 3.72\times10^7\times e^{(-8431.6\times(\frac{1}{T}-1/297))}M^{-2}s^{-1}$ (S24) pH > 4.2	The equation to correct the rate constants for ionic strength was determined for I_s ≤ 2 M. We assume this relationship holds for the entire range of ionic strengths predicted for our particles (maximum I_s = 23 M). The activity coefficients (γ_{Is}) of metal species were determined using the equations listed here.	(Ibusuki and Takeuchi, 1986)

	$P_{SO_4^{2-}} = k_4[\mathrm{H^+}]^{0.67}[\mathrm{S(IV)}][\mathrm{Mn(II)}][\mathrm{Fe(III)}]$ (S25) $k_4 = 2.51 \times 10^{13} \times \mathrm{e}^{(-8431.6\times(\frac{1}{\mathrm{T}}-1/297))}\mathrm{M}^{-2}\mathrm{s}^{-1}$ (S26) $log_{10}\left(\frac{k}{k^{I_S=0}}\right) = \frac{-3.02\sqrt{I_S}}{1+\sqrt{I_S}}$ (S27) For Mn(II): $log_{10}(\gamma_{Is}) = \frac{-z_i{}^2\times 0.5109\sqrt{I_S}}{1+1.5\times\sqrt{I_S}}$ (S28) For Fe(III), γ_{Is}= 0.001		(Martin & Hill, 1987) (Song et al., 2021)
Gas-phase •OH	$k(\mathrm{T}) = \left(\frac{\frac{k_0(\mathrm{T})[\mathrm{M}]}{1+\frac{k_0(\mathrm{T})[\mathrm{M}]}{k_\infty(\mathrm{T})}}\right)0.6^z$ (S29) $z = \left(1+\left[log_{10}\left(\frac{k_0(\mathrm{T})[\mathrm{M}]}{k_\infty(\mathrm{T})}\right)\right]^2\right)^{-1}$ (S30) $k_0(\mathrm{T}) = {k_0}^{300}\left(\frac{\mathrm{T}}{300}\right)^{-\mathrm{n}}$ (S31) $k_\infty(\mathrm{T}) = {k_\infty}^{300}\left(\frac{\mathrm{T}}{300}\right)^{-\mathrm{m}}$ (S32) [M] = concentration of N_2 and O_2 ${k_0}^{300} = 3.3\times10^{-31}$ cm^6 molecule^{-2} s^{-}1 n = 4.3 ${k_\infty}^{300} = 1.6\times10^{-12}$ cm^3 molecule^{-1} s^{-1} m = 0	[O_2] and [N_2] were determined assuming the ideal gas law applies and that O_2 and N_2 account for 21% and 78% of the gas molecules in the atmosphere.	(Cheng et al., 2016)
Aqueous-phase •OH	$k_{\bullet OH+HSO3^-} = 4.5\times10^9$ M^{-1} s^{-1} (at 298 °K)	Seinfeld & Pandis (2016) report a multistep mechanism with 14 different rate constants. Here, we make two assumptions. First, we assume HSO_3^- is the dominant inorganic S(IV) species and that its activity is equal to that of inorganic S(IV). Second, we assume the first step of the reaction is the rate-determining step, and therefore that $k_{\bullet OH+HSO3^-}$ defines the rate of SO_4^{2-} formation. The rate constant was not adjusted for temperature or ionic strength. The activity coefficient of •OH is assumed to be 1.	(Seinfeld & Pandis, 2016)

NO_2	$k_{NO2+S(IV)} = 1.4\times10^5$ M^{-1} s^{-1} (pH < 5) $P_{SO_4^{2-}} = k_{NO2+S(IV)}[S(IV)][NO_{2(aq)}]$ (S33) $log_{10}\left(\frac{k}{k^{I_S=0}}\right) = cI_s$ (S34) c = 0.01 $H_{NO_2}^{I_S=0} = 1.0\times10^{-2}\times e^{\left(2516.2\times\left(\frac{1}{T}-\frac{1}{298}\right)\right)}$ (S35)	While several values of $k_{NO2+S(IV)}$ have been reported across a range of pH values, the value at pH < 5 is disputed. The reaction of NO_2 with S(IV) is highly pH dependent, with higher pHs associated with faster reactions with rate constants an order of magnitude higher than the $k_{NO2+S(IV)}$ reported here. However, Tilgner et al. (2021) explain that the fast rate constants measured in dilute solution are not likely to be relevant in the briny, high ionic strengths characteristic of aerosol liquid water. They report $k_{NO2+HSO3-}$ of 13 M^{-1} s^{-1} and $k_{NO2+SO3-2}$ of 270 M^{-1} s^{-1}. Here, we use $k_{NO2+S(IV)}$ at pH < 5 for both the low and high pH regimes. The rate constant was not adjusted for temperature. The activity coefficient of NO_2 was assumed to be equal to the activity coefficient of S(IV).	(Lee & Schwartz, 1982) (Clifton et al., 1988) (Cheng et al., 2016) (Seinfeld & Pandis, 2016)
HONO	pH < 4 $R_{SO_4^{2-}} = k_5[H^+]^{0.5}[N(III)][S(IV)]$ (S36) k_5 = 143 $M^{-3/2}$ s^{-1} 3 < pH < 7 $R_{SO_4^{2-}} = k_6[H^+][N(III)][S(IV)]$ (S37) k_6 = 4800 M^{-2} s^{-1} $H_{HONO}^{I_S=0} = 49\times e^{\left(\left(\frac{-9.5}{1.987\times10^{-3}}\right)\times\left(\frac{1}{298.15}-\frac{1}{T}\right)\right)}$ (S38) $[N(III)] = [HONO] + [NO_2^-] = \frac{[HONO]}{\alpha_0}$ (S39) $\alpha_0 = \frac{1}{1+\frac{K_a}{[H^+]}}$ (S40)	[N(III)] is the total aqueous-phase concentration of HONO and NO_2^-, estimated using the temperature-corrected physical Henry's law constant converted to the effective constant using the mole fraction for nitrous acid (α_0). The rate constant was not adjusted for temperature or ionic strength. The activity coefficient of HONO was assumed to be equal to the activity coefficient of inorganic S(IV).	(Wang et al., 2020) (Seinfeld & Pandis, 2016)

545

Table S19. Composite-averaged, midday ALW oxidant concentrations and gas-phase concentrations used to model secondary sulfate formation

Oxidant [a]		Sample								
		1/15	1/21	1/27	1/31	2/4	2/7	2/14	2/22	2/24
$^{\bullet}OH_g$ (mlc cm^{-3}) [b]		3×10^{5}								
SO_2 (ppb)		7.8	11	12	20.	8.5	3.8	7.3	5.2	8.6
HONO (ppb)		N/A	0.62	0.76	0.91	0.45	0.24	0.37	0.31	N/A
O_3	(ppb)	9.0	6.0	5.0	0.9	15.0	20.0	13.0	18.0	4.0
	(M)	N/A	6×10^{-11}	9×10^{-10}	1×10^{-9}	3×10^{-9}	3×10^{-9}	1×10^{-9}	3×10^{-10}	6×10^{-11}
$^3C^*$ (M) [c]		9×10^{-13}	2×10^{-13}	2×10^{-13}	3×10^{-12}	6×10^{-13}	1×10^{-12}	1×10^{-12}	3×10^{-13}	3×10^{-13}
NO_2 (M)		N/A	8×10^{-10}	1×10^{-9}	3×10^{-9}	1×10^{-9}	7×10^{-10}	1×10^{-9}	6×10^{-10}	9×10^{-10}
N(III) (M)	pH 1	N/A	5×10^{-7}	5×10^{-7}	1×10^{-6}	2×10^{-7}	1×10^{-7}	2×10^{-7}	9×10^{-8}	N/A
	pH 5	N/A	7×10^{-5}	8×10^{-5}	2×10^{-4}	3×10^{-5}	2×10^{-5}	3×10^{-5}	1×10^{-5}	N/A
$^{\bullet}OH_{aq}$ (M) [d,e]	pH 1	2×10^{-15}	7×10^{-16}	4×10^{-16}	4×10^{-15}	8×10^{-16}	7×10^{-16}	2×10^{-16}	2×10^{-16}	3×10^{-16}
	pH 5	5×10^{-16}	2×10^{-16}	1×10^{-16}	1×10^{-15}	3×10^{-16}	2×10^{-16}	6×10^{-16}	5×10^{-16}	9×10^{-16}
Fe_{aq} {M} [f,g]	pH 1	N/A	5×10^{-5}	2×10^{-6}	5×10^{-5}	8×10^{-5}	5×10^{-5}	5×10^{-5}	1×10^{-5}	1×10^{-5}
	pH 5	N/A	7×10^{-6}	2×10^{-6}	1×10^{-5}	1×10^{-5}	3×10^{-6}	2×10^{-6}	3×10^{-7}	6×10^{-7}
Mn_{aq} {M} [f,h]	pH 1	N/A	1×10^{-4}	7×10^{-5}	1×10^{-4}	2×10^{-4}	2×10^{-4}	1×10^{-4}	6×10^{-5}	5×10^{-5}
	pH 5	N/A	9×10^{-5}	7×10^{-5}	9×10^{-5}	1×10^{-4}	2×10^{-4}	9×10^{-5}	3×10^{-5}	3×10^{-5}

[a] Concentrations of $^3C^*$ and $^{\bullet}OH_{aq}$ represent the midday peak three hours of sunlight for each filter, averaged across all days in the composite. Concentrations of NO_2, O_3, and HONO are averaged over the entire time period of each composite, not just the peak daylight hours.

[b] The gas-phase $^{\bullet}OH$ concentration is the predicted peak daytime concentration averaged over the campaign (Kuhn et al., in preparation). The subsequent rate of sulfate formation from gas-phase $^{\bullet}OH$ is an upper-bound daytime value. The $^{\bullet}OH$ concentration predicted in Fairbanks is higher than typically expected for northern latitude winter conditions due to the abundance of HONO, which is the dominant daytime gas-phase $^{\bullet}OH$ source in Fairbanks (Kuhn et al., in preparation).

[c] The relative standard deviation for the predicted $^3C^*$ concentrations in ALW ranges from 45 to 74%.

[d] The secondary sulfate formation model is based on measurements in the House site extracts, which we only extracted in pH 1 solution. [$^{\bullet}OH$] at pH 5 was estimated using $[\bullet OH]_{pH5} = [\bullet OH]_{pH1} \times 0.42$ based on the ratio $[\bullet OH]_{pH5}:[\bullet OH]_{pH1}$ determined in the CTC samples (Figure 5).

[e] The relative standard deviations for $^{\bullet}OH$ concentrations in ALW at pH 1 and 5 range from 6 to 25%.

[f] Soluble metal concentrations were measured in dilute particle extracts (Sunday et al., 2024) prepared from separate filter squares extracted into pH 1 H_2SO_4 solution and into Milli-Q water to determine the pH 1 and 5 metal concentrations, respectively. The concentration of metals in ALW was determined by multiplying the measured concentrations in particle extracts by the concentration factor between extracts and ALW conditions (Table S15).

[g] The fraction of the total water-soluble Fe pool that is Fe(II) during daylight hours is estimated to be 80% (Deguillaume et al., 2004). We considered this in our calculations by multiplying the concentrations reported in the table by 0.2, the fraction of Fe(III) available for reaction during daylight hours. To calculate the activity of Fe, we use the activity coefficient of 0.001 reported by Song et al. (2021) for both Fe(III) and Fe(II).

[h] The fraction of the total water-soluble Mn pool that is Mn(II) during daylight hours is estimated to be 70% (Majestic et al., 2007). We considered this in our calculations by multiplying the concentrations reported in the table by 0.7, the fraction of Mn(II) available for reactions during daylight hours. To determine the activity of Mn, we calculated activity coefficients between 0.06 and 0.09 as described by Martin & Hill (1987).

Table S20. Secondary sulfate model components: ALWC, ionic strength, total SO_4^{2-}, fraction 2° SO_4^{2-}, HMS, & inorganic S(IV)

Sample	$PM_{2.5}$ [a] ($\mu g\ m^{-3}$)	ALWC ($\mu g\ m^{-3}$) [b]	Ionic Strength (I_s) (M) [b]	Total SO_4^{2-} ($\mu g\ m^{-3}$) [c]	2° SO_4^{2-} (%) [d]	HMS ($\mu g\ m^{-3}$) [e]	Inorganic S(IV) (and labile organo-S(IV) complexes)						
							S(IV) Activity Coefficient (γ_{Is})	Measured [f]		Henry's Law Predicted Activity {M}		Model-Predicted Activity {M} [g]	
								($\mu g\ m^{-3}$)	{M}	pH 1	pH 5	Low pH [h]	High pH [i]
1/15	7.5	9.4	13	N/A									
1/21	12.0	12	13	3.0	19	0.29	0.73	0.37	0.27	9×10^{-8}	6×10^{-5}	0.01	0.002
1/27	17.7	11	14	4.0	28	0.50	0.70	0.76	0.58	9×10^{-8}	1×10^{-4}	0.01	0.0005
1/31	26.1	16	15	6.5	23	1.2	0.77	1.4	0.85	2×10^{-7}	6×10^{-4}	0.07	0.02
2/4	8.6	4.9	23	3.3	36	0.42	0.52	0.47	0.61	8×10^{-8}	6×10^{-5}	0.006	0.001
2/7	4.3	1.9	18	1.2	53	0.039	0.62	0.035	0.14	2×10^{-8}	1×10^{-6}	0.003	0.0008
2/14	7.2	6.1	14	2.1	37	0.12	0.69	0.15	0.21	5×10^{-8}	1×10^{-5}	0.01	0.005
2/22	3.6	9.5	5	1.0	57	0.07	0.82	0.06	0.06	3×10^{-8}	2×10^{-6}	0.001	N/A
2/24	12.5	32	5	3.1	22	0.43	0.82	0.35	0.11	3×10^{-8}	2×10^{-5}	0.03	0.01

[a] $PM_{2.5}$ measured at the NCore site by the Alaska Department of Environmental conservation, https://www.epa.gov/outdoor-air-quality-data/download-daily-data.

[b] Aerosol liquid water content (ALWC) determined using the ISORROPIA model as outlined in Campbell et al. (2024), accounting for the uptake of water by inorganic and organic components.

[c] Total sulfate (i.e., primary and secondary) measured in bulk (PM_{10}) filter sample extracts.

[d] Percent of total sulfate that is secondary, as reported by (Moon et al., 2024) and averaged over each composite period.

[e] Mass concentration of hydroxymethanesulfonate (HMS) in PM_{10}. This was determined as the S(IV) signal in the ion chromatograph that remained after adding HOOH to the extraction solution, which removes inorganic S(IV) (Dingilian et al., 2024).

[f] The measured inorganic S(IV) atmospheric concentration (and ALW activity) were determined as the difference in bisulfite/sulfite determined by ion chromatography in two different extracts of the same filter: (1) extraction in purified water minus (2) extraction in water containing HOOH. It appears that labile organo-S(IV) species on the PM decompose to inorganic S(IV) during filter extraction, so these species also appear as inorganic S(IV) during this measurement (Dingilian et al., 2024). Values were converted from $\mu g\ m^{-3}$ to molarity using the ALWC.

[g] The model-predicted activity of inorganic S(IV) is defined as the point where the fraction of secondary sulfate formed by HOOH in the model matches the measurements from Moon et al. (2024). They differ between high and low pH conditions because rates of secondary sulfate formation are pH dependent for several of the reactions included here.

[h] The "low pH" regime reflects calculations performed at pH 1.

[i] The "high pH" regime reflects calculations performed between pH 4 and 5.

Table S21. Daytime rates of secondary SO_4^{2-} formation ($\mu g\ m^{-3}\ hr^{-1}$) under high and low pH conditions

Conditions	Oxidant [a]	House Site Sample								
		1/15	1/21	1/27	1/31	2/4	2/7	2/14	2/22	2/24
Daytime, Low pH [b]	HOOH	N/A [d]	0.088	0.051	0.49	0.077	0.077	0.18	0.053	0.22
	O_3		0.105	0.076	0.076	0.16	0.076	0.28	0.033	0.078
	$^{\bullet}OH_g$		0.054	0.054	0.098	0.054	0.018	0.054	0.054	0.054
	NO_2		0.023	0.017	0.12	0.0020	0.0010	0.021	0.0076	0.15
	$^3C^*$		0.0066	0.0020	0.096	0.0011	0.0020	0.020	0.0036	0.054
	$^{\bullet}OH_{aq}$		0.0015	2.9×10^{-4}	0.0098	0.0001	7.4×10^{-5}	0.0025	0.0015	0.036
	TMI		0.0016	1.4×10^{-5}	4.6×10^{-4}	3.0×10^{-4}	2.0×10^{-4}	0.0016	0.0013	0.029
	HONO		0.0028	0.0011	0.011	6.6×10^{-5}	4.1×10^{-5}	8.7×10^{-4}	2.4×10^{-4}	N/A
	Total Rate		**0.28**	**0.20**	**0.91**	**0.29**	**0.17**	**0.56**	**0.15**	**0.56**
Daytime, High pH [c]	HOOH		0.035	0.021	0.20	0.031	0.036	0.071	N/A [e]	0.087
	O_3		0.022	0.005	0.016	0.032	0.027	0.093		0.079
	$^{\bullet}OH_g$		0.054	0.054	0.098	0.054	0.018	0.054		0.054
	NO_2		7.5×10^{-4}	5.7×10^{-4}	0.029	1.7×10^{-4}	1.6×10^{-4}	0.0030		0.019
	$^3C^*$		2.2×10^{-4}	6.7×10^{-5}	0.023	9.6×10^{-5}	3.3×10^{-4}	0.0029		0.0068
	$^{\bullet}OH_{aq}$		1.5×10^{-5}	4.4×10^{-6}	6.6×10^{-4}	2.7×10^{-6}	3.5×10^{-6}	9.9×10^{-5}		0.0013
	TMI		8.9×10^{-5}	7.2×10^{-6}	3.9×10^{-4}	3.7×10^{-5}	1.9×10^{-5}	1.1×10^{-4}		0.0011
	HONO		9.6×10^{-6}	3.9×10^{-6}	2.7×10^{-4}	5.9×10^{-7}	7.1×10^{-7}	1.3×10^{-5}		N/A
	Total Rate		**0.11**	**0.080**	**0.36**	**0.12**	**0.082**	**0.23**		**0.24**

[a] HOOH, $^3C^*$, and $^{\bullet}OH_{aq}$ formation rates, and TMI concentrations, reflect measurements made on filter samples from the House site.
[b] The "low pH" regime reflects calculations performed at pH 1.
[c] The "high pH" regime reflects calculations performed between pH 4 and 5.
[d] Calculations could not be run for the 1/15 composite period since there were no actinic flux measurements.
[e] For the 2/22 High pH daytime composite, no valid model results were obtained because even at very low {inorganic S(IV)}, the maximum modelled fraction of secondary SO_4^{2-} produced by HOOH is smaller than the measured fraction reported by Moon et al. (2024).

Table S22. Parameters for modelling monthly average actinic fluxes with TUV

Date	Snow on the Ground?	Albedo [a]	Solar Noon [b]	Solar Zenith Angle at Solar Noon [b]
6/15/2021	No	0.1	13:51	41.5
7/15/2021	No	0.1	13:56	43.5
8/15/2021	No	0.1	13:55	51.1
9/15/2021	No	0.1	13:45	62.1
10/15/2021	No	0.1	13:36	73.6
11/15/2021	Slight	0.3	12:35	83.4
12/15/2021	Yes	0.85	12:46	87.9
1/15/2022	Yes	0.85	13:00	85.7
2/15/2022	Yes	0.85	13:04	77.2
3/15/2022	Yes	0.85	13:59	66.7
4/15/2022	Yes	0.4	13:50	54.8
5/15/2022	No	0.1	13:47	45.8
6/15/2022	No	0.1	13:51	41.5

[a] Wintertime albedo estimated based on upwelling-to-downwelling j_{NO2} measured during ALPACA and adjusted year-round based on snow cover.

[b] Determined from https://www.timeanddate.com/sun/usa/fairbanks?month=2&year=2022.

Table S23 a). Estimating $O(^1D)$ loss pathways and production rates of $^{\bullet}OH(g)$ from ozone photolysis ($P_{O3\rightarrow\bullet OH}$)

Month-Year	Average Temperature (°C)	Average Relative Humidity (%)	H_2O Saturation Vapor Pressure (mbar)	$[H_2O(g)]$ (mlc cm^{-3})	$P_{O3\rightarrow\bullet OH}$ (mlc cm^{-3} s^{-1})
Jun-21	18	56	21	2.9×10^{17}	2.2×10^{6}
Jul-21	18	59	21	3.0×10^{17}	1.9×10^{6}
Aug-21	13	80	15	3.0×10^{17}	9.3×10^{5}
Sep-21	6.0	74	9.4	1.8×10^{17}	1.9×10^{5}
Oct-21	-1.5	86	5.5	1.3×10^{17}	2.7×10^{4}
Nov-21	-17	79	1.6	3.6×10^{16}	2.1×10^{3}
Dec-21	-17	82	1.6	3.7×10^{16}	1.8×10^{3}
Jan-22	-20	77	1.2	2.7×10^{16}	1.5×10^{3}
Feb-22	-17	79	1.6	3.6×10^{16}	2.3×10^{4}
Mar-22	-6.9	64	3.6	6.4×10^{16}	2.5×10^{5}
Apr-22	-0.90	49	5.7	7.4×10^{16}	6.3×10^{5}
May-22	11	50	13	1.6×10^{17}	1.4×10^{6}
Jun-22	17	49	20	2.4×10^{17}	2.6×10^{6}

610

Table S23 b). Estimated monthly photochemical rate constants for O_3, HONO, and BrC in Fairbanks. Values were calculated for midday on the 15th day of each month.

Month-Year	$j_{BrC \rightarrow 3C^*}$ (s^{-1})	$j_{O3 \rightarrow O(1D)}$ (s^{-1})	$j_{O3 \rightarrow \bullet OH}$ (s^{-1})	$j_{HONO \rightarrow \bullet OH}$ (s^{-1})
Jun-21	3.1×10^{-4}	2.3×10^{-5}	3.0×10^{-6}	1.5×10^{-3}
Jul-21	3.0×10^{-4}	2.2×10^{-5}	2.9×10^{-6}	1.4×10^{-3}
Aug-21	2.6×10^{-4}	1.5×10^{-5}	2.0×10^{-6}	1.2×10^{-3}
Sep-21	1.9×10^{-4}	6.6×10^{-6}	5.3×10^{-7}	9.0×10^{-4}
Oct-21	1.0×10^{-4}	1.7×10^{-6}	9.2×10^{-8}	4.6×10^{-4}
Nov-21	3.6×10^{-5}	3.6×10^{-7}	5.4×10^{-9}	1.7×10^{-4}
Dec-21	2.2×10^{-5}	2.1×10^{-7}	3.2×10^{-9}	1.1×10^{-4}
Jan-22	4.0×10^{-5}	4.2×10^{-7}	4.6×10^{-9}	2.1×10^{-4}
Feb-22	1.5×10^{-4}	2.5×10^{-6}	3.8×10^{-8}	7.5×10^{-4}
Mar-22	3.5×10^{-4}	1.1×10^{-5}	3.0×10^{-7}	1.7×10^{-3}
Apr-22	3.5×10^{-4}	1.8×10^{-5}	5.8×10^{-7}	1.7×10^{-3}
May-22	2.9×10^{-4}	1.9×10^{-5}	1.4×10^{-6}	1.4×10^{-3}
Jun-22	3.1×10^{-4}	2.3×10^{-5}	2.6×10^{-6}	1.5×10^{-3}

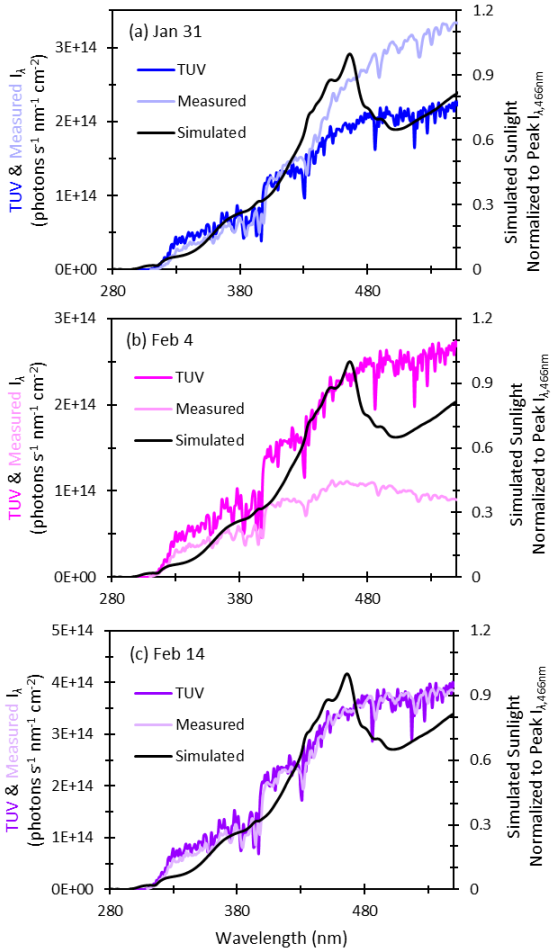

Figure S1. Comparison of laboratory, field, and modeled photon fluxes (I_λ) on (a) January 31st, (b) February 4th, and (c) February 14th. The dark colored lines are modelled total actinic flux from TUV solar noon on each specified day and the light colored lines are the total actinic flux measured on each specified day in Fairbanks, AK at 13:30, near solar noon. Both measurements and modeled results are total actinic flux, i.e., the sum of upwelling and downwelling. The black line represents the normalized photon fluxes of laboratory simulated sunlight. TUV data is from https://www.acom.ucar.edu/Models/TUV/Interactive_TUV/.

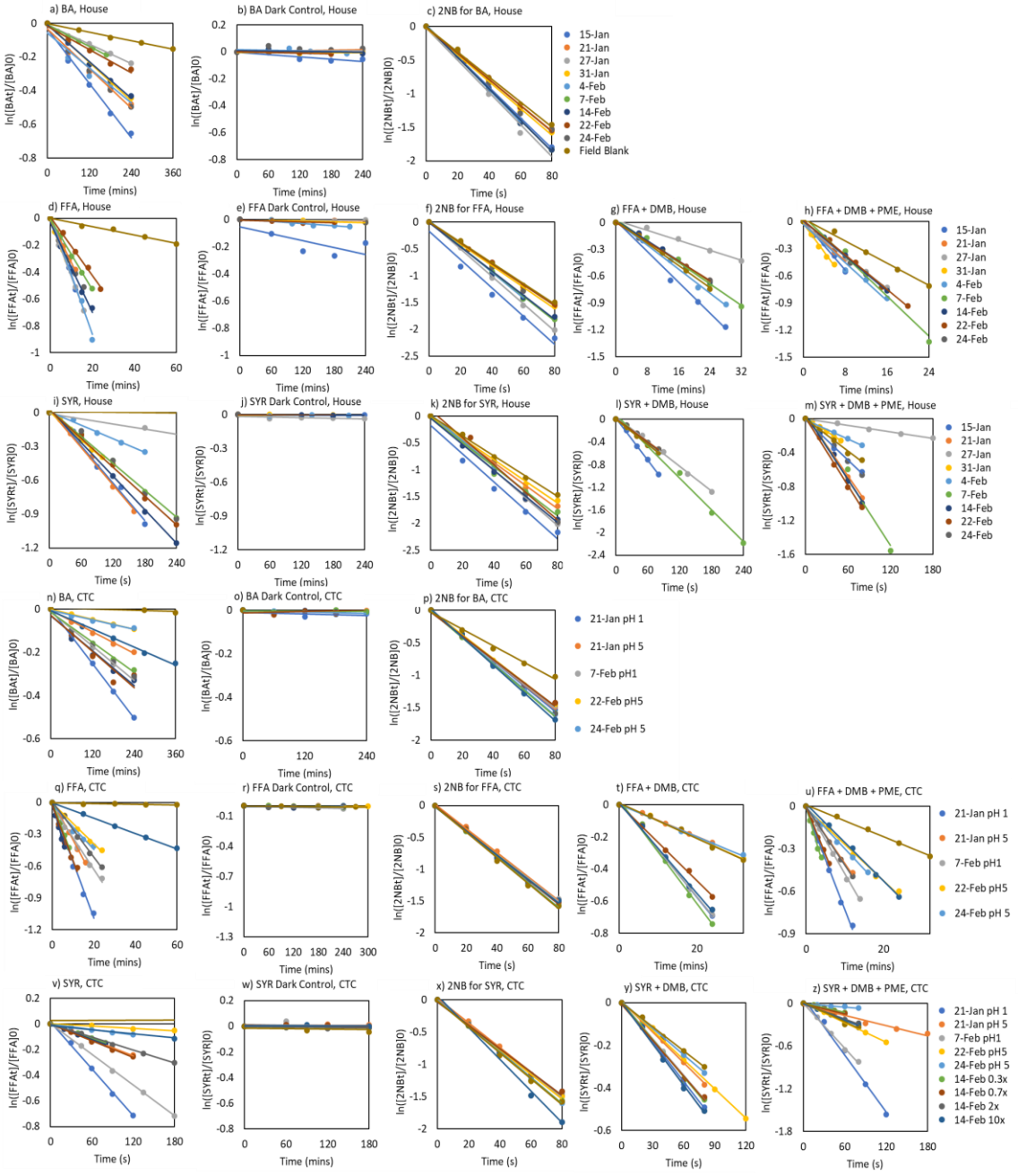

Figure S2. Raw Experimental Data: BA, FFA, SYR, and 2-NB Decay Plots for the House (a-m) and CTC (n-z) sites.

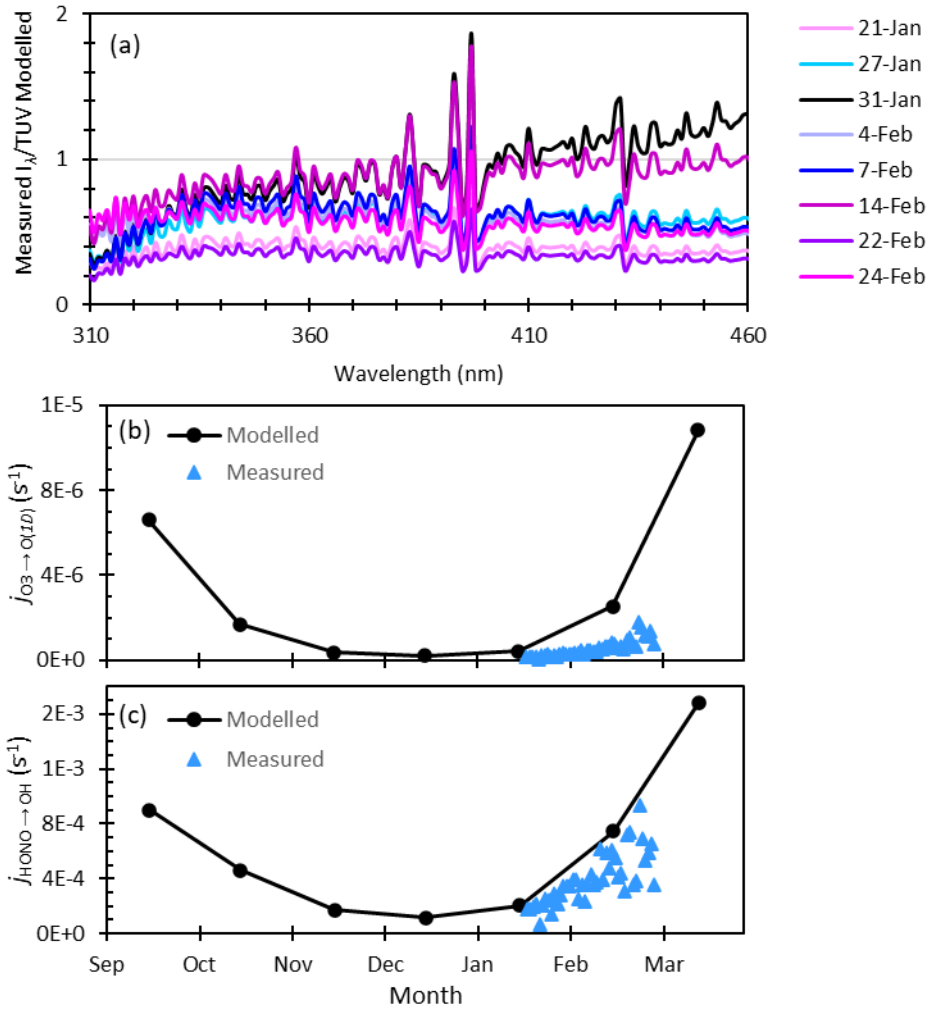

630

Figure S3. Comparison of modelled and measured actinic fluxes (I_λ) and photochemical rate constants (j). (a) Ratio of modelled (TUV) and measured actinic fluxes at midday on each composite midpoint date. (b) Rate constants for ozone photolysis ($j_{O3 \rightarrow O(1D)}$) and (c) rate constants for photolysis of HONO ($j_{HONO \rightarrow \bullet OH}$) on the 15th day of each month.

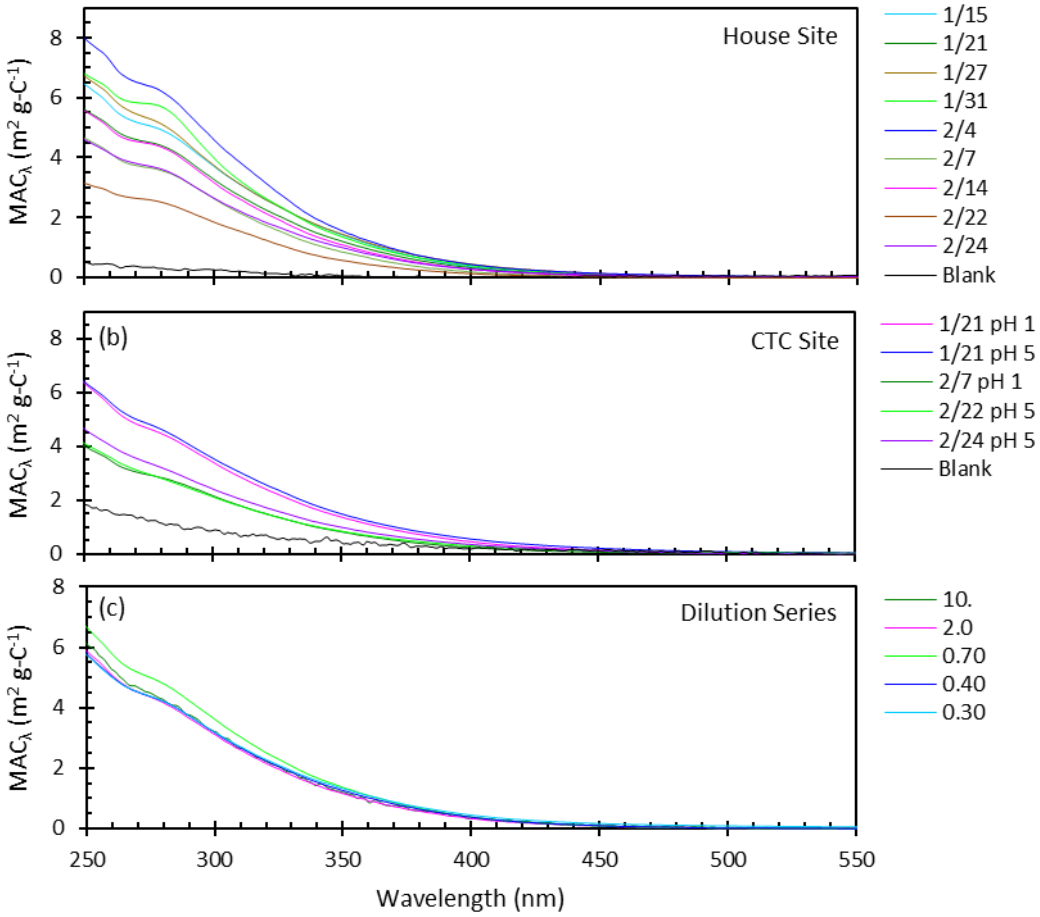

635

Figure S4. Spectrally resolved mass absorption coefficients of particle extracts at (a) the House site, (b) the CTC site, and (c) in the dilution series of the 2/14 CTC sample. In panel (c), each legend number represents the volume of H_2SO_4 solution used to extract each filter square for that dilution. While absorbance values at wavelengths above 500 nm look minimal, these wavelengths contribute to BrC photochemistry under Fairbanks sunlight.

640

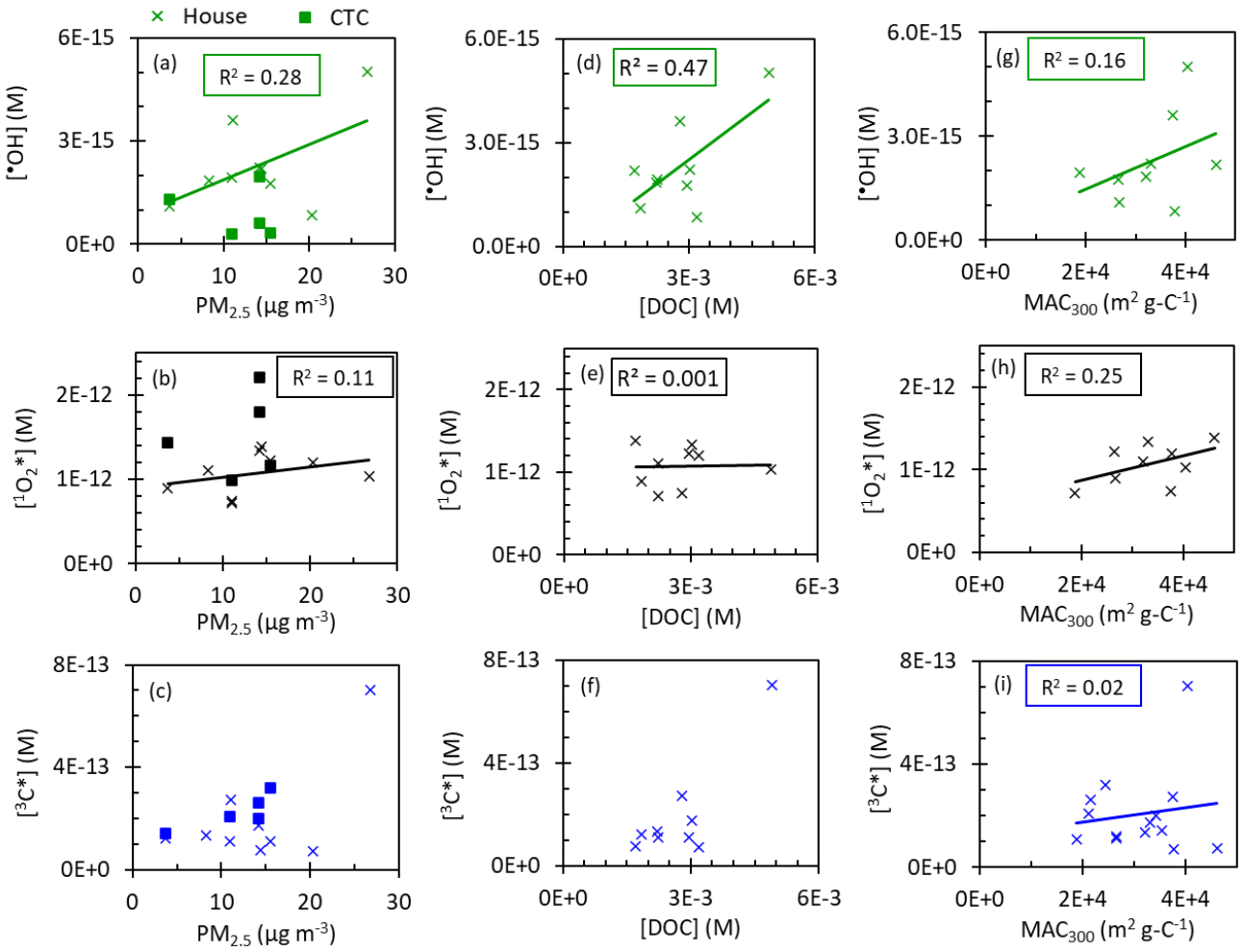

Figure S5. Correlations of $^{\bullet}OH$, $^{1}O_2^*$, and $^{3}C^*$ concentrations with $PM_{2.5}$, $[DOC]_{PME}$, and MAC_{300}. (a) – (c) all depict House (marked with 'x') and CTC site samples (marked with filled squares), while (d) – (i) only show House site samples. The regressions were calculated using only the House site samples to control for site differences. $[DOC]_{PME}$ at the House and CTC sites cannot be compared because the filters at the two sites collected different size bins, with the House site representing $PM_{2.5}$ and the CTC site representing $PM_{0.7}$.

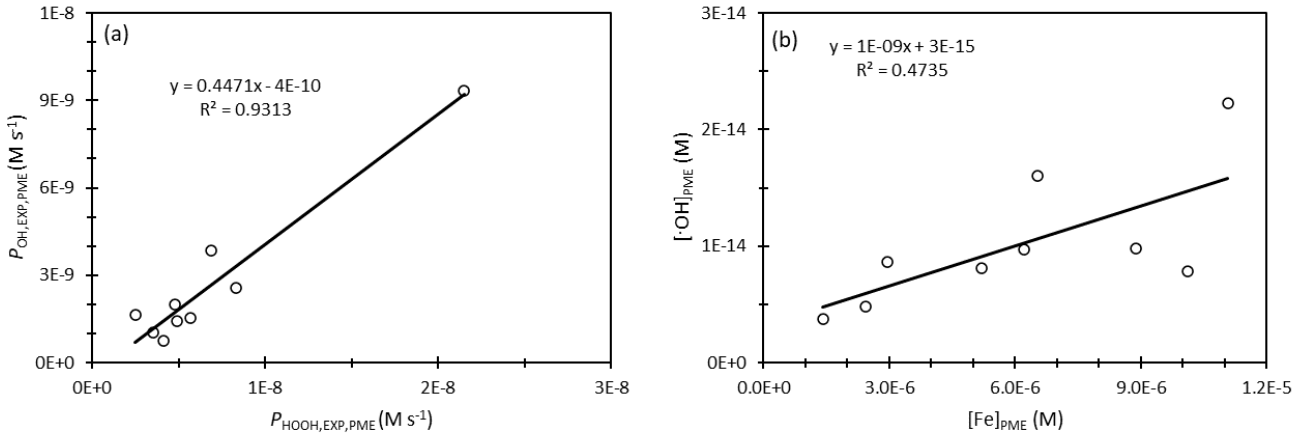

Figure S6. Correlations exploring •OH sources. (a) $P_{\bullet OH,EXP,PME}$ versus $P_{HOOH,EXP,PME}$. (b) •OH concentration versus soluble Fe concentrations in pH 1 extracts.

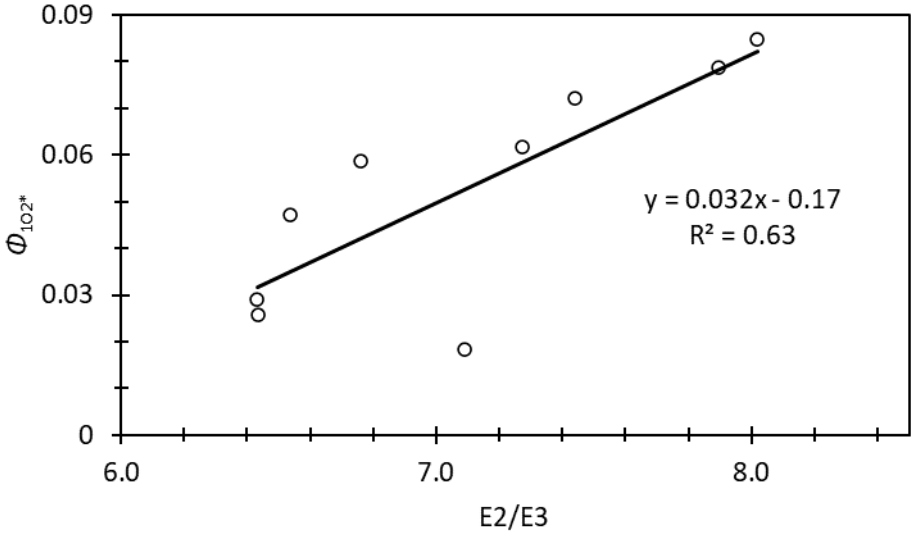

655

Figure S7. Relationship of Φ_{1O2*} and E2/E3.

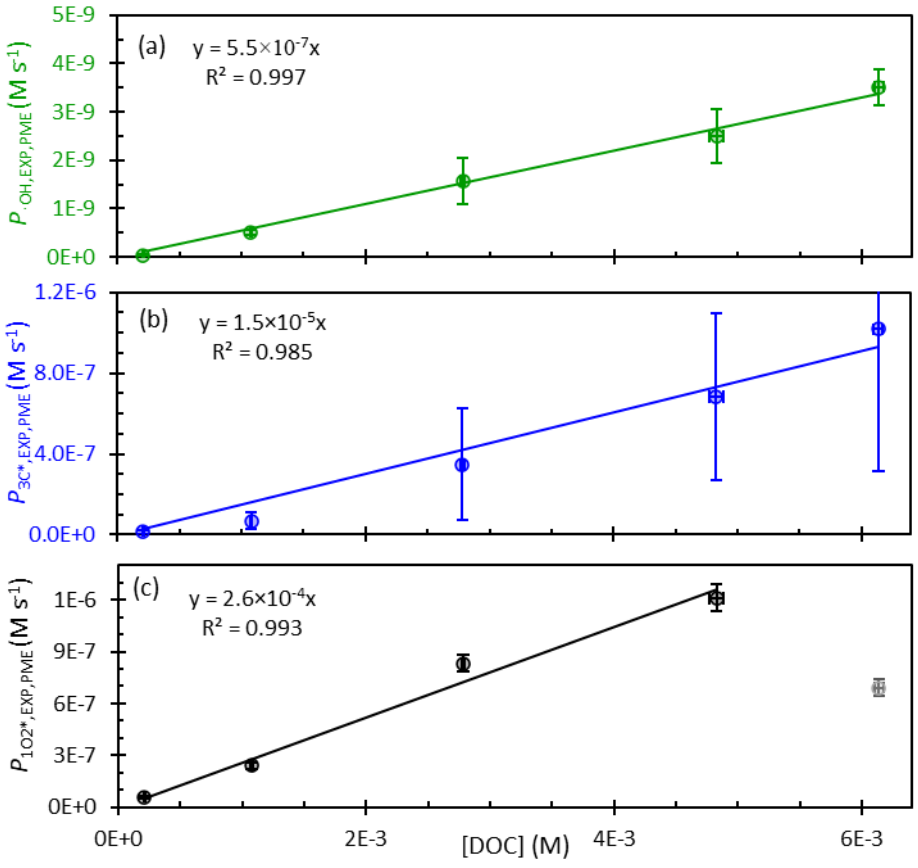

660 **Figure S8.** Formation rates from the dilution series for CTC sample 2/14 for (a) •OH, (b) $^3C^*$, and (c) $^1O_2^*$ as a function of $[DOC]_{PME}$. Formation rates are normalized to the average midday actinic flux on February 1st in Fairbanks (equivalent to $j_{2NB,AK}$ = 0.0045 s^{-1}). Solid lines represent linear regression fits to the experimental data. For panel (c), the point corresponding to the $^1O_2^*$ production rate at the highest DOC is not included in the regression.

665

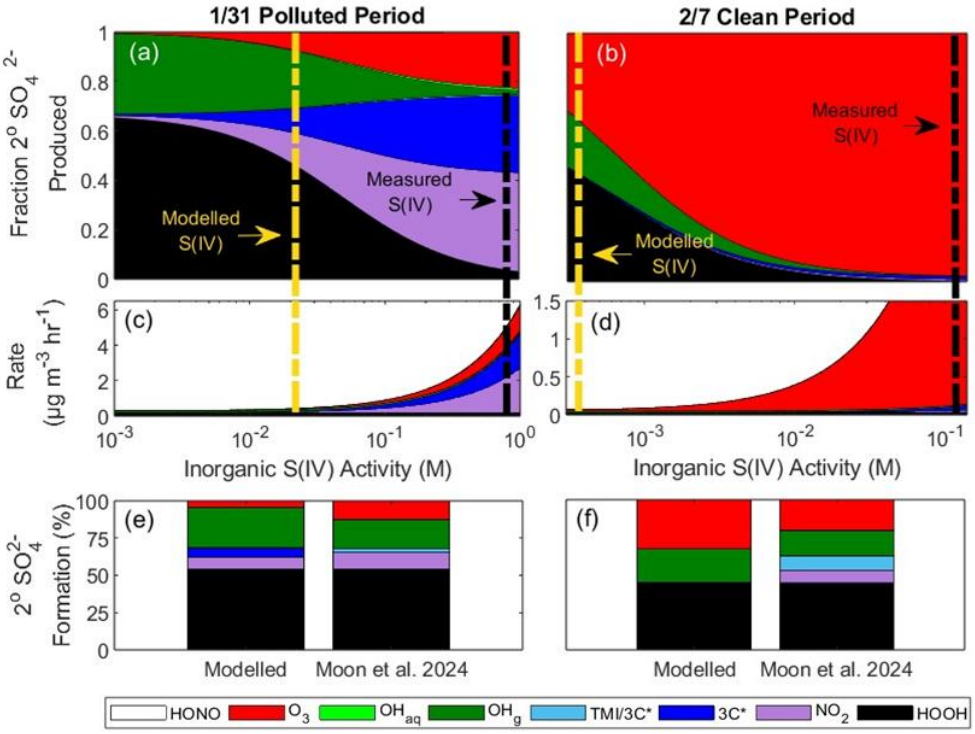

Figure S9. Modelled secondary (2°) SO_4^{2-} formation under high pH (pH 4-5), daytime conditions during the 1/31 polluted period and 2/7 clean period due to HOOH, NO_2, $^3C^*$, O_2 catalyzed by transition metal ions (TMI), gas-phase $^\bullet OH$, aqueous-phase $^\bullet OH$, and O_3. Panels (a) and (b) show the fraction of secondary SO_4^{2-} formation from the different oxidation pathways as a function of the activity of particle inorganic S(IV), i.e., sulfite and bisulfite. The black vertical dashed lines are the ALW inorganic S(IV) activities based on PM measurements, assuming all the HOOH-labile S(IV) is inorganic. The yellow vertical dashed lines are the ALW inorganic S(IV) activities at which our modelled fractions of secondary sulfate from HOOH match the fractions determined from isotopic measurements (Moon et al., 2024). Panels (c) and (d) show the total rate of secondary SO_4^{2-} formation from all pathways. Panels (e) and (f) show the percent contribution of each oxidant to secondary SO_4^{2-} formation at the modelled concentrations of inorganic S(IV) and the corresponding isotope-determined oxidant contributions from Moon et al. (2024). In our model results, sulfate formation from TMI is too small to see.

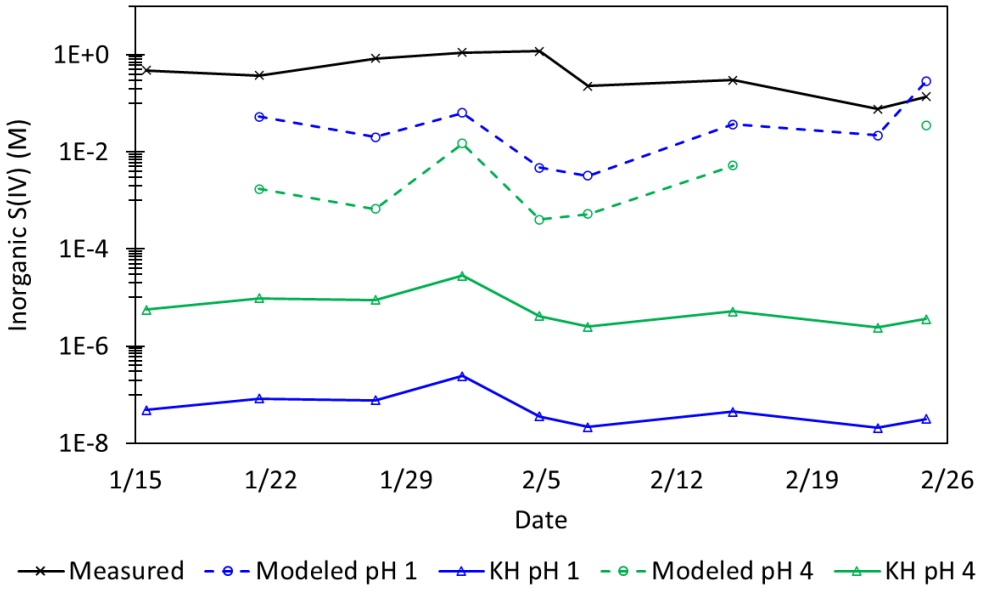

Figure S10. Inorganic S(IV) concentrations comparing measurements (black line), model results (dashed blue (pH 1) and green (pH 4) lines), and predictions from Henry's Law (K_H; solid blue (pH 1) and green (pH 4) lines). The measured values are likely overestimates because they probably include contributions from labile organo-S(IV) complexes that broke down to inorganic S(IV) when the filters were extracted.

References

Air Quality Monitoring Data: https://www.epa.gov/outdoor-air-quality-data/download-daily-data, last access: 10 November 2024.

Anastasio, C. and McGregor, K. G.: Chemistry of fog waters in California's Central Valley: 1. In situ photoformation of hydroxyl radical and singlet molecular oxygen, Atmos Environ, 35, 1079–1089, https://doi.org/10.1016/S1352-2310(00)00281-8, 2001.

Anastasio, C., Faust, B. C., and Rao, C. J.: Aromatic Carbonyl Compounds as Aqueous-Phase Photochemical Sources of Hydrogen Peroxide in Acidic Sulfate Aerosols, Fogs, and Clouds. 1. Non-Phenolic Methoxybenzaldehydes and Methoxyacetophenones with Reductants (Phenols), Environ Sci Technol, 31, 218–232, https://doi.org/https://doi.org/10.1021/es960359g, 1997.

Appiani, E., Ossola, R., Latch, D. E., Erickson, P. R., and McNeill, K.: Aqueous singlet oxygen reaction kinetics of furfuryl alcohol: Effect of temperature, pH, and salt content, Environ Sci Process Impacts, 19, 507–516, https://doi.org/10.1039/c6em00646a, 2017.

Arakaki, T., Anastasio, C., Kuroki, Y., Nakajima, H., Okada, K., Kotani, Y., Handa, D., Azechi, S., Kimura, T., Tsuhako, A., and Miyagi, Y.: A General Scavenging Rate Constant for Reaction of Hydroxyl Radical with Organic Carbon in Atmospheric Waters, Environ Sci Technol, 47, 8196–8203, https://doi.org/10.1021/es401927b, 2013.

Arciva, S., Niedek, C., Mavis, C., Yoon, M., Sanchez, M. E., Zhang, Q., and Anastasio, C.: Aqueous ·OH Oxidation of Highly Substituted Phenols as a Source of Secondary Organic Aerosol, Environ Sci Technol, 56, 9959–9967, https://doi.org/10.1021/acs.est.2c02225, 2022.

Ashton, L., Buxton, G. V, and Stuart, C. R.: Temperature Dependence of the Rate of Reaction of OH with Some Aromatic Compounds in Aqueous Solution Evidence for the Formation of a n-Complex Intermediate?, Journal of the Chemical Society, Faraday Transactions, 1631–1633, 1995.

Bogler, S., Daellenbach, K. R., Bell, D. M., Prévôt, A. S. H., El Haddad, I., and Borduas-Dedekind, N.: Singlet Oxygen Seasonality in Aqueous PM_{10} is Driven by Biomass Burning and Anthropogenic Secondary Organic Aerosol, Environ Sci Technol, 56, 15389–15397, https://doi.org/10.1021/acs.est.2c04554, 2022.

Cheng, Y., Zheng, G., Wei, C., Mu, Q., Zheng, B., Wang, Z., Gao, M., Zhang, Q., He, K., Carmichael, G., Pöschl, U., and Su, H.: Reactive nitrogen chemistry in aerosol water as a source of sulfate during haze events in China, Sci Adv, 2, https://doi.org/DOI: 10.1126/sciadv.1601530, 2016.

Clifton, C. L., Altstein, M., and Hule, R. E.: Rate Constant for the Reaction of NO_2 with Sulfur(IV) over the pH Range of 5.3-13, Environ. Sci. Technol, 22, 586–589, https://doi.org/https://doi.org/10.1021/es00170a018, 1988.

Deguillaume, L., Leriche, M., Monod, A., and Chaumerliac, N.: The role of transition metal ions on HOx radicals in clouds: a numerical evaluation of its impact on multiphase chemistry, Atmos. Chem. Phys, 4, 95–110, https://doi.org/https://doi.org/10.5194/acp-4-95-2004, 2004.

Dingilian, K., Hebert, E., Battaglia, M., Campbell, J. R., Cesler-Maloney, M., Simpson, W., St. Clair, J. M., Dibb, J., Temime-Roussel, B., D'Anna, B., Moon, A., Alexander, B., Yang, Y., Nenes, A., Mao, J., and Weber, R. J.: Hydroxymethanesulfonate and Sulfur(IV) in Fairbanks Winter During the ALPACA Study, ACS ES&T Air, 1, 646–659, https://doi.org/10.1021/acsestair.4c00012, 2024.

Edwards, K. C., Kapur, S., Fang, T., Cesler-Maloney, M., Yang, Y., Holen, A. L., Wu, J., Robinson, E. S., DeCarlo, P. F., Pratt, K. A., Weber, R. J., Simpson, W. R., and Shiraiwa, M.: Residential Wood Burning and Vehicle Emissions as Major Sources of Environmentally Persistent Free Radicals in Fairbanks, Alaska, Environ Sci Technol, https://doi.org/10.1021/acs.est.4c01206, 2024.

Haag, W. R. and Hoigne, J.: Siglet Oxygen in Surface Waters. 3. Photochemical Formation and Steady-State Concentrations in Various Types of Waters, J. Environ. Sci. Technol, 20, 341–348, https://doi.org/doi.org/10.1021/es00146a005, 1986.

Helms, J. R., Stubbins, A., Ritchie, J. D., Minor, E. C., Kieber, D. J., and Mopper, K.: Absorption spectral slopes and slope ratios as indicators of molecular weight, source, and photobleaching of chromophoric dissolved organic matter, Limnol Oceanogr, 53, 955–969, https://doi.org/10.4319/lo.2008.53.3.0955, 2008.

Hullar, T., Bononi, F. C., Chen, Z., Magadia, D., Palmer, O., Tran, T., Rocca, D., Andreussi, O., Donadio, D., and Anastasio, C.: Photodecay of guaiacol is faster in ice, and even more rapid on ice, than in aqueous solution, Environ Sci Process Impacts, 22, 1666–1677, https://doi.org/10.1039/d0em00242a, 2020.

Ibusuki, T. and Takeuchi, K.: Sulfur dioxide oxidation by oxygen catalyzed by mixtures of manganese(II) and iron(III) in aqueous solutions at environmental reaction conditions, Atmos Environ, 21, 1555–1560, https://doi.org/https://doi.org/10.1016/0004-6981(87)90317-9, 1986.

Kaur, R., Labins, J. R., Helbock, S. S., Jiang, W., Bein, K. J., Zhang, Q., and Anastasio, C.: Photooxidants from brown carbon and other chromophores in illuminated particle extracts, Atmos Chem Phys, 19, 6579–6594, https://doi.org/10.5194/acp-19-6579-2019, 2019.

Kim, S., Vandenboer, T. C., Young, C. J., Riedel, T. P., Thornton, J. A., Swarthout, B., Sive, B., Lerner, B., Gilman, J., Warneke, C., Roberts, J. M., Guenther, A., Wagner, N. L., Dubé, W. P., Williams, E., and Brown, S. S.: The primary and recycling sources of OH during the NACHTT-2011 campaign: HONO as an important OH primary source in the wintertime, J Geophys Res, 119, 6886–6896, https://doi.org/10.1002/2013JD019784, 2014.

Kuhn, J., Heinlein, L. M. D., Cesler-Maloney, M., Stutz, J., Anastasio, C., Simpson, W., Dibb, J., Jennie, T., Bartels-Rausch, T., Sunday, M. O., Guo, F., Flynn III, J. H., and Fahey, K.: Oxidation in Polluted Surface Layers During High-Latitude Winter, Atmos Chem Phys, n.d.

Lee, Y. and Schwartz, S. E.: Kinetics of oxidation of aqueous sulfur (IV) by nitrogen dioxide, Precipitation Scavenging, Dry Deposition and Resuspension, 1, 453–470, 1983.

Ma, L., Guzman, C., Niedek, C., Tran, T., Zhang, Q., and Anastasio, C.: Kinetics and Mass Yields of Aqueous Secondary Organic Aerosol from Highly Substituted Phenols Reacting with a Triplet Excited State, Environ Sci Technol, 55, 5772–5781, https://doi.org/10.1021/acs.est.1c00575, 2021.

Ma, L., Worland, R., Tran, T., and Anastasio, C.: Evaluation of Probes to Measure Oxidizing Organic Triplet Excited States in Aerosol Liquid Water, Environ Sci Technol, 57, 6052–6062, https://doi.org/10.1021/acs.est.2c09672, 2022.

Ma, L., Worland, R., Jiang, W., Niedek, C., Guzman, C., Bein, K. J., Zhang, Q., and Anastasio, C.: Predicting photooxidant concentrations in aerosol liquid water based on laboratory extracts of ambient particles, Atmos Chem Phys, 23, 8805–8821, https://doi.org/10.5194/acp-23-8805-2023, 2023.

Ma, L., Worland, R., Heinlein, L., Guzman, C., Jiang, W., Niedek, C., Bein, K. J., Zhang, Q., and Anastasio, C.: Seasonal variations in photooxidant formation and light absorption in aqueous extracts of ambient particles, Atmos Chem Phys, 24, 1–21, https://doi.org/10.5194/acp-24-1-2024, 2024.

Machado, A. E. H., Gomes, A. J., Campos, C. M. F., Terrones, M. G. H., Perez, D. S., Ruggiero, R., and Castellan, A.: Photoreactivity of lignin model compounds in the photobleaching of chemical pulps 2. Study of the degradation of 4-hydroxy-3-methoxy-benzaldehyde and two lignin fragments induced by singlet oxygen, 1997.

Madronich, S. and Flocke, S.: The role of solar radiation in atmospheric chemistry, in: Handbook of Environmental Chemistry, Springer-Verlag, 1–26, 1998.

Majestic, B. J., Schauer, J. J., and Shafer, M. M.: Development of a manganese speciation method for atmospheric aerosols in biologically and environmentally relevant fluids, Aerosol Science and Technology, 41, 925–933, https://doi.org/10.1080/02786820701564657, 2007.

Martin, L. R. and Hill, M. W.: The Effect of Ionic Strength on the Manganese Catalyzed Oxidation of Sulfur (IV), Atmos Environ, 21, 2267–2270, https://doi.org/https://doi.org/10.1016/0004-6981(87)90361-1, 1987.

McNeill, K. and Canonica, S.: Triplet state dissolved organic matter in aquatic photochemistry: Reaction mechanisms, substrate scope, and photophysical properties, Environ Sci Process Impacts, 18, 1381–1399, https://doi.org/10.1039/c6em00408c, 2016.

Millero, F., Hershey, J. P., Johnson, G., and Zhang, J.-Z.: The Solubility of SO_2 and the Dissociation of H_2SO_3 in NaCl Solutions, J Atmos Chem, 8, 377–389, https://doi.org/https://doi.org/10.1007/BF00052711, 1989.

Moon, A., Jongebloed, U., Dingilian, K. K., Schauer, A. J., Chan, Y.-C., Cesler-Maloney, M., Simpson, W. R., Weber, R. J., Tsiang, L., Yazbeck, F., Zhai, S., Wedum, A., Turner, A. J., Albertin, S., Bekki, S., Savarino, J., Gribanov, K., Pratt, K. A., Costa, E. J., Anastasio, C., Sunday, M. O., Heinlein, L. M. D., Mao, J., and Alexander, B.: Primary Sulfate Is the Dominant Source of Particulate Sulfate during Winter in Fairbanks, Alaska, ES&T Air, 1, 139–149, https://doi.org/10.1021/acsestair.3c00023, 2024.

Peuravuori, J. and Pihlaja, K.: Molecular size distribution and spectroscopic properties of aquatic humic substances, Anal Chim Acta, 337, 133–149, 1997.

Ross, A. B., Mallard, W. G., Helman, W. P., Buxton, G. V., Huie, R., and Neta, E. P.: NDRL-NIST Solution Kinetics Database - Version 2, Gaithersburg, MD, 1994.

Ross, F. and Ross, A. B.: Selected specific rates of reactions of transients from water in aqueous solution, Gaithersburg, MD, https://doi.org/10.6028/NBS.NSRDS.59, 1977.

Sander, R.: Compilation of Henry's law constants (version 5.0.0) for water as solvent, https://doi.org/10.5194/acp-23-10901-2023, 6 October 2023.

Seinfeld, J. H. and Pandis, S. N.: Atmospheric Chemistry and Physics: From Air Pollution to Climate Change, 3rd ed., Wiley, 2016.

Simpson, W. R., Mao, J., Fochesatto, G. J., Law, K. S., DeCarlo, P. F., Schmale, J., Pratt, K. A., Arnold, S. R., Stutz, J., Dibb, J. E., Creamean, J. M., Weber, R. J., Williams, B. J., Alexander, B., Hu, L., Yokelson, R. J., Shiraiwa, M., Decesari, S., Anastasio, C., D'Anna, B., Gilliam, R. C., Nenes, A., St. Clair, J. M., Trost, B., Flynn, J. H., Savarino, J., Conner, L. D., Kettle, N., Heeringa, K. M., Albertin, S., Baccarini, A., Barret, B., Battaglia, M. A., Bekki, S., Brado, T. J., Brett, N., Brus, D., Campbell, J. R., Cesler-Maloney, M., Cooperdock, S., Cysneiros de Carvalho, K., Delbarre, H., DeMott, P. J., Dennehy, C. J. S., Dieudonné, E., Dingilian, K. K., Donateo, A., Doulgeris, K. M., Edwards, K. C., Fahey, K., Fang, T., Guo, F., Heinlein, L. M. D., Holen, A. L., Huff, D., Ijaz, A., Johnson, S., Kapur, S., Ketcherside, D. T., Levin, E., Lill, E., Moon, A. R., Onishi, T., Pappaccogli, G., Perkins, R., Pohorsky, R., Raut, J.-C., Ravetta, F., Roberts, T., Robinson, E. S., Scoto, F., Selimovic, V., Sunday, M. O., Temime-Roussel, B., Tian, X., Wu, J., and Yang, Y.: Overview of the Alaskan Layered Pollution and Chemical Analysis (ALPACA) Field Experiment, ACS ES&T Air, 1, 200–222, https://doi.org/10.1021/acsestair.3c00076, 2024.

Smith, J. D., Kinney, H., and Anastasio, C.: Aqueous benzene-diols react with an organic triplet excited state and hydroxyl radical to form secondary organic aerosol, Physical Chemistry Chemical Physics, 17, 10227–10237, https://doi.org/10.1039/c4cp06095d, 2015.

Smith, J. D., Kinney, H., and Anastasio, C.: Phenolic carbonyls undergo rapid aqueous photodegradation to form low-volatility, light-absorbing products, Atmos Environ, 126, 36–44, https://doi.org/10.1016/j.atmosenv.2015.11.035, 2016.

Song, H., Lu, K., Ye, C., Dong, H., Li, S., Chen, S., Wu, Z., Zheng, M., Zeng, L., Hu, M., and Zhang, Y.: A comprehensive observation-based multiphase chemical model analysis of sulfur dioxide oxidations in both summer and winter, Atmos Chem Phys, 21, 13713–13727, https://doi.org/10.5194/acp-21-13713-2021, 2021.

Sunday, M. O., Heinlein, L. M. D., He, J., Moon, A., Kapur, S., Fang, T., Edwards, K. C., Guo, F., Dibb, J., Flynn III, J. H., Alexander, B., Shiraiwa, M., and Anastasio, C.: Hydrogen Peroxide Photoformation in Particulate Matter and its Contribution to S(IV) Oxidation During Winter in Fairbanks, Alaska, Atmos Chem Phys, 25, 5087–5100, https://doi.org/10.5194/acp-25-5087-2025, 2025.

Tilgner, A., Schaefer, T., Alexander, B., Barth, M., Collett, J. L., Fahey, K. M., Nenes, A., Pye, H. O. T., Herrmann, H., and McNeill, V. F.: Acidity and the multiphase chemistry of atmospheric aqueous particles and clouds, Atmos Chem Phys, 21, 13483–13536, https://doi.org/10.5194/acp-21-13483-2021, 2021.

Wander, R., Neta, P., Dorfman, L. M., Flory, P. J., and Dorfman, L. M.: Pulse Radiolysis Studies. XII. Kinetics and Spectra of the Cyclohexadienyl Radicals in Aqueous Benzoic Acid Solution, Journal of Physical Chemistry, 72, 2946–2949, https://doi.org/https://doi.org/10.1021/j100854a044, 1968.

Wang, X., Gemayel, R., Hayeck, N., Perrier, S., Charbonnel, N., Xu, C., Chen, H., Zhu, C., Zhang, L., Wang, L., Nizkorodov, S. A., Wang, X., Wang, Z., Wang, T., Mellouki, A., Riva, M., Chen, J., and George, C.: Atmospheric Photosensitization: A New Pathway for Sulfate Formation, Environ Sci Technol, 54, 3114–3120, https://doi.org/10.1021/acs.est.9b06347, 2020.

Wenk, J. and Canonica, S.: Phenolic antioxidants inhibit the triplet-induced transformation of anilines and sulfonamide antibiotics in aqueous solution, Environ Sci Technol, 46, 5455–5462, https://doi.org/10.1021/es300485u, 2012.

Ye, C., Liu, P., Ma, Z., Xue, C., Zhang, C., Zhang, Y., Liu, J., Liu, C., Sun, X., and Mu, Y.: High H_2O_2 Concentrations Observed during Haze Periods during the Winter in Beijing: Importance of H_2O_2 Oxidation in Sulfate Formation, Environ Sci Technol Lett, 5, 757–763, https://doi.org/10.1021/acs.estlett.8b00579, 2018.

Yu, C., Liu, T., Ge, D., Nie, W., Chi, X., and Ding, A.: Ionic Strength Enhances the Multiphase Oxidation Rate of Sulfur Dioxide by Ozone in Aqueous Aerosols: Implications for Sulfate Production in the Marine Atmosphere, Environ Sci Technol, 57, 6609–6615, https://doi.org/10.1021/acs.est.3c00212, 2023.

Zhou, R., Liu, J., Zhou, C., and Zhang, X.: Phototransformation of Lignin-related Compounds in Chromophoric Dissolved Organic Matter Solutions, Water Res, 245, https://doi.org/10.1016/j.watres.2023.120586, 2023.